LATTICE FIELD THEORY STUDIES OF MAGNETIC CATALYSIS IN GRAPHENE

by

Christopher R. Winterowd

A dissertation submitted to the faculty of
The University of Utah
in partial fulfillment of the requirements for the degree of

Doctor of Philosophy

in

Physics

Department of Physics and Astronomy

The University of Utah

August 2016

The University of Utah Graduate School

STATEMENT OF DISSERTATION APPROVAL

The dissertation of **Christopher R. Winterowd**

has been approved by the following supervisory committee members:

Carleton DeTar	, Chair	**05/31/16** Date Approved
Stephane Louis LeBohec	, Member	**06/13/16** Date Approved
Eugene Mishchenko	, Member	**06/13/16** Date Approved
Pearl Elizabeth Sandick	, Member	**06/14/16** Date Approved
Aaron L. Fogelson	, Member	**06/14/16** Date Approved

and by **Carleton DeTar** , Chair/Dean of

the Department of **Physics and Astronomy**

and by David B. Kieda, Dean of The Graduate School.

ABSTRACT

Consisting of a single two-dimensional layer of Carbon atoms arranged in a hexagonal lattice, graphene represents one of the most exciting recent developments in condensed matter physics. With novel electronic and mechancial properties, graphene not only has great potential with respect to technological applications, but also displays phenomena that typically appear in relativistic quantum field theory. The low-energy electronic excitations of graphene consist of two identical species of massless Dirac particles. Due to the small Fermi velocity, these particles are strongly coupled through the Coulomb interaction. Although various perturbative approaches have succeeded in elucidating many of the electronic properties of graphene, one would still like a nonperturbative study to address various questions. In particular, the spontaneous breaking of chiral symmetry in the presence of an external magnetic field, commonly known as magnetic catalysis, is one of these questions. Early studies of this phenomenon in model relativistic field theories have posited the mechanism to be universal. More recently, this mechanism of spontaneous symmetry breaking has been studied in low-dimensional condensed matter systems. Due to the strongly-coupled nature of the low-energy effective field theory of graphene, nonperturbative methods of lattice gauge theory can be used which are well suited to studying chiral symmetry breaking. Most notably used to study the theory of the strong interactions, quantum chromodynamics, these methods have proven successful in elucidating nonperturbative phenomena in cases where perturbative methods fail. In this thesis, using these methods, evidence in favor of magnetic catalysis in the graphene effective field theory will be presented.

CONTENTS

CHAPTERS

LIST OF FIGURES

LIST OF TABLES

ACKNOWLEDGMENTS

This thesis, and the work contained within it, would not be possible without the contributions, assistance, and support of numerous people. I am deeply indebted to my parents for their love and unconditional support throughout my life. I am also grateful to my advisor, Carleton DeTar, with whom I have worked and from whom I have learned throughout my seven years at the University of Utah. I owe a huge debt of gratitude to all of my physics professors, beginning from my undergradudate studies, until the present. They are the ones who I aspire to be like in my scientific life. Finally, I would like to thank my collaborator and friend Savvas Zafeiropoulos who has been a constant source of inspiration and motivation.

CHAPTER 1

INTRODUCTION TO GRAPHENE

We briefly review the discovery and history of graphene. We then set about to describe its unique electronic properties via the tight-binding description. From there, one is able to gain information regarding graphene's band structure. The appearance of the so-called "Dirac points", which are responsible for many of the novel electronic features of graphene, is discussed. The low-energy excitations due to these special points is the basis for our field theory description and nonperturbative study of the metal-insulator phase transition in graphene.

1.1 History and Discovery

Graphene is a remarkable material with an even more remarkable history. Consisting of a plane of Carbon atoms arranged in a hexagonal lattice, graphene is an allotrope of other more familiar, everyday Carbon structures such as diamond and graphite. Even though graphene is currently the subject of intense study and has spawned a rapidly increasing literature, studies of graphene's band structure date back to 1946 [2], when graphene was classified as a semimetal due to the touching of the conductance and valence bands at certain points in the Brillouin zone. Although not yet realized experimentally, this served as a starting point for the study of the band structure of graphite which followed in the works of McClure [3], and Slonczewski and Weiss [4]. Decades later, Novoselov and collaborators were able to experimentally isolate graphene, exploiting an optical effect it produced when placed on a SiO_2 substrate [5]. For their discovery, Novoselov and Geim were awarded the 2010 Nobel Prize in Physics. Since its discovery in 2004, graphene and its subfields have grown tremendously.

1.2 Electronic Properties of Graphene

1.2.1 Tight-Binding Description of Graphene

Graphene is a hexagonal lattice with Carbon atoms living at the vertices. The hexagonal lattice is not a Bravais lattice in that not every Carbon atom can be reached by a linear combination of primitive lattice vectors. Thus, one can think of graphene as a triangular lattice with a basis of two atoms, each belonging to its separate sublattice (sublattices A and B). The primitive lattice vectors are as follows:

$$\vec{a}_1 = \frac{a}{2}(3, \sqrt{3}), \quad \vec{a}_2 = \frac{a}{2}(3, -\sqrt{3}). \tag{1.1}$$

where the interatomic distance $a \approx 1.42$ Å. One can construct the reciprocal lattice vectors from the condition $\vec{a}_i \cdot \vec{b}_j = 2\pi\delta_{i,j}$ [6], thus obtaining

$$\vec{b}_1 = \frac{2\pi}{3a}(1, \sqrt{3}), \quad \vec{b}_2 = \frac{2\pi}{3a}(1, -\sqrt{3}). \tag{1.2}$$

The three nearest-neighbor vectors are given by

$$\vec{\delta}_1 = \frac{a}{2}(1, \sqrt{3}), \quad \vec{\delta}_2 = \frac{a}{2}(1, -\sqrt{3}), \quad \vec{\delta}_3 = a(-1, 0). \tag{1.3}$$

The nearest neighbors of a given site on a given sublattice belong to the opposite sublattice. There are six next-to-nearest neighbors, $\vec{\delta}'_i$, whose vectors are given by appropriate combinations of the primitive lattice vectors ($\pm\vec{a}_1$, $\pm\vec{a}_2$, $\pm(\vec{a}_1 - \vec{a}_2)$) and connect sites belonging to the same sublattice. In Fig. 1.1, the graphene lattice as well its reciprocal lattice are depicted.

One can construct a tight-binding description of electrons hopping between nearest and next-to-nearest neighbors. The Hamiltonian of this model is given by

$$\begin{aligned} \mathcal{H} = & - t \sum_{\langle i,j \rangle, \sigma} \left(a^{\dagger}_{i,\sigma} b_{j,\sigma} + \text{c.c.} \right) \\ & - t' \sum_{\langle\langle i,j \rangle\rangle, \sigma} \left(a^{\dagger}_{i,\sigma} a_{j,\sigma} + b^{\dagger}_{i,\sigma} b_{j,\sigma} + \text{c.c.} \right), \end{aligned} \tag{1.4}$$

where the electron creation (annihilation) operator on sublattice A is given by $a^{\dagger}_{i,\sigma}$ ($a_{i,\sigma}$) with i labeling the site, $\sigma =\uparrow, \downarrow$ label the spin, $t(\approx 2.8\text{eV})$ is the nearest-neighbor hopping parameter, and t' is the next-to-nearest neighbor hopping parameter. One then obtains the band structure by diagonalizing (1.4) in momentum space. First the spatial sums are recast

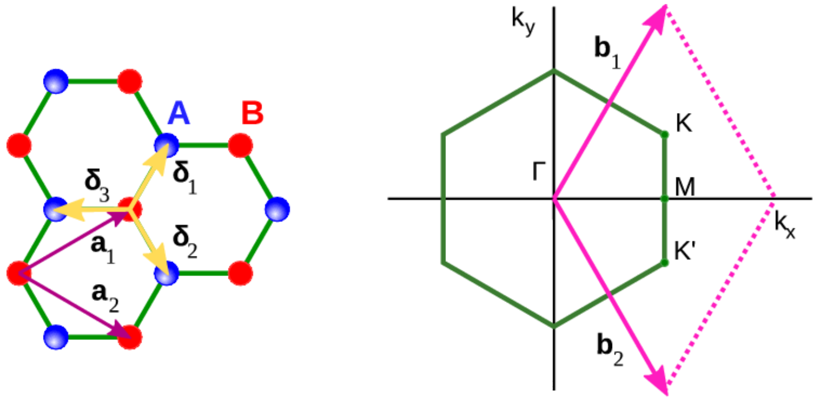

Figure 1.1. (left) The hexagonal lattice of graphene is illustrated along with the nearest-neighbor vectors, $\vec{\delta}_i, i = 1, 2, 3$, and the primitive lattice vectors, $\vec{a}_1, \vec{a}_2$. (right) The first Brillouin zone is depicted along with the reciprocal lattice vectors $\vec{b}_1, \vec{b}_2$. Courtesy of http://oer.physics.manchester.ac.uk/AQM2/Notes

into a sum over sites of a given sublattice and a sum over nearest or next to nearest-neighbors i.e., for the nearest-neighbor term one has

$$\sum_{\langle i,j\rangle,\sigma}\left(a^{\dagger}_{i,\sigma}b_{j,\sigma}+\text{c.c.}\right)=\sum_{\vec{x},\sigma}\sum_{\vec{\delta}_i}\left(a^{\dagger}_{\vec{x},\sigma}b_{\vec{x}+\vec{\delta}_i,\sigma}+\text{c.c.}\right) \tag{1.5}$$

One now goes to momentum space by using the Fourier representation of the creation and annihilation operators

$$\begin{aligned} a_{\vec{x},\sigma} &= \frac{1}{\sqrt{N}}\sum_{\vec{k}} e^{i\vec{k}\cdot\vec{x}}a_{\vec{k},\sigma} \\ a^{\dagger}_{\vec{x},\sigma} &= \frac{1}{\sqrt{N}}\sum_{\vec{k}} e^{-i\vec{k}\cdot\vec{x}}a^{\dagger}_{\vec{k},\sigma}. \end{aligned} \tag{1.6}$$

This allows one to rewrite the Hamiltonian as

$$\begin{aligned} \mathcal{H} = &- t\sum_{\vec{x},\sigma}\sum_{\vec{\delta}_i}\frac{1}{N}\sum_{\vec{k},\vec{k}'}\left(a^{\dagger}_{\vec{k},\sigma}b_{\vec{k}',\sigma}e^{i\vec{k}'\cdot\vec{\delta}_i}+\text{c.c.}\right)e^{i(\vec{k}'-\vec{k})\cdot\vec{x}} \\ &- t'\sum_{\vec{x},\sigma}\sum_{\vec{\delta}'_i}\frac{1}{N}\sum_{\vec{k},\vec{k}'}\left((a^{\dagger}_{\vec{k},\sigma}a_{\vec{k}',\sigma}+b^{\dagger}_{\vec{k},\sigma}b_{\vec{k}',\sigma})(e^{i\vec{k}'\cdot\vec{\delta}'_i}+e^{-i\vec{k}'\cdot\vec{\delta}'_i})\right)e^{i(\vec{k}'-\vec{k})\cdot\vec{x}} \\ = &- \sum_{\vec{k},\sigma}\left(\gamma(\vec{k})a^{\dagger}_{\vec{k},\sigma}b_{\vec{k},\sigma}+\text{c.c.}\right)-\sum_{\vec{k},\sigma}\beta(\vec{k})\left(a^{\dagger}_{\vec{k},\sigma}a_{\vec{k},\sigma}+b^{\dagger}_{\vec{k},\sigma}b_{\vec{k},\sigma}\right) \end{aligned} \tag{1.7}$$

where in the second line, the identity $\frac{1}{N}\sum_{\vec{x}} e^{i\vec{x}\cdot(\vec{k}-\vec{k}')} = \delta_{\vec{k},\vec{k}'}$ was used and the the following quantities have been introduced

$$\gamma(\vec{k}) \equiv t\sum_{\vec{\delta}_i} e^{i\vec{k}\cdot\vec{\delta}_i}, \quad \beta(\vec{k}) \equiv t'\sum_{\vec{\delta}'} 2\cos(\vec{k}\cdot\vec{\delta}'_i). \tag{1.8}$$

One can now diagonalize the Hamiltonian (1.7) most easily by introducing the following matrix form, which will be useful later on

$$\begin{aligned} \mathcal{H} &= \sum_{\vec{k},\sigma} \left(\begin{array}{cc} a^\dagger_{\vec{k},\sigma}, & b^\dagger_{\vec{k},\sigma} \end{array} \right) \mathcal{H}(\vec{k}) \left(\begin{array}{c} a_{\vec{k},\sigma} \\ b_{\vec{k},\sigma} \end{array} \right) && (1.9) \\ \mathcal{H}(\vec{k}) &= \left(\begin{array}{cc} -\beta(\vec{k}) & -\gamma(\vec{k}) \\ -\gamma^*(\vec{k}) & -\beta(\vec{k}) \end{array} \right) && (1.10) \end{aligned}$$

From the above expression, one can compute the band energies which are determined by

$$\det \Big(\mathcal{H}(\vec{k}) - E(\vec{k})\mathbf{1} \Big) = 0 \tag{1.11}$$

$$E_{\pm}(\vec{k}) = \pm|\gamma(\vec{k})| - \beta(\vec{k}) \tag{1.12}$$

For what follows, the next-to-nearest neighbor hopping will be neglected and thus one sets $\beta(\vec{k}) = 0$ in (1.12), yielding $E_{\pm}(\vec{k}) = \pm|\gamma(\vec{k})|$. The band structure is illustrated in Fig. 1.2. The "+" corresponds to the conduction band whereas the "−" corresponds to the valence band. In neutral graphene, the valence band is filled while the conduction band is empty.

The conductance and valence bands touch at two (unique) points in the Brillouin zone, which we label K and K'. These points are given by

$$\vec{K} = \left(\frac{2\pi}{3a}, \frac{2\pi}{3\sqrt{3}a} \right), \qquad \vec{K}' = \left(\frac{2\pi}{3a}, -\frac{2\pi}{3\sqrt{3}a} \right). \tag{1.13}$$

One can indeed explicitly verify that the bands touch by noting that

$$\gamma(\vec{k} = \vec{K}) = \gamma(\vec{k} = \vec{K}') = 0. \tag{1.14}$$

These points are referred to as Dirac points as the excitations close to them are described by Dirac fermions. This can be seen in Fig. 1.3, where the Dirac cone is depicted. One can see this by considering the conductance band at $\vec{k} = \vec{K} + \vec{q}$

$$\begin{aligned} E(\vec{k}) &= t\sqrt{3 + 4\cos(\sqrt{3}/2k_y a)\cos(3/2k_x a) + 2\cos(\sqrt{3}k_y a)} \\ E(\vec{K} + \vec{q}) &= E(\vec{K}) + \vec{q} \cdot \frac{\partial E}{\partial \vec{k}}|_{\vec{k}=\vec{K}} + O(q^2) \\ \epsilon(\vec{q}) &= v_F|\vec{q}| + O((q/K)^2) && (1.15) \end{aligned}$$

where $E(\vec{K}) = E(\vec{K}') = 0$, and the Fermi velocity $v_F = 3ta/2 \approx c/300$ has been introduced. From this, one can see that although these low-energy excitations have a relativistic dispersion, one does not have Lorentz symmetry due to the small Fermi velocity. The dispersion of these excitations differ from most metals where the conductance band has curvature and the excitations have a quadratic dispersion $\epsilon(\vec{q}) = q^2/2m^*$, where m^* is the effective mass

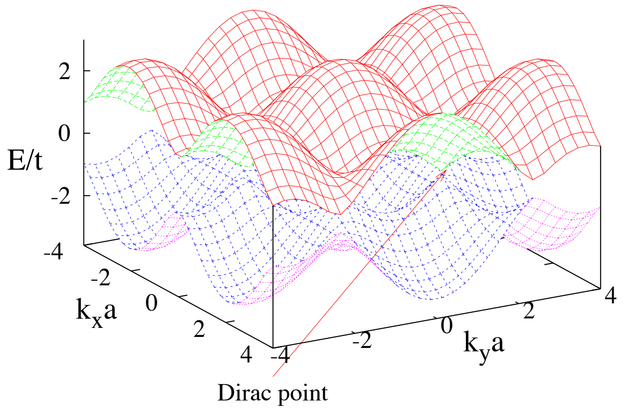

Figure 1.2. The band structure of graphene. One can see the points where the two bands touch, known as Dirac points.

of the quasiparticle. Furthermore, in the case of the low-energy excitations of graphene, the Fermi velocity is constant whereas, in the quadratic case, it is momentum dependent i.e., $v = \partial\epsilon(\vec{q})/\partial q = q/m^*$.

Other variations of graphene are interesting, both theoretically and experimentally, in their own right. The simplest variation of single-layer graphene is bilayer graphene and can be also understood within a tight-binding description [7]. The configuration of the two layers in bilayer graphene is such that the A sublattices are stacked on top of each other (known as AB or Bernal stacking). Considering only nearest-neighbor in-plane hopping as well as hopping between the A sublattices of the two layers, one finds four bands, two of which touch at the Dirac points $\vec{K}$ and $\vec{K}'$ and have parabolic dispersion. By applying a voltage perpendicular to the graphene layers one can open and control a gap between these two bands.

Doped single-layer graphene, trilayer, as well as graphite constitute other related subfields. Despite being very active and containing many interesting avenues of research, this thesis will not discuss them.

1.2.2 Dirac Fermions

In the previous subsection, the form of the tight-binding Hamiltonian in the limit of only nearest-neighbor hopping was discussed and from that the band structure was derived. At

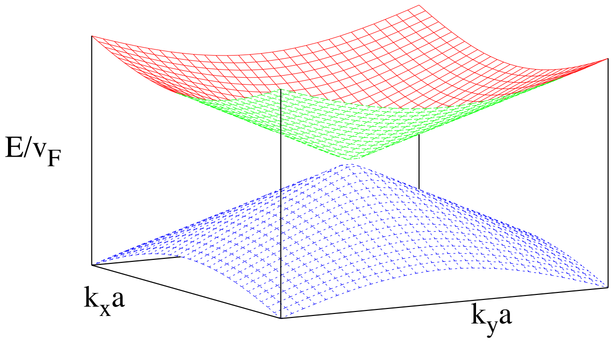

Figure 1.3. Close up of the Dirac cone, where the dispersion of the quasiparticles is given by $E(\vec{k}) = v_F|\vec{k}|$.

the Dirac points, one has massless particles with linear dispersion. One would like to take this a step further and make fully clear the connection between the low-energy excitations and the Dirac equation. To do this, one writes the Hamiltonian of the low-energy excitations as the sum of two terms, one coming from K and one coming from K'. After a unitary rotation of basis which removes a phase, one obtains

$$\begin{aligned}
\mathcal{H} &\approx \mathcal{H}_K + \mathcal{H}_{K'} \\
&= \Psi^\dagger_{K,\sigma} \begin{pmatrix} 0 & (q_x + iq_y) \\ (q_x - iq_y) & 0 \end{pmatrix} \Psi_{K,\sigma} + \Psi^\dagger_{K',\sigma} \begin{pmatrix} 0 & (q_x - iq_y) \\ (q_x + iq_y) & 0 \end{pmatrix} \Psi_{K',\sigma} \\
&= \Psi^\dagger_{K,\sigma} \vec{\sigma} \cdot \vec{q} \Psi_{K,\sigma} + \Psi^\dagger_{K',\sigma} \vec{\sigma}^* \cdot \vec{q} \Psi_{K',\sigma} \qquad (1.16)
\end{aligned}$$

where the spinors $\Psi_{K^{(\prime)},\sigma} = \begin{pmatrix} \psi_{K^{(\prime)},a,\sigma} \\ \psi_{K^{(\prime)},b,\sigma} \end{pmatrix}$ have been introduced. Rearranging the basis, one is able to write the Hamiltonian in the following compact form by introducing a tensor product of sublattice, valley, and spin space,

$$\mathcal{H}(\vec{q}) = v_F \sigma \cdot \vec{q} \otimes \mathbf{1} \otimes \mathbf{1}. \qquad (1.17)$$

Thinking ahead to our staggered lattice fermion formulation of the theory which will be analyzed in a chapter to come, one can think of the four-dimensional space of the sublattice tensored with the valley degrees of freedom as comprising the normal Dirac spinor degrees of freedom while the two-dimensional space of the electron's spin comprises a flavor (referred to as “taste” in the language of staggered fermions) degree of freedom. The two-component eigenfunctions of $\mathcal{H}_K(\vec{q})$, with energies given by $E = \pm v_F q$, can be written

$$\Psi_{K,(\pm)} = \frac{1}{\sqrt{2}} \begin{pmatrix} e^{-i\phi_q/2} \\ \pm e^{i\phi_q/2} \end{pmatrix} \tag{1.18}$$

where $\phi_q = \tan^{-1}(q_y/q_x)$. An analogous expression can be constructed for the eigenstates for valley K'. Just as one would expect for massless, Dirac fermions in relativistic quantum field theory [8], these states are chiral. We can verify this by noting the following

$$\frac{\vec{\sigma} \cdot \vec{q}}{q} \Psi_{K,(\pm)} = \pm \Psi_{K,(\pm)} \tag{1.19}$$

In this case, chirality pertains to the sublattice degree of freedom, which is sometimes referred to as pseudospin.

The formation of a gap at the Dirac points would require an additional term in the Hamiltonian. One can show that a mass term is forbidden as a consequence of symmetry considerations [9]. The effect of time-reversal on the system exchanges Dirac points (can take $\vec{K}' = -\vec{K}$) but does not affect the sublattice degrees of freedom

$$T \mathcal{H}_K T^{-1} = \mathcal{H}^*_{K'} \tag{1.20}$$

The effect of spatial inversion exchanges both sublattice degrees of freedom as well as Dirac points

$$I \mathcal{H}_K I^{-1} = \sigma_x \mathcal{H}_{K'} \sigma_x \tag{1.21}$$

Invariance under the combined action of time-reversal and spatial inversion imposes the following condition on the valley Hamiltonians

$$\mathcal{H}_K = \sigma_x \mathcal{H}^*_K \sigma_x \tag{1.22}$$

If one writes down the most general 2 × 2 Hamiltonian as

$$\mathcal{H}(\mathbf{k}) = \vec{h}(\mathbf{k}) \cdot \vec{\sigma}, \tag{1.23}$$

where $\vec{h}(\mathbf{k}) \equiv (h_x, h_y, h_z)$, inversion symmetry requires $h_z(-\mathbf{k}) = -h_z(\mathbf{k})$ while time-reversal symmetry requires $h_z(-\mathbf{k}) = h_z(\mathbf{k})$. Thus, if both symmetries are present, one is forced to require $h_z(\mathbf{k}) = 0$. A gap can form at the Dirac points if one of these symmetries is violated. Inversion symmetry is violated if the two sublattices become inequivalent to each other. In the low-energy theory this is represented by adding a Dirac mass term to (1.17) of the form

$$m\,(\sigma_z \otimes \mathbf{1} \otimes \mathbf{1})\,, \tag{1.24}$$

where the unit matrices are in the valley and spin spaces. One can show that a gap of $2m$ forms at each of the Dirac points. This is the usual mass term that appears in relativistic field theory. If time-reversal symmetry is broken but spatial inversion is not, one can introduce a mass term which is positive at one Dirac point and negative at the other, $m(K) = -m(K') = -m(-K)$. In the low-energy theory, this is represented by adding a mass term of the form [10]

$$m\,(\sigma_z \otimes \sigma_z \otimes \mathbf{1})\,. \tag{1.25}$$

Both types of masses will be studied in this thesis.

The Hamiltonian in (1.17) also has the following symmetries associated with it

$$\begin{aligned} \sigma_3 \mathcal{H}_{K,K'}(\vec{k})\sigma_3 &= -\mathcal{H}_{K,K'}(\vec{k}), & (1.26)\\ \sigma_2 \mathcal{H}^*_{K,K'}(\vec{k})\sigma_2 &= -\mathcal{H}_{K,K'}(\vec{k}). & (1.27) \end{aligned}$$

The implications of these relations is that given an eigenstate of the Hamiltonian ψ, with energy E, there exist states $\sigma_3\psi$ and $\sigma_2\psi^*$ which have energy $-E$. This follows from (1.26) and (1.27), respectively. When a mass term of the form (1.24) or (1.25) is introduced, (1.26) is no longer satisfied but the spectrum is still symmetric about $E = 0$ due to (1.27). This symmetry is known as particle-hole symmetry. In the low-energy effective field theory for graphene, which will be used in this thesis, this symmetry relates particles and antiparticles.

In the coming chapters it will be convenient to bundle the Bloch components for a given spin projection into a four-dimensional Dirac spinor

$$\psi_\sigma^\top = (\psi_{KA\sigma}, \psi_{KB\sigma}, \psi_{K'B\sigma}, \psi_{K'A\sigma})\,, \tag{1.28}$$

where K, K' refer to the Dirac points, σ refers to the electron's spin projection, and A, B refer to the sublattice. In this basis, it is also convenient to describe the effect of the discrete symmetries. Ignoring spin, the action of time-reversal in the basis four-dimensional sublattice-valley subpsace is as follows

$$\begin{aligned} \begin{pmatrix} \psi_{A\sigma}(\vec{K}+\vec{p}) \\ \psi_{B\sigma}(\vec{K}+\vec{p}) \\ \psi_{B\sigma}(\vec{K'}+\vec{p}) \\ \psi_{A\sigma}(\vec{K'}+\vec{p}) \end{pmatrix} &\rightarrow \begin{pmatrix} \psi_{A\sigma}(\vec{K'}-\vec{p}) \\ \psi_{B\sigma}(\vec{K'}-\vec{p}) \\ \psi_{B\sigma}(\vec{K}-\vec{p}) \\ \psi_{A\sigma}(\vec{K}-\vec{p}) \end{pmatrix} & (1.29)\\ &= T\psi_\sigma(-\vec{p}), & (1.30) \end{aligned}$$

where $\psi_{K^{(\prime)},A/B,\sigma}(\vec{p}) \equiv \psi_{A/B,\sigma}(\vec{K}^{(\prime)} + \vec{p})$, and the spinor has been written in momentum space. One sees that the transformation interchanges Dirac points but leaves the sublattice degree of freedom intact. Time-reversal acts on the spin projection in the following way

$$\begin{aligned} \begin{pmatrix} \psi_{K,A/B,\uparrow} \\ \psi_{K,A/B,\downarrow} \end{pmatrix} &\rightarrow \begin{pmatrix} \psi_{K,A/B,\downarrow} \\ -\psi_{K,A/B,\uparrow} \end{pmatrix}, \qquad (1.31) \\ &= i\sigma_2 \begin{pmatrix} \psi_{K,A/B,\uparrow} \\ \psi_{K,A/B,\downarrow} \end{pmatrix}. \qquad (1.32) \end{aligned}$$

Combining the action of time-reversal on both the four-dimensional sublattice-valley space and on the two-dimensional spin space one obtains the following result in momentum space

$$\psi(\vec{p}) \rightarrow (T \otimes i\sigma_2)\, \psi(-\vec{p}). \qquad (1.33)$$

For the coordinate space spinor, time-reversal takes the following form

$$\psi(\vec{x}, t) \rightarrow (T \otimes i\sigma_2)\, \psi(\vec{x}, -t). \qquad (1.34)$$

One can then show that the Hamiltonian in this basis is left invariant by the following transformations [11]

$$\begin{aligned} \psi(\vec{x}, t) &\rightarrow (T \otimes i\sigma_2)\, \psi(\vec{x}, -t), \qquad (1.35) \\ \bar{\psi}(\vec{x}, t) &\rightarrow -\bar{\psi}(\vec{x}, -t)\, (T \otimes i\sigma_2)\,, \qquad (1.36) \\ A_0(\vec{x}, t) &\rightarrow -A_0(\vec{x}, -t). \qquad (1.37) \end{aligned}$$

Spatial inversion acts on the four-dimensional spinor as follows

$$\begin{aligned} \begin{pmatrix} \psi_{A\sigma}(\vec{K} + \vec{p}) \\ \psi_{B\sigma}(\vec{K} + \vec{p}) \\ \psi_{B\sigma}(\vec{K}' + \vec{p}) \\ \psi_{A\sigma}(\vec{K}' + \vec{p}) \end{pmatrix} &\rightarrow \begin{pmatrix} \psi_{B\sigma}(\vec{K}' - \vec{p}) \\ \psi_{A\sigma}(\vec{K}' - \vec{p}) \\ \psi_{A\sigma}(\vec{K} - \vec{p}) \\ \psi_{B\sigma}(\vec{K} - \vec{p}) \end{pmatrix} \qquad (1.38) \\ &= P\psi_\sigma(-\vec{p}), \qquad (1.39) \end{aligned}$$

where the transformation was written in momentum space. A similar transformation exists in coordinate space

$$\psi(\vec{r}, t) \rightarrow P\psi(-\vec{r}, t). \qquad (1.40)$$

One sees that the transformation interchanges Dirac points as well as sublattices. Unlike time-reversal, inversion does not act on the spin degree of freedom.

CHAPTER 2

EFFECTIVE FIELD THEORY DESCRIPTION OF GRAPHENE

In this chapter the philosophy of effective field theory (EFT) in modern physics, particularly in the context of condensed matter physics and graphene, is discussed. By considering the low-energy excitations of graphene, one constructs a continuum gauge theory which describes Coulomb interaction of Dirac fermions in $(2+1)$ dimensions where the temporal component of the gauge field, A_0, lives in $(3+1)$ dimensions. From an appropriate rescaling of the continuum theory, one finds that the effective coupling between the fermions, $\alpha_g \equiv e^2/(\epsilon v_F 4\pi) > 1$, where ϵ is the dielectric constant of the substrate. Thus, the strongly coupled nature of the theory disfavors a perturbative analysis of the theory. Being a gauge theory, the EFT can be studied using methods from lattice quantum chromodynamics (LQCD), which are well suited to tackling nonperturbative questions.

2.1 Motivation and Uses of Effective Field Theory in Physics

The idea of an effective field theory that describes particular regimes of physics has been a very useful approach that has been applied succesfully in high-energy as well as condensed matter physics. Starting from an underlying, more fundamental theory, one can often construct a simpler theory which aims at describing physical degrees of freedom appropriate at a certain length or energy scale. One of the most famous examples of an effective field theory in twentieth-century physics is the Fermi theory of the weak interactions [12]. The electroweak theory of Weinberg, Glashow, and Salam presumably describes physics up to the unification scale, yet at low enough energies ($\sim$ 10 MeV) the Fermi theory accurately describes nuclear beta decay. This is primarily due to the fact that the mass of the charged electroweak boson, $W^{\pm}$, which defines the scale of the electroweak theory, $m_{W^{\pm}} \approx 80$GeV, is much larger than the energy at which the decay occurs. Thus, one has a separation of scales in which some degrees of freedom in the underlying theory do not appear in the effective theory (the electroweak gauge bosons). Another application of EFTs in high-energy physics appears in the low-energy dynamics of the theory of the strong interactions, quantum chromodynamics (QCD). The low-energy regime is dominated by pions, kaons, and the eta for number of quark flavors $N_f = 3$. One can write down a theory based on the symmetries of the underlying theory and the phenomenon of chiral symmetry breaking, which tells us that the pions are Goldstone bosons [13, 14].

In condensed matter physics, one typically starts from a many-body Hamiltonian describing the electrons and their interactions. In certain instances, once the relevant physics of the particular system has been identified, one can often write down a simpler theory which describes these pertinent degrees of freedom and inherits their symmetries. One famous example of this is the Bardeen-Cooper-Schrieffer (BCS) theory of superconductivity [15]. In metals, phonons can mediate an attractive interaction between certain electrons, leading to the formation of Cooper pairs which bring about the transition to the superconducting state. In the effective theory, this is taken into account by introducing an attractive point-like interaction between electrons. In graphene, one can look at regions close to the Dirac points where the dispersion of excitations is relativistic. Counting the fermionic degrees of freedom correctly, one effectively is left with a theory of two identical flavors of massless Dirac fermions that can interact electromagnetically. Naturally, one then introduces a gauge field which mediates this interaction, leaving a variant of $(2 + 1)$-dimensional quantum electrodynamics (QED). In the following sections, we realize this program and write down the continuum EFT that we will later study on the lattice.

EFTs are not typically renormalizable in the sense of QED. One can think of the EFT as an expansion in a momentum or energy, characterizing a typical process which it describes. At each order in this expansion, one needs to introduce new parameters to keep the theory finite. Although in the early days of quantum field theory this approach faced resistance, with the advent of the renormalization group (RG) [16] a new undestanding of this type of theory and what it meant gave new life to the technique of EFT. Namely, one could think of the EFT as a low-energy theory obtained by taking the more fundamental theory valid at higher energies, and “integrating out” the high modes. What one is left with is a simpler theory where the physics at the scale of the cutoff would be encoded in the parameters introduced in the effective Lagrangian.

2.2 Continuum EFT for Graphene

In this section, the continuum action for the fermionic degrees of freedom is introduced, followed by the continuum action for the gauge field in the Coulomb approximation. This is the form that will later be discretized upon moving to the cubic lattice.

2.2.1 Fermionic Sector

From the discussion in the previous chapter, it is evident that the low-energy excitations consist of two species of massless four-component Dirac fermions (2 valley × 2 sublattice × 2 spin). One can immediately writef down the continuum Euclidean action describing the fermions

$$S_F \;=\; \int dt d^2x \sum_{a=1,2}\left(\bar{\psi}_a\gamma_0\partial_0\psi_a + v_F\sum_{i=1,2}\bar{\psi}_a\gamma_i\partial_i\psi_a + m\bar{\psi}_a\psi_a\right) \tag{2.1}$$

where the index i runs over $1,2$, characterizing the spatial directions in the plane and the Dirac matrices $\gamma_\mu, \mu = 0,1,2$, satisfying the Clifford algebra $\{\gamma_\mu,\gamma_\nu\} = 2\delta_{\mu\nu}$ have been introduced. In (2.1), the four-component Dirac spinors are organized as in (1.28). The mass term, $m\bar{\psi}\psi$, has also been introduced in anticipation of our lattice formulation. As will be seen later, this will act as an infrared regulator necessary to perform Monte Carlo simulations of the theory.

The spinor representation of the Lorentz group, and thus the gamma matrices which the generators are constructed from, is of dimension $2^{[d/2]}$ [17]. One notes that in this theory four-component spinors have been introduced instead of the assumed two-component spinors. In doing so one constructs a reducible representation composed of the two inequivalent, irreducible representations of the Clifford algebra in odd Euclidean dimensions. One thus can write

$$\gamma_\mu = \begin{pmatrix} \sigma_\mu & 0 \\ 0 & -\sigma_\mu \end{pmatrix}, \quad \mu = 0,1,2 \tag{2.2}$$

where σ_μ refers to the Pauli matrices ($\sigma_0 \equiv \sigma_3$), which form an irreducible representation of the Clifford algebra. The other irreducible representation can be taken as $-\sigma_\mu$ as implied by the form in (2.2). In (3+1)-dimensions, one could identify a similarity transformation S, $S^\dagger\gamma_\mu^{(1)}S = \gamma_\mu^{(2)}$, given by the familiar $S = \gamma_5 = \gamma_5^\dagger$ where $\{\gamma_\mu,\gamma_5\} = 0$. By the very definition of this matrix, $\gamma_5 \equiv \mathcal{C}\prod_{i=1}^{d}\gamma_i$, with $\mathcal{C}$ a phase factor, one can verify that in odd Euclidean dimensions $\gamma_5 \propto \mathbf{1}$ [18]. This issue is intimately related to chirality in odd-dimensional relativistic quantum field theory. One can also define an additional set of matrices which generate symmetry transformations in the graphene EFT

$$\tilde{\gamma}_4 = \begin{pmatrix} 0 & \mathbf{1} \\ \mathbf{1} & 0 \end{pmatrix}, \quad \tilde{\gamma}_5 = \begin{pmatrix} 0 & \mathbf{1} \\ -\mathbf{1} & 0 \end{pmatrix} \tag{2.3}$$

$$\tilde{\gamma}_{4,5} \equiv -\tilde{\gamma}_4\tilde{\gamma}_5 = \begin{pmatrix} \mathbf{1} & 0 \\ 0 & -\mathbf{1} \end{pmatrix} \tag{2.4}$$

The continuum fermionic action listed in (2.1) has a $U(4)$ flavor symmetry which can be seen by using the four-dimensional gamma matrices defined in (2.3) and (2.4) to construct the $4^2 = 16$ generators of the group

$$\mathbf{1} \otimes \mathbf{1}, \quad \mathbf{1} \otimes \sigma_\mu, \quad \tilde{\gamma}_{4,5} \otimes \mathbf{1}, \quad \tilde{\gamma}_{4,5} \otimes \sigma_\mu \tag{2.5}$$

$$\tilde{\gamma}_4 \otimes \mathbf{1}, \quad \tilde{\gamma}_4 \otimes \sigma_\mu, \quad i\tilde{\gamma}_5 \otimes \mathbf{1}, \quad i\tilde{\gamma}_5 \otimes \sigma_\mu, \tag{2.6}$$

where the four-dimensional sublattice $\otimes$ valley subspace has been tensored with the two-dimensional spin subspace. The mass term of the form

$$\mathcal{L}_m = m \sum_{a=1,2} \bar{\psi}_a \psi_a, \tag{2.7}$$

breaks the $U(4)$ symmetry down to a $U(2) \otimes U(2)$ symmetry whose generators are given by (2.5). Similarily, a formation of a nonzero value for the chiral condensate, $\langle \bar{\psi}_a \psi_a \rangle$, would signal spontaneous symmetry breaking, $U(4) \to U(2) \otimes U(2)$, which would imply the appearance of $16 - 2(2^2) = 8$ Goldstone bosons which would parametrize the coset.

2.2.2 Gauge Sector

The Dirac-like quasiparticles of graphene are electrically charged and thus interact electromagnetically. In the framework of our EFT, this would necessitate the introduction of a $U(1)$ gauge field, A_μ. The gauge field presumably would live in $(3+1)$ dimensions (the graphene sheet is embedded in our normal $(3+1)$-dimensional world) and would have an action resembling that of electrodynamics

$$S_G = \frac{\epsilon}{4} \int d^3x dt \; (F_{\mu\nu})^2, \tag{2.8}$$

where one has introducted the $U(1)$ field-strength tensor $F_{\mu\nu} \equiv \partial_\mu A_\nu - \partial_\nu A_\mu$, $\mu, \nu = 0, 1, 2, 3, 4$ and ϵ represents the dielectric constant of the material on which graphene is embedded.

Recalling the analysis from the previous chapter, one notices that the excitations near the Dirac point have a tiny Fermi velocity, $v_F/c \approx 1/300$. This suggests that a valid approximation would be to neglect magnetic fields ($F_{ij} = 0$) and to neglect electric fields created by magnetic induction ($\partial_0 A_i = 0$) [19]. Applying this to (2.8) results in

$$S_G = \frac{\epsilon}{2} \int d^3x dt \ (\partial_i A_0)^2. \tag{2.9}$$

One notices that the action in (2.9) is invariant under spatially uniform shifts of the gauge potential, i.e., $A_0 \to A_0 + \alpha(t)$, where $\alpha(t)$ is a function of time only. This fact is equivalent to the gauge invariance of the action. This also has consequences in the fermionic sector as one must introduce interactions with A_0. This is done in the usual way, $\partial_0 \to \partial_0 - ieA_0$, known as minimal coupling. This leads to an interaction term of the form

$$S_{int} = -ie \int dt d^2x \sum_{a=1,2} \bar{\psi}_a \gamma_0 A_0 \psi_a. \tag{2.10}$$

It was previously mentioned that the graphene EFT is strongly coupled. One can easily see this by defining the following rescalings [20]:

$$x_0 = v_F t, \quad A_0 = \frac{v_F}{e} A_0', \quad D_0 = \partial_0 - iA_0'. \tag{2.11}$$

Rewriting the action in terms of these quantities, one obtains

$$\begin{aligned} S = \int d^3x \sum_{a=1,2} \big(& \bar{\psi}_a \gamma_0 D_0 \psi_a + \sum_{i=1,2} \bar{\psi}_a \gamma_i \partial_i \psi_a \\ & + \frac{m}{v_F} \bar{\psi}_a \psi_a \big) + \frac{\epsilon v_F}{2e^2} \int d^4x \sum_{i=1}^{3} (\partial_i A_0')^2. \end{aligned} \tag{2.12}$$

From the form of the action in (2.12), one recognizes that the true fermion-fermion-photon coupling is $g^2 \equiv \frac{e^2}{v_F \epsilon} = \frac{c}{v_F} 4\pi\alpha$, where α is the fine structure constant of QED. This suggests that perturbation theory is most reliable when $\alpha_g \equiv \frac{g^2}{4\pi} = \alpha \frac{c}{v_F} \ll 1$, which for graphene does not hold true due to the small Fermi velocity of the Dirac quasiparticles. Although perturbation theory can be useful in certain instances, one might want to employ nonperturbative techniques. For this reason, lattice Monte Carlo simulations are important to gain insight into various aspects of graphene just as they have proved useful in studying the theory of the strong interactions, QCD. In particular, lattice methods will be used to study the formation of the chiral condensate, $\langle \bar{\psi}\psi \rangle \neq 0$, as well as a time-reversal odd condensate, $\langle \bar{\psi} \tilde{\gamma}_{4,5} \psi \rangle$, as a function of the inverse coupling $\beta \equiv \frac{1}{g^2}$ as well as a function of an external magnetic field perpendicular to the sheet of graphene.

CHAPTER 3

MAGNETIC CATALYSIS IN GRAPHENE

The phenomenon of magnetic catalysis, first proposed by Miransky and collaborators [21, 22, 23, 24], is a fascinating example of dynamical symmetry breaking. In $(2+1)$-dimensions, an external magnetic field can be shown to be a catalyst for this symmetry breaking that leads to dynamical mass generation for fermions even if they are weakly interacting. First shown in the context of the Nambu-Jona-Lasinio (NJL) model [25, 26], this phenomenon has been proposed for two-dimensional condensed matter systems as well, including graphene. Although various approaches such as the Schwinger-Dyson equations (SDE) have been employed to study and lend support to this phenomenon, it is also useful to apply LQCD methods in the context of the graphene EFT to further the understanding of this type of dynamical symmetry breaking in low-dimensional systems.

3.1 Dirac Fermions in a Magnetic Field

Before considering a full interacting theory such as the graphene EFT, one can start from a free Dirac theory in a constant external magnetic field. Already from here, one can begin to understand the mechanism for the catalysis which involves the dimensional reduction $D \to D-2$ [27].

The equation for a $(3+1)$-dimensional charged Dirac fermion in the presence of an external constant magnetic field is given by the following

$$(i\gamma^{\mu}\mathcal{D}_{\mu} - m)\psi = 0, \tag{3.1}$$

where $\mathcal{D}_{\mu} = \partial_{\mu} - ieA_{\mu}$. The gauge field A_{μ} describes the external magnetic field oriented in the z-direction and in Landau gauge it is given by

$$A_{\mu} = \delta_{\mu,2} B x_1, \quad \nabla \times \vec{A} = B\hat{z}. \tag{3.2}$$

The Dirac equation, $H_D\psi = E\psi$, in the presence of the vector potential in (3.2), can be written as two coupled equations

$$\begin{aligned}\vec{\sigma}\cdot(\vec{p}-e\vec{A})\chi &= (\epsilon-m)\,\phi, && (3.3)\\ \vec{\sigma}\cdot(\vec{p}-e\vec{A})\phi &= (\epsilon+m)\,\chi, && (3.4)\end{aligned}$$

where χ and ϕ are two-component spinors. Eliminating χ, one is able to obtain

$$\left(\vec{p}^2+e^2B^2x^2-eB\left(\sigma_z-2xp_y\right)\right)\phi=\left(\epsilon^2-m^2\right)\phi. \qquad (3.5)$$

Using the ansatz $\phi(x,y,z)=e^{i(p_yy+p_zz)}f(x)$ and defining the variable $\xi=\sqrt{eB}\,(x-p_y/eB)$, one can write an equation for $f(x)$ that resembles the quantum harmonic oscillator

$$\begin{aligned}\left(-\frac{d^2}{d\xi^2}+\xi^2\right)f &= (a+\mu)f, && (3.6)\\ a &\equiv \frac{E^2-m^2-p_z^2}{eB},\end{aligned}$$

where f is an eigenstate of σ_z, $\sigma_zf=\mu f$ with $\mu=\pm$. One then obtains

$$E_n(p_z)=\pm\sqrt{m^2+2|eB|n+p_z^2}, \qquad (3.7)$$

where n is a non-negative integer ($n=0,1,2,\dots$) labeling the Landau level [28]. One can relate this index to contributions from the orbital motion and the spin, $n\equiv k+s_z+\frac{1}{2}$, where $k=0,1,2,\dots$ is the orbital quantum number and $s_z=\pm\frac{1}{2}$ is the projection of the spin onto the direction of the external field.

There arise various distinctions between the lowest Landau level (LLL) ($n=0$) and all other Landau levels ($n>0$). The first distinction is that the LLL corresponds to the lowest orbital state $k=0$ with $s_z=-\frac{1}{2}$ only. This implies that the LLL is spin-polarized while all other levels can be degenerate in the two spin projections ($k,\ s_z=+\frac{1}{2}$ and $k+1,\ s_z=-\frac{1}{2}$). Another crucial distinction comes from the degeneracy of the LLL. For a fixed value of n and p_z, this degeneracy arises from the freedom to choose the center of the orbit in the x-direction which is given by p_y/eB. This leads to a degeneracy per area in the xy-plane which is given by $\frac{|eB|}{2\pi}$ for $n=0$ and $\frac{|eB|}{\pi}$ for $n>0$.

When one considers a Dirac mass, which is small with respect to the energy scale of the Landau levels, $m\ll\sqrt{|eB|}$, one can see that the low-energy dynamics are completely dominated by the LLL. In this limit, the excitations have energy given by $E_{n=0}(p_z)=\pm\sqrt{m^2+p_z^2}$. One immediately notices that this is the dispersion relation for $(1+1)$-dimensional Dirac particles. Thus by considering this limit, we have effectively seen a dimensional reduction, $D\to D-2$.

Having solved the problem in $(3+1)$-dimensions, it is straightforward to obtain the spectrum of Dirac fermions in a constant external magnetic field in $(2+1)$-dimensions.

Using the reducible representation of the Clifford algebra introduced in (2.2), one proceeds analogously to obtain the energies given by

$$E_n = \pm\sqrt{m^2 + 2|eB|n}. \tag{3.8}$$

This is the form in (3.7), having set $p_z = 0$. Similar arguments made in the $(3+1)$-dimensional case apply here as well regarding the low-energy behavior of the theory (LLL dominance) and the degeneracy per area of the LLL as compared with the other Landau levels. One thing of note, however, is that all particles in the LLL are degenerate, $E_0 = m$, due to the absence of p_z. Furthermore, in the massless limit, $m \to 0$, the energy of this level goes to zero and becomes degenerate with the negative energy state, formally at $E_0 = -m$.

An interesting consequence of $(2+1)$-dimensional Dirac fermions in a constant external magnetic field is the spontanous symmetry breaking characterized by the appearance of a condensate, $\langle\bar{\psi}\psi\rangle$. This is true in the free theory and can be verified by calculating the propagator using the proper-time representation pioneered by Schwinger [29]. As a result, one can calculate the condensate which is given in $(2+1)$ dimensions by [30, 31]

$$\langle\bar{\psi}\psi\rangle = -\frac{1}{2\pi}\left[m\sqrt{2eB}\,\zeta(\tfrac{1}{2}, 1 + \tfrac{m^2}{2eB}) + eB - 2m^2\right], \tag{3.9}$$

where $\Gamma(n)$ is Euler's gamma function. Taking the chiral limit $(m \to 0)$ of (3.9) one obtains

$$\lim_{m\to 0_+} \langle\bar{\psi}\psi\rangle(B,m) = -\frac{eB}{2\pi}, \tag{3.10}$$

while the chiral limit of an analogous expression in $(3+1)$ dimensions gives $\langle\bar{\psi}\psi\rangle \propto m\log m$. This hints that the phenomenon of dynamical symmetry breaking in the presence of an external magnetic field is likely to occur in $(2+1)$ dimensions.

One might initially think that the dimensional reduction, $D \to D-2$, which is at play in magnetic catalysis is at odds with the Mermin-Wagner-Coleman (MWC) theorem [32, 33]. Spontaneous breaking of a continuous symmetry occurs in magnetic catalysis for theories in which the reductions $(3+1) \to (1+1)$ and $(2+1) \to (0+1)$ take place. By Goldstone's theorem, the spontaneous breaking of a continous symmetry implies the existence of massless bosons [34, 35, 36]. However, the MWC theorem states that spontaneous symmetry breaking is not possible in theories of dimension less than $(2+1)$. The resolution of this apparent contradiction comes from the fact that the Nambu-Goldstone (NG) bosons, which appear due to the spontaneous symmetry breaking according to Goldstone's theorem, are charge neutral and thus do not experience a dimensional reduction while the charged fermions and antifermions do. This follows from the fact that a charged particle's motion is constrained in the plane perpendicular to the magnetic field while the motion of the center of mass of the neutral NG bosons is not. A simple argument in the language of first quantization can illustrate this fact [24]. One first defines the components of the canonical momentum operator in the gauge (3.2)

$$\hat{P}_x = -i\frac{\partial}{\partial x},\ \hat{P}_y = -i\frac{\partial}{\partial y} + \hat{Q}Bx,\ \hat{P}_z = -i\frac{\partial}{\partial z}, \tag{3.11}$$

where $\hat{Q}$ is the charge operator and each component commutes with the Hamiltonian. Taking the commutator of each pair of operators one finds

$$\left[\hat{P}_x, \hat{P}_y\right] = -i\hat{Q}B,\ \left[\hat{P}_x, \hat{P}_z\right] = \left[\hat{P}_y, \hat{P}_z\right] = 0. \tag{3.12}$$

From this it is clear that for neutral particles, all of the above commutators are zero, and thus, all three components can be used to describe the dynamics. Thus, the NG boson propagator has the full $(3+1)$ or $(2+1)$-dimensional form in the infrared, which resolves the contradiction with the MWC theorem.

3.2 Magnetic Catalysis and Applications

Various field theories and condensed matter systems have been predicted to exhibit magnetic catalysis. Originally, the authors [21, 22, 23, 24] considered the NJL model, as it was known to exhibit chiral symmetry breaking even without the external magnetic field. After grasping the physics of the problem, in particular the concept of dimensional reduction, the authors proposed that the phenomenon was in fact universal and carried out studies of QED and eventually graphene.

3.2.1 NJL Model and QED

First introduced as a model involving the nucleons and the pions, the NJL model exhibits dynamical symmetry breaking. The chiral symmetry is broken via an effective four-fermion interaction. The mechanism by which the chiral symmetry breaks is similar to that in the BCS theory of superconductivity. The point-like interaction between fermions and antifermions leads to a condensation of fermion-antifermion pairs in the vacuum and implies the breaking of chiral symmetry and the generation of a dynamical fermion mass.

Knowing that external fields stabilize the condensate in the broken phase [37], one might wonder how the phase diagram of the theory is changed in the presence of an external magnetic field. One may start with a $U(1)_{\mathrm{V}} \times U(1)_{\mathrm{A}}$ invariant NJL Lagrangian in $(3+1)$ dimensions

$$\mathcal{L} = \frac{1}{2}\bar{\psi}i\not{D}\psi + \frac{G}{2}\left[(\bar{\psi}\psi)^2 + (\bar{\psi}i\gamma_5\psi)^2\right], \tag{3.13}$$

where one considers fermions with an additional "color" index $\alpha = 1, 2, \dots N_c$. The reason for adding this extra index will be seen later on when one considers the large N_c limit ($N_c \to \infty$). This Lagrangian is invariant under the following transformations

$$U(1)_{\mathrm{V}}: \ \psi \to e^{i\alpha}\psi, \ \bar{\psi} \to \bar{\psi}e^{-i\alpha}, \tag{3.14}$$

$$U(1)_{\mathrm{A}}: \ \psi \to e^{i\alpha\gamma_5}\psi, \ \bar{\psi} \to \bar{\psi}e^{i\alpha\gamma_5}. \tag{3.15}$$

One can rewrite the Lagrangian in (3.13) by introducing two auxiliary fields σ and π via the Hubbard-Stratonovich transformation [38], [39]

$$\mathcal{L} = \frac{1}{2}\bar{\psi} i \not{D} \psi - \bar{\psi}(\sigma + i\gamma_5\pi)\psi - \frac{1}{2G}(\sigma^2 + \pi^2). \tag{3.16}$$

Using the equations of motion one can derive the following relations

$$\sigma = -G(\bar{\psi}\psi), \ \pi = -G(\bar{\psi}i\gamma_5\psi). \tag{3.17}$$

To examine the ground state properties of the theory one may calculate the effective potential. Considering only spatially uniform configurations in the large N_c limit, the authors of [21, 22, 23, 24] obtained the following gap equation

$$\rho\Lambda^2\left(\frac{1}{g} - 1\right) = -\rho^3 \ln\tfrac{(\Lambda l)^2}{2} + \gamma\rho^3 + l^{-2}\rho\ln\tfrac{(\rho l)^2}{4\pi} + 2l^{-2}\rho\ln\Gamma(\tfrac{\rho^2 l^2}{2}), \tag{3.18}$$

where the dimensionless coupling constant $g \equiv \frac{N_c G \Lambda^2}{4\pi^2}$, is introduced. Taking the limit $B \to 0$ ($l \equiv |eB|^{-1/2} \to \infty$), one can recover the familiar gap equation for the NJL model

$$\rho\Lambda^2\left(\frac{1}{g} - 1\right) = -\rho^3 \ln\tfrac{\Lambda}{\rho^2}. \tag{3.19}$$

One notes that a nontrivial solution of (3.19) only appears when $g > g_c = 1$, as can be easily verified by verifying that sign of the right hand side is always negative while that of the left hand side depends on the value of the coupling g. Thus one sees that spontaneous symmetry breaking is strictly a strong coupling phenomenon in the NJL model without an external magnetic field. However, for the gap equation in (3.18), one can obtain a nontrivial solution $\bar{\rho} \equiv \sigma = m_{\mathrm{dyn}}$ even in the weak coupling regime $g \ll g_c$. In this regime, one obtains a dynamical mass of the form

$$m^2_{\mathrm{dyn}} = \frac{eB}{\pi} e^{-\frac{4\pi^2(1-g)}{|eB|N_c G}}. \tag{3.20}$$

From the form of (3.20), one notices that an essential singularity exists at $G = 0$ and thus the result is nonanalytic in the coupling. This is a sign that the generation of the dynamical fermion mass is a truly nonperturbative phenomenon. It has been shown that the dominant contribution to this result comes from the LLL [24], further corroborating the intuition gained from the free Dirac theory in an external field. One also notes that this form for the dynamical fermion mass closely resembles the result obtained in the $(1+1)$ Gross-Neveu model [40], [41]

$$m_{\text{dyn}}^2 = \Lambda^2 e^{-\frac{2\pi}{N_c G_0}}, \tag{3.21}$$

where G_0 is the coupling and Λ is the momentum space cutoff. This fact further supports the claim of dimensional reduction $D \to D-2$ as one has a form for the dynamical mass in the $(3+1)$ NJL model which mirrors that of the $(1+1)$ Gross-Neveu model. One can also ask how the condensate is enhanced by the magnetic field for strong couplings $g > g_c$? In this regime one finds that for sufficiently weak fields the dynamical mass takes the form

$$m_{\text{dyn}}^2 \simeq (m_{\text{dyn}}^{(0)})^2 \left[1 + \frac{|eB|^2}{3(m_{\text{dyn}}^{(0)})^4 \ln(\Lambda/m_{\text{dyn}}^{(0)})^2}\right], \tag{3.22}$$

where $m_{\text{dyn}}^{(0)}$ refers to the solution of (3.19).

The NJL model in $(2+1)$-dimensions in the presence of an external magnetic field can be studied with the same methods used in the $(3+1)$-dimensional version. Due to the necessity of using a reducible representation of the Dirac algebra as discussed in the previous chapter, one finds that the kinetic term has a $U(2)$ flavor symmetry. One can then construct a four-fermion interaction term which is also invariant under the action of the flavor symmetry, leading to the following

$$\mathcal{L} = \bar{\psi} i \not{D} \psi + \frac{G}{2}\left[(\bar{\psi}\psi)^2 + (\bar{\psi}\tilde{\gamma}^4\psi)^2 + (\bar{\psi}i\tilde{\gamma}^5\psi)^2\right], \tag{3.23}$$

where the conventions for the gamma matrices in (2.3) have been used. The appearance of a mass for the Dirac fermion will break the $U(2)$ symmetry down to a $U(1) \times U(1)$ subgroup, leading to the appearance of NG bosons. The gap equation in this case takes the form

$$2\Lambda l \left(\frac{1}{g} - \frac{1}{\sqrt{\pi}}\right)\rho = \frac{1}{l} + \sqrt{2}\rho\zeta(-\tfrac{1}{2}, \tfrac{(\rho l)^2}{2} + 1) + O(1/\Lambda). \tag{3.24}$$

In the limit $B \to 0$ one obtains an expression that only admits a nontrivial value for the dynamical mass when the coupling is sufficiently strong, $g > g_c \equiv \sqrt{\pi}$. The external magnetic field causes a dynamical mass to be generated even as $g \to 0$,

$$m_{\text{dyn}} = \bar{\rho} \simeq G N_c \frac{|eB|}{2\pi}. \tag{3.25}$$

This can be understood as the mean field value defined by $m_{\text{dyn}} = \langle 0|\sigma|0\rangle = -G\langle 0|\bar{\psi}\psi|0\rangle$. Using the expression for $\langle\bar{\psi}\psi\rangle$ calculated in the free theory (3.10), one obtains the above result (including a factor of N_c). Furthermore, one notices that the expression in (3.25) is analytic in G, as opposed to the result obtained in (3.20). This suggests that perturbation theory is valid at weak coupling in $(2+1)$ dimensions.

Given that magnetic catalysis seems to rest upon general physical principles, one might also ask whether it applies to gauge theories with long-range interactions such as QED. In QED, one can study the bound state equation describing the NG boson in a magnetic field. The formalism involves the Schwinger-Dyson equations, in particular the Bethe-Salpeter equation (BSE). Using the BSE, one can transform the relativistic bound-state problem to a two-dimensional Schrödinger-like equation. The result for the dynamical mass in $(3+1)$ QED takes the form

$$m \simeq \sqrt{|eB|}F(\alpha)e^{-\frac{\pi}{\alpha \ln(C/N_f\alpha)}}, \tag{3.26}$$

where C is a constant of $O(1)$ and $F(\alpha) \propto (N_f\alpha)^{1/3}$. One notices that this has the same nonanalytic dependence on the coupling constant at $\alpha = 0$ as would the energy of the ground state of a Schrödinger equation in two dimensions [42]. This makes clear the relationship with dimensional reduction as a result of an external magnetic field.

3.2.2 Graphene and Condensed Matter Systems

In the presence of an external magnetic field, graphene exhibits an anomalous quantum Hall effect [43, 44], which is well understood from a theoretical point of view [45]. Assuming that electron states which lie between Landau levels (LL) are localized due to disorder and that the Fermi energy lies between Landau levels, the contribution to the Hall conductivity, σ_{xy}, comes from each filled LL. Accounting for the additional four-fold degeneracy due to the spin and valley degrees of freedom, one obtains

$$\sigma_{xy} = \nu\frac{e^2}{h}, \tag{3.27}$$

where

$$\nu = 4\left(N + \frac{1}{2}\right) \tag{3.28}$$

is the filling factor. Here N is an integer and the additional 1/2 is due to the zero-energy LL which shared equally between electrons and holes. Thus, plateaus are expected to appear at half-integer values of σ_{xy} as the carreir concentration is varied. Experimentally, this is exactly what happens. For the case of bilayer graphene, the zero-energy level has double the occupation as the single-layer case, and thus the plateaus appear at integer values with the caveat that there is no plateau at zero. One can begin to see from the above discussion that the zero-energy level plays a crucial role in the observable properties of graphene in a magnetic field.

In strong magnetic fields ($B \sim 45$ T), there appear additional Hall plateaus associated with the breaking of the four-fold degeneracy of each LL [46]. The additional plateaus appearing at $\nu = 0, \pm 1$ are due to the splitting of the degeneracy of the LLL. The charge-neutral state, $\nu = 0$, which one can access in lattice calculations at zero chemical potential, is predicted to support a time-reversal odd, Haldane mass $\Delta_H \bar{\psi} \tilde{\gamma}_{4,5} \psi$ [47, 48, 49, 50]. This mass is a singlet under $SU(2)_\sigma$, whose generators are given by

$$\tilde{\gamma}_4 \otimes P_\sigma, \quad i\tilde{\gamma}_5 \otimes P_\sigma, \quad \tilde{\gamma}_{4,5} \otimes P_\sigma, \tag{3.29}$$

where the spin projection operator, $P_\sigma \equiv \frac{1}{2}(1 \pm \sigma_3)$, has been introduced. The regular Dirac mass is a triplet with respect to $SU(2)_\sigma$ and breaks this symmetry to $U(1)_\sigma$ with the generator $\tilde{\gamma}_{4,5} \otimes \mathbf{1}$.

In the full continuum theory, an additional Zeeman term is needed to describe the interaction of the electron's magnetic moment with the external magnetic field. This term takes the form

$$\mathcal{H}_Z = -\mu_B B \int d\vec{r}\ \psi^\dagger \sigma_3 \psi, \tag{3.30}$$

where μ_B is the Bohr magneton and σ_3 acts in spin space. Including this term explicity breaks the $U(4)$ symmetry to $U(2)_\uparrow \otimes U(2)_\downarrow$, whose generators are given by those in (3.29), with the addition of $\mathbf{1} \otimes P_\sigma$. However, although (3.30) lifts the spin degeneracy of each LL, this perturbation is extremely small even in the presence of large magnetic fields. This can be observed by noting

$$\begin{aligned} \epsilon_Z &\equiv \mu_B B = 5.8 \times 10^{-2} B[\mathrm{T}]\ \mathrm{meV}, && (3.31) \\ \epsilon_B &\equiv \sqrt{\hbar v_F^2 |eB|/c} = 26\sqrt{B[\mathrm{T}]}\ \mathrm{meV}, && (3.32) \end{aligned}$$

where ϵ_B is the Landau energy and ϵ_Z is the Zeeman energy. For even the strongest magnetic fields available in the laboratory ($B \sim 45$ T), ϵ_Z is only a fraction of ϵ_B. For the results in this thesis, the Zeeman term has not been taken into account and thus the continuum graphene EFT possesses the full $U(4)$ symmetry.

Apart from the long-range Coulomb interaction considered in the continuum EFT presented in (2.1), (2.9), and (2.10), the complete hexagonal lattice theory includes numerous short-range electron-electron interactions. These lattice-scale interaction terms are allowed by the point group symmetry of the underlying hexagonal lattice, C_{6v} [51]. As a result, these terms break the much larger $U(4)$ symmetry present in the continuum EFT. The couplings associated with these terms can vary in sign and are strongly renormalized at energies on the order of the bandwidth, v_F/a, where a is the spacing of the hexagonal lattice [52]. Taking these renormalized couplings into account can have a decisive effect on the selection of the ground state in the full theory. As with the Zeeman interaction, this thesis will neglect these lattice-scale interactions.

As first pointed out in [53, 47], and later in [48, 49], magnetic catalysis is thought to be responsible for the lifting of the degeneracy of the first two Landau levels and thus the appearance of the additional plateaus in the Hall conductivity that were observed in [46]. The authors of [48] considered the fermion gap equation in the Hartree-Fock approximation

$$\begin{aligned}\big(G(u,u')\big)^{-1} &= \Big(G^{(0)}(u,u')\Big)^{-1} + ig_{int}\gamma^0 G(u,u)\gamma^0\delta^{(3)}(u-u') \\ &- ig_{int}\gamma^0 \,\mathrm{Tr}\,\big[\gamma^0 G(u,u)\big]\,\delta^{(3)}(u-u'), \qquad (3.33)\end{aligned}$$

where $u \equiv (\vec{r},t)$, and a contact interaction has been used, $g_{int}\delta(\vec{r})$. In (3.33), $G(u,u') = \langle 0|\mathrm{T}\Psi(u)\bar{\Psi}(u')|0\rangle$ represents the full quasiparticle propagator and $G^{(0)}(u,u')$ represents the bare quasiparticle propagator. The gap equation represents a self-consistent method for determining the various condensates.

For the plateau at $\nu = 0$, which corresponds to a half-filled LLL, there are several different solutions of the gap equations. The ground state is identified by computing the free energy associated with each solution. It turns out that for chemical potential sufficiently near the Dirac point, the ground state is the so-called singlet solution

$$\tilde{\Delta}_\uparrow = \tilde{\Delta}_\downarrow = 0,\ \Delta_\uparrow = -\Delta_\downarrow = M, \qquad (3.34)$$

where $\tilde{\Delta}_\sigma$ corresponds to the Dirac mass which is a triplet under $SU(2)_\sigma$, and Δ_σ corresponds to the Haldane mass which is a singlet under $SU(2)_\sigma$. In (3.34) the dynamically generated mass scale $M = \sqrt{\pi}\lambda\epsilon_B/(4(1-\lambda))$ is introduced where $\lambda \equiv g_{int}\epsilon_B/(4\pi^{3/2}v_F^2)$.

As mentioned previously, the Zeeman term is a symmetry breaking term which explicitly breaks the $U(4)$ symmetry of the EFT down to $U(2)_\uparrow \times U(2)_\downarrow$. From the form of the solutions in (3.34), where the two singlet masses have opposite signs, one can see that this symmetry breaking is enhanced. In Fig. 3(b) of [48], which plots the order parameters of the singlet solution versus temperature, one can see a crossover as T becomes greater than the dynamical mass scale, M. For small chemical potentials, the solution closest in energy to the singlet solution is the triplet solution, as one can see in Fig. 2(b) of [48]. The authors calculate the difference and show that

$$\delta\Omega = \Omega_{S1} - \Omega_T = -\frac{\epsilon_Z eB}{\pi\hbar c}, \qquad (3.35)$$

where “S1” refers to the singlet solution and “T” refers to the triplet solution. One notices that as the Zeeman energy vanishes ($\epsilon_Z \to 0$), these solutions become degenerate. Another consequence of vanishing Zeeman energy can be seen in Fig. 3(a) of [48], which plots the order parameters of the singlet solution versus temperature in the absence of Zeeman splitting. One can see that without including the explicit symmetry breaking term, a phase transition occurs at $T \approx 0.9M$.

Including a more realistic, long-range interaction complicates the gap equation. Due to the nontrivial momentum dependence of the Coulomb interaction, one must introduce various wavefunction renormalizations. In [49], the authors find that the singlet solution described by (3.34) is still the ground state in the presence of Zeeman splitting and is degenerate with the triplet solution in the absence of Zeeman splitting. However, there is one qualitative difference with the solutions obtained with the contact interaction. In the presence of long-range, unscreened Coulomb interactions, the gap parameters decrease with increasing LL index n, leading to the existence of ”running gaps”. It is of importance to this thesis that the ground state of the graphene EFT be characterized using nonperturbative methods and compared to the results of [48, 49].

CHAPTER 4

INTRODUCTION TO LATTICE FIELD THEORY

In this chapter, the path integral approach to quantization, first introduced by Feynman [54], will be discussed. A simple bosonic system, the relativistic scalar field, will be studied via the path integral. Fermions will be incorporated into the formalism by introducing the Grassmann calculus. After discussing the interpretation of the Euclidean path integral as a statistical model for the given field theory, one is introduced to the lattice as a means of regulating ultraviolet divergences. From here, one can discretize the continuum graphene EFT introduced earlier and discuss the advantages and limitations of such a formulation.

4.1 The Path Integral

Originally carried out in the context of nonrelativistic quantum mechanics, the path integral represents a view of time evolution as a weighted sum over paths. In this view, complimentary to the commonly used Schrödinger and Heisenberg pictures, each path has an associated weight, $e^{iS/\hbar}$, where S is the action for the given path between the spacetime points (x_i, t_i) and (x_f, t_f). One starts with the transition amplitude given by

$$\langle x_i, t_i | x_f, t_f \rangle = \langle x_i | e^{-i(t_f - t_i)\hat{H}} | x_f \rangle, \tag{4.1}$$

where $\hat{H} = \frac{\hat{p}^2}{2m} + V(\hat{x})$ refers to the Hamiltonian of the system. Due to the fact that the Hamiltonian is a sum of terms which do not commute, one must take care in order to express $e^{-i\hat{H}\tau}$, $\tilde{t} \equiv t_f - t_i$, in a form convenient for calculation of matrix elements. Considering an infinitesimal interval ϵ, one can write the following expression for the time-evolution operator

$$e^{-i\epsilon\hat{H}} = e^{-i\epsilon\hat{V}/2} e^{-i\epsilon\hat{p}^2/2m} e^{-i\epsilon\hat{V}/2} (1 + \mathrm{O}(\epsilon^2)), \tag{4.2}$$

where $\hat{V} \equiv V(\hat{x})$. This form allows us to evaluate matrix elements of the time-evolution operator

$$\langle x | e^{-i\epsilon\hat{H}} | y \rangle \quad = \quad e^{-i\epsilon V(x)/2} \langle x | e^{-i\epsilon\hat{p}^2/2m} | y \rangle e^{-i\epsilon V(y)/2}, \tag{4.3}$$

where the matrix element on the right hand side of (4.3) can be evaluated by gaussian integration yielding

$$\begin{aligned}\langle x|e^{-i\epsilon\hat{p}^2/2m}|y\rangle &= \int\frac{dp}{2\pi}e^{ip(x-y)}e^{-i\epsilon p^2/2m}\\ &= \sqrt{\tfrac{m}{2\pi i\epsilon}}e^{im(x-y)^2/2\epsilon}. \qquad (4.4)\end{aligned}$$

One can construct the time-evolution operator on a finite interval by forming the product of the infinitesimal form in (4.2) which gives the following

$$e^{-i\tilde{t}\hat{H}} = \lim_{N\to\infty}(e^{-i\epsilon\hat{H}})^N, \quad \epsilon = \frac{\tilde{t}}{N}. \qquad (4.5)$$

One then uses this identity in (4.1), and inserting $N-1$ sets of intermediate position states, one obtains

$$\begin{aligned}&\langle x_f|e^{-i\tau\hat{H}}|x_i\rangle = \lim_{N\to\infty}\langle x_f|(e^{-i\epsilon\hat{H}})^N|x_i\rangle\\ &= \lim_{N\to\infty}\int dx_1\dots dx_{N-1}\langle x_f|e^{-i\epsilon\hat{H}}|x_{N-1}\rangle\langle x_{N-1}|e^{-i\epsilon\hat{H}}|x_{N-2}\rangle\dots\langle x_1|e^{-i\epsilon\hat{H}}|x_i\rangle\\ &= \lim_{N\to\infty}C^N\int dx_1\dots dx_{N-1}\exp\left[i\epsilon\sum_{j=0}^{N-1}\left(\tfrac{m}{2}\tfrac{(x_{j+1}-x_j)^2}{\epsilon^2}-\tfrac{1}{2}(U(x_j)+U(x_{j+1}))\right)\right],\end{aligned}$$

where $x_0\equiv x_i$, $x_N\equiv x_f$, and $C=\sqrt{\frac{m}{2\pi i\epsilon}}$. Taking the continuum limit, $\epsilon\to 0$, one can write (4.6) in the following, more physically intuitive form

$$\langle x_f|e^{-i\tau\hat{H}}|x_i\rangle = \int\mathcal{D}[x(t)]e^{i\int_{t_i}^{t_f}dtL(x,\dot{x})} \qquad (4.6)$$

where we have introduced the measure, $\mathcal{D}[x(t)] \equiv \lim_{N\to\infty}C^N\prod_1^{N-1}dx_i$, and the Lagrangian, $L(x,\dot{x})=\frac{1}{2}m\dot{x}^2-V(x)$. The argument of the exponent, $S=\int_{t_i}^{t_f}dtL(x,\dot{x})$, is the classical action of the path taken from $\{x_i,t_i\}$ to $\{x_f,t_f\}$. Thus, one is led to the interpretation of (4.6) as a weighted average of paths connecting the fixed end points, with e^{iS} ($\hbar=1$) the weight associated with each path. The dominant contributions to the path integral come from the classical trajectories, as they correspond to the extrema of the action, $\frac{\delta S}{\delta x}=0$. One is then led to interpret the trajectories that deviate from the classical ones as the quantum fluctuations.

Although one can make use of this form of the path integral, one notices that the integrand is oscillatory. A more useful form for what follows can be obtained by making a Wick rotation to Euclidean space, $t\to -i\tau$, replacing e^{iS} with e^{-S_E}, where
$S_E=\int d\tau(\frac{1}{2}\dot{x}^2+V(x))$. In this way, deviations from the classical trajectory are exponentially suppressed, the integrand is real, and one can intepret the integrand as a probabilistic weight, making it suitable for numerical calculations.

The usefulness of the Euclidean path integral manifests itself in the way one can use it to express thermal expectation values. Recalling from quantum statistical mechanics that for a system at temperature $T = 1/\beta$, whose dynamics are governed by a Hamiltonian $\hat{H}$, the thermal expectation value of an observable $\mathcal{O}$ can be calculated as follows

$$\begin{aligned} \langle \mathcal{O} \rangle_T &\equiv Z^{-1}\,\mathrm{Tr}\,\{e^{-\beta\hat{H}}\mathcal{O}\}, && (4.7) \\ Z &\equiv \mathrm{Tr}\; e^{-\beta\hat{H}} && (4.8) \end{aligned}$$

where the trace is typically calculated using the complete set of eigenstates of $\hat{H}$, and Z is referred to as the partition function. Vacuum expectation values can be obtained in this formalism by applying the limit $\beta \to \infty$. Anticipating the observables of interest in a lattice field theory, one considers the following vacuum expectation value

$$\begin{aligned} G(\tau_1, \tau_2, \ldots, \tau_n) &= \lim_{\tau \to \infty} Z^{-1}\mathrm{Tr}\{e^{-\tau\hat{H}}\hat{x}(\tau_1)\hat{x}(\tau_2)\ldots\hat{x}(\tau_n)\} \\ &= \langle 0|\hat{x}(\tau_1)\ldots\hat{x}(\tau_n)|0\rangle, \qquad (4.9) \end{aligned}$$

where the state $|0\rangle$ refers to the ground state of $\hat{H}$ and the position operators are written in the Heisenberg representation, $\hat{x}(\tau_i) = e^{\tau_i\hat{H}}\hat{x}e^{-\tau_i\hat{H}}$. Taking the trajectories in our Euclidean path integral to be periodic, one can express thermal expectation values in the language of path integrals

$$\langle 0|\hat{x}(\tau_1)\hat{x}(\tau_2)\ldots\hat{x}(\tau_n)|0\rangle = \frac{\int \mathcal{D}[x]x(\tau_1)\ldots x(\tau_n)e^{-S_E[x]}}{\int \mathcal{D}[x]e^{-S_E[x]}}, \qquad (4.10)$$

where the $x(\tau_i)$ in the integrand on the right hand side are numbers and not operators. Considering the right hand side of (4.10), one notices that it has the form of a Boltzmann distribution with $e^{-S_E[x]}$ replacing the familiar $e^{-\beta H}$. Thus, one can clearly see the connection between path integrals and quantum statistical mechanics.

One can generalize the previous discussion to the context of a field theory by making the identification $x(\tau) \to \phi(x)$, where $\phi(x)$ is a spin-0 bosonic field. In particular one can take the Klein-Gordon field which is described by the following action

$$S_E = \int d^d x \frac{1}{2}\Big[(\partial_\mu\phi)^2 + m^2\phi^2\Big]. \qquad (4.11)$$

The form of the correlation functions, $G(x_1, x_2, \ldots, x_n)$, can be read off from (4.10)

$$\begin{aligned} G(x_1, x_2, \ldots, x_n) &\equiv \langle\phi(x_1)\phi(x_2)\ldots\phi(x_n)\rangle = \frac{\int \mathcal{D}\phi\phi(x_1)\ldots\phi(x_n)e^{-S_E[\phi]}}{\int \mathcal{D}\phi e^{-S_E[\phi]}}, \qquad (4.12) \\ \mathcal{D}\phi &\equiv \lim_{N\to\infty}\prod_{i=1}^{N} d\phi_i, \end{aligned}$$

where the number of spacetime points, N, is taken to infinity in the continuum. The calculation of correlation functions is aided by the introduction of the generating functional. This is done by introducing a source J which couples linearly to the field ϕ, yielding

$$\begin{aligned} Z_0[J] &= \int \mathcal{D}\phi e^{-\frac{1}{2}\phi_i A_{ij}\phi_j + J_i\phi_i} \\ &= Z_0[0] e^{\frac{1}{2}J_i A^{-1}_{i,j} J_j}, \end{aligned} \tag{4.13}$$

where the index i is a generic label and one generalizes the Gaussian integral used in (4.4). One then computes correlation functions using the following identity

$$\langle \phi_1 \phi_2 \ldots \phi_n \rangle = \left(\frac{1}{Z_0[J]} \frac{\delta^n Z_0[J]}{\delta J_1 \delta J_2 \ldots \delta J_n} \right)_{J=0} \tag{4.14}$$

For an interacting theory, one can write the action as $S[\phi] = S_0[\phi] + S_{int}[\phi]$, where S_0 characterizes the free theory which is quadratic in the fields and $S_{int}[\phi]$ represents the interactions. One can then introduce interactions by writing

$$\begin{aligned} Z[J] &= \sum_k \frac{(-1)^k}{k!} \int \mathcal{D}\phi (S_{int}[\phi])^k e^{-\frac{1}{2}\phi_i A_{ij}\phi_j + J_i\phi_i} \\ &= \sum_k \frac{(-1)^k}{k!} (S_{int}[\tfrac{\delta}{\delta J}])^k Z_0[J], \end{aligned} \tag{4.15}$$

and the correlation functions in the interacting theory can be calculated by using $Z[J]$ in (4.14).

Incorporating fermions into the path integral is a bit more difficult as one needs to take into account statistics. Namely, correlation functions of fermionic operators should be antisymmetric under the interchange of quantum numbers. This is done by introducing Grassman variables $\psi_i, \bar{\psi}_i$ which satisfy

$$\{\psi_i, \psi_j\} = \{\bar{\psi}_i, \bar{\psi}_j\} = \{\psi_i, \bar{\psi}_j\} = 0. \tag{4.16}$$

The rules for integration and differentiation of Grassmann variables are given by [55]

$$\int d\psi_i = 0, \quad \int d\psi_i \psi_j = \delta_{ij}, \tag{4.17}$$

$$\frac{d}{d\psi_i} 1 = 0, \quad \frac{d}{d\psi_i}\psi_j = \delta_{ij}. \tag{4.18}$$

These rules make differentiation and integration of a function with respect to the ψ_i relatively easy. One particularly useful application is the evaluation of a Gaussian integral with Grassmann variables

$$Z_F = \int d\bar{\psi}_N d\psi_N \ldots d\bar{\psi}_1 d\psi_1 e^{-\sum_{i,j=1}^{N} \bar{\psi}_i M_{ij} \psi_j} = \det[M]. \tag{4.19}$$

One can also introduce anticommuting sources for the fields $\{\eta_i, \bar{\eta}_i\}$. Using the above identity, one can then introduce the generating functional for a system of free fermions

$$\begin{aligned} Z_F[\eta, \bar{\eta}] &= \int \mathcal{D}\bar{\psi}\mathcal{D}\psi e^{-\bar{\psi}_i M_{ij}\psi_j + \bar{\eta}_i\psi_i + \bar{\psi}_i\eta_i} \\ &= Z_F[0,0] e^{\bar{\eta}_i M_{ij}^{-1}\eta_j}. \end{aligned} \tag{4.20}$$

Proceeding as in the bosonic case, one can compute correlation functions of the Grassmann variables by taking derivatives of the generating functional with respect to the sources

$$\begin{aligned} \langle \psi_1\psi_2\ldots\psi_n\bar{\psi}_{n+1}\bar{\psi}_{n+2}\ldots\bar{\psi}_{2n}\rangle &= Z_F^{-1}\int\left(\prod_{k=1}^{N} d\bar{\psi}_k d\psi_k\right)\psi_1\ldots\bar{\psi}_{2n} e^{-\bar{\psi}_i M_{ij}\psi_j} && (4.21) \\ &= (-)^n\left(\frac{1}{Z_F[\eta,\bar{\eta}]}\frac{\delta^{2n} Z_F[\eta,\bar{\eta}]}{\delta\bar{\eta}_1\ldots\delta\eta_{2n}}\right)_{\eta=\bar{\eta}=0}. && (4.22) \end{aligned}$$

One can see that in order for the correlation function to be nonvanishing, an equal number of ψ_i and $\bar{\psi}_i$ must appear.

4.2 Introducing the Lattice

One needs to give a more precise meaning to the path integral expressions in the previous section. In particular, in order to calculate observables in a quantum field theory, one needs an ultraviolet regulator. The regulator allows one to obtain finite expressions free of infinities. In continuum field theory, dimensional regularization and Pauli-Villars regularization are popular choices. One can also introduce a hypercubic spacetime lattice with spacing a and points labeled by $n \equiv (n_1, n_2, n_3, n_4)$ which serves as a regulator, as all momenta will now have an upper limit, $|k_\mu| \leq \pi/a$.

To translate a continuum theory to the lattice, the field, $\phi(x)$, let us say, is now defined at the sites of the lattice, $\phi_n \equiv \phi(na)$, the integral in the action becomes a sum and the measure is $\mathcal{D}\phi \equiv \prod_n d\phi_n$. One also needs to replace the derivative in the kinetic term of (4.11) with a finite difference in order to obtain the lattice action

$$S_E = a^4 \sum_n \frac{1}{2}\left[-\phi_n \sum_\mu \frac{1}{a^2}(\phi_{n+\hat{\mu}} + \phi_{n-\hat{\mu}} - 2\phi_n) + m^2\phi_n^2\right] \tag{4.23}$$

The expression has the correct (naive) cotinuum limit, $a \to 0$, as one can explicitly verify. One can see that this theory correctly describes a spinless particle of mass m by examining the propagator. One first uses the identity

$$\langle \phi_n\phi_m\rangle = \left(\frac{1}{Z}\frac{\delta^2 Z}{\delta J_n \delta J_m}\right)_{j=0} = A^{-1}_{n,m}, \tag{4.24}$$

where (4.13) was used to express the propagator in terms of the inverse of A. By inspection of (4.23) one can see that

$$A_{n,m} = \sum_{\mu} \left(-\delta_{n,m+\hat{\mu}} - \delta_{n,m-\hat{\mu}} + 2\delta_{n,m}\right) + m^2\delta_{n,m}. \tag{4.25}$$

Calculating the inverse of A, defined by $\sum_{p} A_{n,p}A^{-1}_{p,m} = \delta_{n,m}$, is easiest in momentum-space where one has

$$A_{n,m} = \int_{-\pi/a}^{\pi/a} \frac{d^4k}{(2\pi)^4} e^{i\hat{k}(n-m)} \tilde{A}(k), \tag{4.26}$$

as well as the identity

$$\delta_{n.m} = a^4 \int_{-\pi/a}^{\pi/a} \frac{d^4k}{(2\pi)^4} e^{i\hat{k}(n-m)}, \tag{4.27}$$

where $\hat{k}_\mu \equiv ak_\mu$. Using the above relations, one obtains

$$\tilde{A}(k) = \frac{4}{a^2}\sum_{\mu} \sin^2\left(\hat{k}_\mu/2\right) + m^2. \tag{4.28}$$

From here, referring back to (4.24), one arrives at the following form for the propagator

$$\langle\phi_n\phi_m\rangle = \int_{-\pi/a}^{\pi/a} \frac{d^4k}{(2\pi)^4} \frac{e^{i\hat{k}\cdot(n-m)}}{\sum_\mu \tilde{k}_\mu^2 + m^2}, \tag{4.29}$$

where $\tilde{k}_\mu \equiv \frac{2}{a}\sin\frac{k_\mu a}{2}$. One can examine the large $\tau \equiv (n_0 - m_0) > 0$ behavior of the propagator by performing the integral over dk_0. To do so, one considers

$$\begin{aligned} I &= \int_{-\pi}^{\pi} \frac{d\hat{k}_0}{2\pi} \frac{e^{i\hat{k}_0\tau}}{2b - \cos\hat{k}_0}, \\ b &\equiv 1 + \frac{1}{2}\left(m^2 + \sum_i \tilde{k}_i^2\right). \end{aligned} \tag{4.30}$$

One then makes the change of variables, $z = e^{i\hat{k}_0}$, and (4.30) becomes a counter-clockwise contour on the unit circle

$$I = -\oint \frac{dz}{2\pi i} \frac{z^\tau}{z^2 - 2bz + 1}, \tag{4.31}$$

where the integrand has two simple poles at $z_\pm = b \pm \sqrt{b^2-1}$. One can express the poles as $z_\pm = e^{\pm\omega}$, where $\omega = \log\left(b + \sqrt{b^2-1}\right)$. The integral can be evaluated by the method of residues by noting that the contour encloses z_-, yielding the result

$$I = \frac{e^{-\omega\tau}}{2\sinh(\omega)}. \tag{4.32}$$

Inserting this result into the expression for the progator in (4.29), one obtains, in lattice units,

$$\langle \phi_n \phi_m \rangle = \int_{-\pi}^{\pi} \frac{d^3k}{(2\pi)^3} \frac{e^{i\hat{k}_i(n-m)_i - \omega\tau}}{2\sinh\omega}, \tag{4.33}$$

where $\omega \to \sqrt{m^2 + \vec{p}^2}$ in the limit $a \to 0$. At large τ, the correlation function decays as $e^{-m\tau}$, which imples the system has a correlation length $\xi = 1/m$.

Unlike the previous example of the free scalar field, the discretization of the Dirac equation on the lattice is a tricky endeavor. A naive discretization entails replacing the derivative with a symmetric finite difference, yielding the following expression

$$S_E = a^4 \sum_n \left[\frac{1}{2a} \sum_\mu \bar{\psi}_n \gamma_\mu (\psi_{n+\hat{\mu}} - \psi_{n-\hat{\mu}}) + m\bar{\psi}_n \psi_n \right]. \tag{4.34}$$

The free fermion propagator can be expressed as the inverse of the Dirac operator using (4.22)

$$G(n-m) = \langle \psi_n \bar{\psi}_m \rangle = -\left(\frac{1}{Z_F[\eta,\bar{\eta}]} \frac{\delta^2 Z_F[\eta,\bar{\eta}]}{\delta\bar{\eta}_n \delta\eta_m} \right)_{\eta=\bar{\eta}=0} = M^{-1}_{n,m}, \tag{4.35}$$

where $M_{n,m}$ is the fermion matrix defined implictly in (4.34). Just as in the bosonic case, one may invert this matrix by going to momentum-space

$$M_{n,m} = \int_{-\pi}^{\pi} \frac{d^4\hat{k}}{(2\pi)^4} e^{i\hat{k}(n-m)} \left(i \sum_\mu \gamma_\mu \sin\hat{k}_\mu + m \right). \tag{4.36}$$

Thus one obtains the momentum-space propagator

$$G(k) = \frac{-ia^{-1} \sum_\mu \gamma_\mu \sin\hat{k}_\mu + m}{m^2 + a^{-2} \sum_\mu \sin^2 \hat{k}_\mu}, \tag{4.37}$$

which characterizes the excitations of our lattice Dirac fermions. One observes that the lattice propagator has the correct naive continuum limit, $a \to 0$

$$\lim_{a\to 0} G(k) \to \frac{-i\sum_\mu \gamma_\mu k_\mu + m}{m^2 + k^2}, \tag{4.38}$$

which is reassuring. However, there exist unwanted degrees of freedom which can be seen by examining the pole structure of the massless lattice propagator

$$G(k)_{m=0} = \frac{-ia^{-1} \sum_\mu \gamma_\mu \sin\hat{k}_\mu}{a^{-2} \sum_\mu \sin^2 \hat{k}_\mu}. \tag{4.39}$$

There is a pole at $p = (0,0,0,0)$, which describes the single continuum fermion. Unlike the continuum, there exist other poles which are located at the corners of the Brillouin zone

$$p = (\frac{\pi}{a},0,0,0), (0,\frac{\pi}{a},0,0), \ldots, (\frac{\pi}{a},\frac{\pi}{a},\frac{\pi}{a},\frac{\pi}{a}). \tag{4.40}$$

These 15 unwanted poles are referred to as doublers. In order to simulate the correct continuum theory, one must find a way to remove the doublers.

A solution proposed by Wilson [56], is to add a term of the form

$$\begin{aligned} m\sum_n \bar{\psi}_n\psi_n &\rightarrow \sum_n \left(m\bar{\psi}_n\psi_n + \sum_\mu \bar{\psi}_n \partial_\mu^2 \psi_n \right) \\ &= \sum_n \left[\left(m + \frac{4r}{a} \right) \bar{\psi}_n\psi_n - \frac{r}{2a} \sum_\mu \left(\bar{\psi}_n\psi_{n+\hat{\mu}} + \bar{\psi}_{n+\hat{\mu}}\psi_n \right) \right], \end{aligned}$$

to the action in (4.34). In momentum space, this has the form of a momentum-dependent mass

$$\mathcal{M}(k) = m + \frac{r}{a} \sum_\mu \left(1 - \cos(\hat{k}_\mu) \right). \tag{4.41}$$

One can see that for the doublers, which have one or more momentum components $k_\mu = \frac{\pi}{a}$, $\mathcal{M}$ is on the order of the momentum cutoff, π/a, as long as $r \neq 0$. In the continuum limit, $a \to 0$, the doublers become infinitely massive and decouple from the theory, leaving only the correct, continuum mode. Although it elegantly solves the doubling problem, Wilson fermions are not invariant under chiral transformations in the massless limit. In fact, the term added to remove the doublers is the reason why this is so. A theorem proved by Nielsen and Ninomiya [57] codifies the difficulties in removing the doublers while also implementing chiral symmetry. This theorem states that, on the lattice, one cannot implement chiral symmetry in a manner which is free of doublers.

In the continuum, chiral symmetry is encoded in the fact that γ_5 anticommutes with the Dirac operator, $\not{D}$. On the lattice, Ginsparg and Wilson [58] proposed that the relationship takes the form

$$\gamma_5 \not{D} + \not{D}\gamma_5 = a\not{D}\gamma_5\not{D}, \tag{4.42}$$

where the right-hand side is nonvanishing and involves a factor of the lattice spacing. Using (4.42), one can define chiral transformations on the fields

$$\begin{aligned} \psi &\rightarrow \exp\left[i\alpha\gamma_5 \left(\mathbf{1} - \tfrac{a}{2}\not{D} \right) \right] \psi, \\ \bar{\psi} &\rightarrow \bar{\psi} \exp\left[i\alpha\gamma_5 \left(\mathbf{1} - \tfrac{a}{2}\not{D} \right) \right], \end{aligned} \tag{4.43}$$

underwhich the massless lattice Dirac action is invariant. One notices that the chiral transformation in (4.43) involves fields at neighboring sights as well as the gauge field, unlike in the continuum, where chirality and chiral rotations are local properties and independent of the gauge field. This class of chiral lattice Dirac operators has a spectrum that consists of pairs of complex-conjugate eigenvalues as well as real eigenvalues corresponding to states with definite chirality. As a result, a lattice equivalent to the Atiyah-Singer index theorem can be proven [59, 60].

In practice, there are two solutions of the Ginsparg-Wilson relation. The earliest known formulation is the overlap operator, which is defined by

$$\not{D}_{ov} = \frac{1}{a}\left(\mathbf{1} + \gamma_5 \mathrm{sgn}[\gamma_5 \not{D}_W]\right), \tag{4.44}$$

where $\not{D}_W$ is the Wilson Dirac operator introduced previously. Although it exhibits nice chiral properties, the use of overlap fermions is costly as one must approximate $\mathrm{sgn}[A] = A\left(A^2\right)^{-1/2}$ by a polynomial or a ratio of polynomials. The other formulation of chiral fermions on the lattice are the so-called domain wall fermions. This involves introducing a five-dimensional Wilson-like theory, whereby in the normal $(3+1)$ dimensions one has chiral fermions. The advantage of this method is that tried and true methods used for Wilson fermions can be extended to domain wall fermions. A drawback, however, is the introduction of an extra lattice dimension, which significantly increases the cost of simulation. The lesson learned from Ginsparg-Wilson fermions is that one must pay a hefty computational price in exchange for their chiral properties.

Another formulation of fermions on the lattice, and one that will be used exclusively in this thesis, are the so-called staggered fermions [61]. Starting from the action in (4.34), one defines a transformation on the fields

$$\psi_n \to \Omega_n \psi_n, \;\; \bar{\psi}_n \to \bar{\psi}_n \Omega_n^\dagger, \tag{4.45}$$

$$\Omega_n \equiv \gamma_0^{n_0}\gamma_1^{n_1}\gamma_2^{n_2}\gamma_3^{n_3}. \tag{4.46}$$

Using the identity

$$\Omega_n^\dagger \gamma_\mu \Omega_{n+\hat{\mu}} \;=\; \eta_\mu(n), \tag{4.47}$$

$$\eta_\mu(n) \;=\; (-)^{n_0+n_1+\cdots+n_{\mu-1}}, \tag{4.48}$$

one can verify that this transformation leaves the action in (4.34) diagonal in spinor space. Thus, one can immediately reduce the number of doublers by a factor of four by simply writing the action in terms of single component spinors, $\chi_n, \bar{\chi}_n$

$$S_F = a^4 \sum_n \left[\frac{1}{2a}\sum_\mu \eta_\mu(n)\bar{\chi}_n(\chi_{n+\hat{\mu}} - \chi_{n-\hat{\mu}}) + m\bar{\chi}_n\chi_n\right]. \tag{4.49}$$

To define electromagnetic interactions of the fermions, one needs a gauge-invariant formulation for the $U(1)$ field that reduces to (2.8) in the naive continuum limit, $a \to 0$. As opposed to the lattice fermion and scalar boson fields, which live at the sites, the gauge field, $U_\mu(n)$, lives on the link connecting sites n and $n+\hat{\mu}$. This field is $U(1)$-valued and is related to the continuum gauge field in the following way

$$U_\mu(n) \equiv e^{-ie\int_n^{n+\hat{\mu}} dz_\mu A_\mu(z)}. \tag{4.50}$$

Using the form by which $A_\mu(z)$ changes under a gauge transformation, $A_\mu \to A_\mu - \frac{1}{e}\partial_\mu \Lambda$, the link transforms as

$$U_\mu(n) \to G(n) U_\mu(n) G^{-1}(n+\hat{\mu}),\ G(n) \equiv e^{i\Lambda(n)}. \tag{4.51}$$

One can verify from the transformation in (4.51) that only closed paths are gauge-invariant. The simplest closed path is the plaquette, which is given by

$$U^{(p)}_{\mu\nu}(n) \equiv U_\mu(n) U_\nu(n+\hat{\mu}) U^\dagger_\mu(n+\hat{\nu}) U^\dagger_\nu(n). \tag{4.52}$$

An acceptable lattice action is thus composed of closed paths constructed from the link variables which reduces to the correct continuum form in the limit $a \to 0$. The simplest form is constructed from the plaquette as follows

$$S_G = \frac{1}{e^2}\sum_n \sum_{\mu<\nu}\left[1 - \mathrm{Re} U^{(p)}_{\mu\nu}(n)\right], \tag{4.53}$$

where "Re" represents the real part. A gauge-invariant interaction with the fermions can be introduced by using a link to connect fermions at different sites in (4.49)

$$S_F = a^4 \sum_n \left[\frac{1}{2a}\sum_\mu \eta_\mu(n) \bar{\chi}_n (U_\mu(n)\chi_{n+\hat{\mu}} - U^\dagger_\mu(n-\hat{\mu})\chi_{n-\hat{\mu}}) + m\bar{\chi}_n \chi_n\right]. \tag{4.54}$$

Using the fact that the fermions transform under a gauge transformation according to $\chi_n \to G(n)\chi_n$, $\bar{\chi}_n \to \bar{\chi}_n G^{-1}(n)$, the action in (4.54) is shown to be gauge-invariant. Expressing the link variable U_μ, in terms of the gauge potential A_μ, and expanding, one obtains the following interaction term

$$S_{int} = a^4 \frac{(-ie)}{2}\sum_n \sum_\mu \eta_\mu(n)\left(\bar{\chi}_n A_\mu(n)\chi_{n+\hat{\mu}} - \bar{\chi}_n A_\mu(n-\hat{\mu})\chi_{n-\hat{\mu}}\right) + \ldots, \tag{4.55}$$

where vertices of higher order in a were neglected. One can verify that (4.55) reduces to the correct form in the naive continuum limit.

In the preceeding discussion, the naive continuum limit, $a \to 0$, has often been referred to. However, this limit is a bit more subtle. Namely, as one goes towards the continuum, one must vary the bare parameters of the theory such that physical observables are independent of a. This implies that our bare parameters are, in fact, complicated functions of the lattice spacing $g(a)$, $m(a)$, $v_F(a)$, etc. In the case of QCD with massless quarks, this dependence is well understood. The "running" of the gauge coupling constant is encapsulated by the beta function

$$\begin{aligned}
\beta(g) &\equiv -\frac{\partial g}{\partial \log a} = -\beta_0 g^3 - \beta_1 g^5 + O(g^7), \\
\beta_0 &= \frac{1}{(4\pi)^2}\left(\frac{11}{3}N_c - \frac{2}{3}n_f\right), \\
\beta_1 &= \frac{1}{(4\pi)^4}\left(\frac{34}{3}N_c^2 - \frac{10}{3}N_c n_f - \frac{N_c^2-1}{N_c}n_f\right),
\end{aligned} \tag{4.56}$$

where $N_c = 3$. After integrating the above equation and then inverting, one obtains the running coupling

$$g(a)^{-2} = \beta_0 \log\left(a^{-2}\Lambda_L^{-2}\right) + \frac{\beta_1}{\beta_0}\log\left(\log\left(a^{-2}\Lambda_L^{-2}\right)\right) + O\left(1/\log\left(a^{-2}\Lambda_L^{-2}\right)\right). \tag{4.57}$$

From the above discussion it is quite clear that as one pushes $\beta \to \infty$, one obtains the true continuum limit, $a \to 0$. In practice one chooses several values of β which give several values of a. Keeping the physical volume constant, $L = aN_s$, $T = aN_\tau$, one can observe the lattice spacing dependence of physical observables and extrapolate them to the continuum.

4.3 Discretizing the Graphene EFT

Using the formalism and techniques introduced in the preceeding section, one can obtain a discretization of the graphene EFT. Under the assumption that we are only working with a Coulombic interaction characterized by the scalar potential A_0, on the lattice one sets the spatial links to unity, $U_i(n) = 1$. Doing so gives an action for the temporal links, $U_0(n)$, given by

$$S_G = \frac{1}{e^2}\sum_n \sum_{i=1}^{3}\left[1 - \mathrm{Re}U_i^{(p)}(n)\right], \; U_i^{(p)}(n) = U_0(n)U_0^\dagger(n+\hat{i}), \tag{4.58}$$

where this formulation of the $U(1)$ gauge action is referred to as the compact formulation. This is due to the fact that the integration in the measure of the path integral is done over a compact group manifold parametrized by an angular variable taking values in the range $[0, 2\pi]$. This formulation has been shown to lead to an unwanted bulk phase transition as a function of the coupling [62], and thus one can alternatively work with the noncompact version. This is obtained by expanding the links in terms of the real-valued potential up to quadratic order

$$S_G^{(NC)} = a_s^3 a_t \frac{\beta}{2}\sum_n \sum_{i=1}^{3}\frac{1}{a_s^2}\left(\theta(n) - \theta(n+\hat{i})\right)^2, \tag{4.59}$$

where $\beta \equiv 1/e^2$ and one has introduced a lattice spacing in the spatial direction, a_s, as well as in the temporal direction, a_t. Noting that the potential, θ, has engineering dimension of 1, one can define a dimensionless field, $\hat{\theta}(n) \equiv a_t\theta(n)$. One then obtains the following

$$S_G^{(NC)} = \frac{a_s}{a_t}\frac{\beta}{2}\sum_n\sum_{i=1}^{3}\left(\hat{\theta}(n) - \hat{\theta}(n+\hat{\imath})\right)^2, \tag{4.60}$$

where the combination $\xi \equiv \frac{a_s}{a_t}$, known as the anisotropy parameter, appears in the action.

Using the staggered fermion formulation, one can discretize the fermionic contribution to the continuum graphene EFT as given in (2.1). One thus obtains

$$\begin{aligned} S_F = a_s^2 a_t \sum_n \Bigg[& \frac{1}{2a_t}\bar{\chi}_n\left(U_0(n)\chi_{n+\hat{0}} - U_0^\dagger(n-\hat{0})\chi_{n-\hat{0}}\right) + \\ & \frac{1}{2a_s}v_F\sum_{i=1,2}\eta_i(n)\bar{\chi}_n\left(\chi_{n+\hat{\imath}} - \chi_{n-\hat{\imath}}\right) + m\bar{\chi}_n\chi_n\Bigg]. \end{aligned} \tag{4.61}$$

The fermion fields have engineering dimension 1, and thus one can define dimensionless fields, $\hat{\chi}_n, \hat{\bar{\chi}}_n \equiv a_s\chi_n, a_s\bar{\chi}_n$. One then can write the fermion action as

$$\begin{aligned} S_F = \sum_n \Bigg[& \frac{1}{2}\hat{\bar{\chi}}_n\left(U_0(n)\hat{\chi}_{n+\hat{0}} - U_0^\dagger(n-\hat{0})\hat{\chi}_{n-\hat{0}}\right) + \\ & \frac{v_F}{2\xi}\sum_{i=1,2}\eta_i(n)\hat{\bar{\chi}}_n\left(\hat{\chi}_{n+\hat{\imath}} - \hat{\chi}_{n-\hat{\imath}}\right) + m\hat{\bar{\chi}}_n\hat{\chi}_n\Bigg], \end{aligned} \tag{4.62}$$

where it is clear that the combination v_F/ξ controls the anisotropy between the spatial and temporal directions. Previous lattice studies have chosen $\xi = v_F$ [19, 20], which removes the Fermi velocity from the action by choosing a large lattice spacing in the temporal direction.

In $(2+1)$-dimensions, each species of staggered fermions describes two identical, four-component Dirac fermions. In the staggered fermion literature, this degree of freedom is referred to as "taste". Thus, the doublers have been reduced from 8 to 2 while still preserving a remnant chiral symmetry. In LQCD simulations, one typically attempts to eliminate this degree of freedom and simulate one staggered fermion species for each physical quark flavor [63]. In the case of graphene, however, this taste degeneracy is a desirable feature, as one is attempting to describe two identical massless Dirac species. The taste degree of freedom becomes more apparent when one performs a change of basis on the one-component fields within a cube

$$u^{\alpha a}(y) = \frac{1}{4\sqrt{2}}\sum_\eta \Gamma_\eta^{\alpha a}\chi_\eta(y), \tag{4.63}$$

$$d^{\alpha a}(y) = \frac{1}{4\sqrt{2}}\sum_\eta B_\eta^{\alpha a}\chi_\eta(y), \tag{4.64}$$

where one has introduced the operators

$$\Gamma_\eta \equiv \sigma_0^{\eta_0}\sigma_1^{\eta_1}\sigma_2^{\eta_2},\; B_\eta \equiv \beta_0^{\eta_0}\beta_1^{\eta_1}\beta_2^{\eta_2},\; \beta_\mu \equiv -\sigma_\mu. \tag{4.65}$$

In the transformations in (4.63) and (4.64), one notes that both irreducible representations of the Clifford algebra appear [64]. Furthermore, one now labels a lattice site by $n_\mu = 2y_\mu + \eta_\mu$, where y_μ is an integer that labels the corner of the cube, and $\eta_\mu = 0, 1$ labels the sites within the cube An analogous expression can be constructed for the transformation of $\bar{\chi}_n$. One can invert the relations in (4.63) and (4.64) to obtain

$$\begin{aligned}\chi_\eta(y) &= \sqrt{2}\sum_{\alpha,a}(\Gamma_\eta^{*\alpha a}u^{\alpha a}(y) + B_\eta^{*\alpha a}d^{\alpha a}(y)), \\ \bar{\chi}_\eta(y) &= \sqrt{2}\sum_{\alpha,a}(\bar{u}^{\alpha a}(y)\Gamma_\eta^{\alpha a} + \bar{d}^{\alpha a}(y)B_\eta^{\alpha a}),\end{aligned} \tag{4.66}$$

where one has employed the identity Tr $(\Gamma_\eta^\dagger\Gamma_{\eta'} + B_\eta^\dagger B_{\eta'}) = 4\delta_{\eta\eta'}$. Using the relation in (4.54), one can rewrite the (2 + 1)-dimensional staggered action. For example, the mass term becomes

$$a^3 m\sum_{y,\eta}\bar{\chi}_\eta(y)\chi_\eta(y) = (2a)^3 m\sum_y\Big(\bar{u}(y)(\mathbf{1}\otimes\mathbf{1})u(y) + \bar{d}(y)(\mathbf{1}\otimes\mathbf{1})d(y)\Big), \tag{4.67}$$

where one has used the following identities

$$\sum_\eta \Gamma_\eta^{\alpha a}\Gamma_\eta^{*\beta b} = \sum_\eta B_\eta^{\alpha a}B_\eta^{*\beta b} = 4\delta_{\alpha\beta}\delta_{ab}, \tag{4.68}$$

$$\sum_\eta \Gamma_\eta^{\alpha a}B_\eta^{*\beta b} = 0. \tag{4.69}$$

The matrix structure in (4.67) represents the tensoring of the spin space with the taste space, both of which are two-dimensional. Rewriting the kinetic term is a bit more difficult. One first expresses the shifted field as

$$\begin{aligned}\chi_{\eta+\hat{\mu}}(y) &= \delta_{\eta_\mu,0}\eta_\mu(\eta)\sqrt{2}\,\mathrm{Tr}\,\Big(\Gamma_\eta^\dagger\gamma_\mu u(y) + B_\eta^\dagger\beta_\mu d(y)\Big) \\ &\quad+\delta_{\eta_\mu,1}\eta_\mu(\eta)\sqrt{2}\,\mathrm{Tr}\,\Big(\Gamma_\eta^\dagger\gamma_\mu u(y+\hat{\mu}) + B_\eta^\dagger\beta_\mu d(y+\hat{\mu})\Big),\end{aligned} \tag{4.70}$$

where one uses the fact that $\Gamma_{\eta\pm\hat{\mu}} = \eta_\mu(\eta)\gamma_\mu\Gamma_\eta$ and $B_{\eta\pm\hat{\mu}} = \eta_\mu(\eta)\beta_\mu B_\eta$. A similar expression can be written for the backwards-shifted field, $\chi_{\eta-\hat{\mu}}(y)$. Putting these expressions into the kinetic term and proceeding exactly as in [65], one obtains the following form of the staggered action

$$\begin{aligned} S_{st} &= (2a)^3 \sum_{y,\mu} \Big\{ \bar{u}(y)(\gamma_\mu \otimes \mathbf{1})\partial_\mu u(y) + \bar{d}(y)(\beta_\mu \otimes \mathbf{1})\partial_\mu d(y) \\ &\quad + a[\bar{u}(y)(\mathbf{1} \otimes \gamma_\mu^T)\partial_\mu^2 d(y) + \bar{d}(y)(\mathbf{1} \otimes \beta_\mu^T)\partial_\mu^2 u(y)] \Big\} \\ &\quad + (2a)^3 m \sum_y [\bar{u}(y)(\mathbf{1} \otimes \mathbf{1})u(y) + \bar{d}(y)(\mathbf{1} \otimes \mathbf{1})d(y)], \end{aligned} \tag{4.71}$$

where γ_μ^T refers to the transpose, and derivative operators now act on a lattice of spacing $2a$

$$\partial_\mu q(y) \equiv \frac{1}{4a}[q(y+\hat{\mu}) - q(y-\hat{\mu})], \tag{4.72}$$

$$\partial_\mu^2 q(y) \equiv \frac{1}{4a^2}[q(y+\hat{\mu}) - 2q(y) + q(y-\hat{\mu})]. \tag{4.73}$$

The spin-taste basis shows that we have two copies of fermions which have two tastes as well as two spin degrees of freedom. Referring back to the arrangement of the origional graphene degrees of freedom in the construction of the four-component spinor (1.28), one can see that the "taste" degree of freedom is associated with the electron's spin. One can further elucidate the contents of the theory by bundling the two copies into a single field. Namely, one defines the four-component Dirac spinor

$$\Psi(y) = \begin{pmatrix} u(y) \\ d(y) \end{pmatrix}. \tag{4.74}$$

Using the reducible set of four-dimensional gamma matrices in (2.2) and (2.3), one can write the staggered action in the spin-taste basis in the following compact form

$$\begin{aligned} S_{st} &= (2a)^3 \sum_{y,\mu} \Big\{ \bar{\Psi}(y)(\tilde{\gamma}_\mu \otimes \mathbf{1})\partial_\mu \Psi(y) + a\bar{\Psi}(y)(\tilde{\gamma}_5 \otimes \sigma_\mu^T)\partial_\mu^2 \Psi(y) \Big\} \\ &\quad + (2a)^3 m \sum_y \bar{\Psi}(y)(\mathbf{1} \otimes \mathbf{1})\Psi(y). \end{aligned} \tag{4.75}$$

One notices that the second derivative term in (4.75), which is suppressed by a factor of the lattice spacing, is not invariant under a unitary rotation in taste space. Thus, one expects that at finite lattice spacing, the taste symmetry of staggered fermions is broken by contributions of $O(a)$.

One would like to know which, if any, continuum symmetries are inherited by (4.62). In the lattice theory, only a residual $U(1) \otimes U(1)_\epsilon$ of the original $U(4)$ symmetry, as decribed by (2.5) and (2.6), remains at zero mass. Using the one-component form of the action in (4.61), these symmetry operations are given by

$$\chi(x) \to \exp(i\alpha)\chi(x), \quad \bar{\chi}(x) \to \bar{\chi}(x)\exp(-i\alpha), \tag{4.76}$$

$$\chi(x) \to \exp(i\beta\epsilon(x))\chi(x), \quad \bar{\chi}(x) \to \bar{\chi}(x)\exp(i\beta\epsilon(x)), \tag{4.77}$$

where $\epsilon(x) \equiv (-1)^{x_0+x_1+x_2}$. In terms of the fields u and d, these become

$$\begin{pmatrix} u \\ d \end{pmatrix} \to \exp(i\alpha)\begin{pmatrix} u \\ d \end{pmatrix}, \quad \begin{pmatrix} \bar{u} & \bar{d} \end{pmatrix} \to \begin{pmatrix} \bar{u} & \bar{d} \end{pmatrix}\exp(-i\alpha), \tag{4.78}$$

$$\begin{aligned} \begin{pmatrix} u \\ d \end{pmatrix} &\to \begin{pmatrix} \cos(\beta) & i\sin(\beta) \\ i\sin(\beta) & \cos(\beta) \end{pmatrix}\begin{pmatrix} u \\ d \end{pmatrix}, \\ \begin{pmatrix} \bar{u} & \bar{d} \end{pmatrix} &\to \begin{pmatrix} \bar{u} & \bar{d} \end{pmatrix}\begin{pmatrix} \cos(\beta) & i\sin(\beta) \\ i\sin(\beta) & \cos(\beta) \end{pmatrix}. \end{aligned} \tag{4.79}$$

Thus, in the lattice theory, the formation of a nonzero value for the condensate, $\langle\bar{\psi}\psi\rangle$, breaks $U(1)_\epsilon$ and leads to the appearance of a single Goldstone boson.

One should also comment on discrete symmetries in (2+1) dimensions. In the continuum, one can define time-reversal as the following transformation on the fermion fields

$$\Psi(t,\vec{x}) \quad \to \quad -i\tilde{\gamma}_5\gamma_1\gamma_2\Psi(-t,\vec{x}), \tag{4.80}$$

$$\bar{\Psi}(t,\vec{x}) \quad \to \quad -i\bar{\Psi}(-t,\vec{x})\gamma_2\gamma_1\tilde{\gamma}_5. \tag{4.81}$$

One can check that this leaves the contimuum Dirac Lagrangian in (2.1) invariant, which follows from $\{\gamma_0, \tilde{\gamma}_4\gamma_1\gamma_2\} = 0$ and $[\gamma_i, \tilde{\gamma}_4\gamma_1\gamma_2] = 0,\ i = 1, 2$.

Before continuing, one should note the differences between Euclidean and Minskowski space with respect to time-reversal. In Minskowski space, for a fermion bilinear of the form $\bar{\Psi}\Gamma\Psi$, due to the fact that time reversal, $\mathcal{T}$, is an antiunitary operator

$$\bar{\Psi}\Gamma\Psi \to \left(\mathcal{T}\bar{\Psi}\mathcal{T}^{-1}\right)\Gamma^*\left(\mathcal{T}\Psi\mathcal{T}^{-1}\right). \tag{4.82}$$

However, in Euclidean space, time is not distiguished from spatial coordinates by a relative minus sign in the metric. The consequence is that, for example in $(3+1)$ dimensions, time-reversal can be defined by the product of three successive reflection operations

$$\begin{aligned} \Psi(x) \quad &\to \quad \gamma_\mu\Psi(P_\mu(x)), \\ \bar{\Psi}(x) \quad &\to \quad \bar{\Psi}(P_\mu(x))\gamma_\mu, \end{aligned} \tag{4.83}$$

where $P_\mu(x)$ reverses the sign of all components except x_μ. Thus, the Euclidean equivalent of time-reversal can be represented by $P_1P_2P_3$. The situation is a bit different in $(2+1)$

dimensions, as (4.80) and (4.81) illustrate. This is due to the fact that two successive reflections about the spatial axes leaves the time coordinate invariant.

Regarding the spinor indices as a row index and the taste indices as a column index, one can project from spin-taste basis to the single-component basis in the following way

$$\chi_\eta(y) = \sqrt{2}\,\mathrm{Tr}\left\{\left(\Gamma^\dagger_\eta,\ B^\dagger_\eta\right)\left(\begin{array}{c} u(y) \\ d(y) \end{array}\right)\right\}. \tag{4.84}$$

Examining the continuum form of time-reversal in $(2+1)$ dimensions given in (4.80) and (4.81), one supposes that it acts in the same way on the four-component spinor in (4.74)

$$\begin{aligned} \Psi(y_0,\vec{y}) &\rightarrow \tilde{\gamma}_5\gamma_1\gamma_2\Psi(-y_0,\vec{y}), & (4.85)\\ &= \left(\begin{array}{cc} 0 & i\sigma_0 \\ -i\sigma_0 & 0 \end{array}\right)\left(\begin{array}{c} u(-y_0,\vec{y}) \\ d(-y_0,\vec{y}) \end{array}\right), \\ &= \left(\begin{array}{c} i\sigma_0 d(-y_0,\vec{y}) \\ -i\sigma_0 u(-y_0,\vec{y}) \end{array}\right). & (4.86)\end{aligned}$$

To project back to the one-component basis, one takes the trace with $\left(\Gamma^\dagger_\eta, B^\dagger_\eta\right)$. This involves evaluating the following expression

$$\mathrm{Tr}\left(\Gamma^\dagger_\eta\sigma_0 B_{\eta'} - B^\dagger_\eta\sigma_0\Gamma_{\eta'}\right). \tag{4.87}$$

The result is nonzero only when $\eta_0 = \eta'_0 \pm 1$ and $\eta_i = \eta'_i,\ i = 1,2$. Here the "+" corresponds to $\eta_0 = 0$ and the "$-$" corresponds to $\eta_0 = 1$. This gives

$$\begin{aligned} \mathrm{Tr}\left(\Gamma^\dagger_\eta\sigma_0 B_{\eta'} - B^\dagger_\eta\sigma_0\Gamma_{\eta'}\right) &= 2(-)^{\eta_0+\eta_1+\eta_2}\,\mathrm{Tr}\left(\sigma_2^{\eta_2}\sigma_1^{\eta_1}\sigma_1^{\eta'_1}\sigma_2^{\eta'_2}\right), \\ &= 4(-)^{\eta_0+\eta_1+\eta_2}. & (4.88)\end{aligned}$$

One thus obtains the following tranformation on the one-component spinor

$$\chi_\eta(y_0,\vec{y}) \rightarrow i(-)^{\eta_0+\eta_1+\eta_2}\chi_{\tilde{\eta}}(-y_0,\vec{y}), \tag{4.89}$$

where $\tilde{\eta} = (\eta_0 \pm 1, \eta_1, \eta_2)$. This time-reversal operation is intuitive in that it changes η_0 while keeping η_1 and η_2 fixed.

Parity in two spatial directions reverses only one of the spatial coordinates, as reversing both would be equivalent to a rotation by π in the $x-y$ plane. In the continuum, parity operates on the fermion fields as follows

$$\begin{aligned} \Psi(x,y,t) &\rightarrow i\tilde{\gamma}_4\gamma_1\Psi(-x,y,t), & (4.90)\\ \bar{\Psi}(x,y,t) &\rightarrow \bar{\Psi}(-x,y,t)i\tilde{\gamma}_4\gamma_1. & (4.91)\end{aligned}$$

One can verify that this transformation also leaves (2.1) invariant as $[\tilde{\gamma}_4\gamma_1,\gamma_2] = [\tilde{\gamma}_4\gamma_1,\gamma_0] = 0$. With respect to the original honeycomb lattice of graphene, this is related to the symmetry between the A and B sublattices. As shown above for time-reversal, this induces a transformation on the staggered fermion fields in the spin-taste basis

$$\begin{aligned}
\Psi(y_0, y_1, y_2) &\rightarrow i\tilde{\gamma}_4\gamma_1\Psi(y_0, -y_1, y_2), && (4.92)\\
&= \begin{pmatrix} 0 & -i\sigma_1 \\ i\sigma_1 & 0 \end{pmatrix}\begin{pmatrix} u(y_0, -y_1, y_2) \\ d(y_0, -y_1, y_2) \end{pmatrix}, \\
&= \begin{pmatrix} -i\sigma_1 d(y_0, -y_1, y_2) \\ i\sigma_1 u(y_0, -y_1, y_2) \end{pmatrix}. && (4.93)
\end{aligned}$$

One follows the same procedure to project back to the one-component basis

$$\mathrm{Tr}\left(B_\eta^\dagger\sigma_1\Gamma_{\eta'} - \Gamma_\eta^\dagger\sigma_0 B_{\eta'}\right). \tag{4.94}$$

The result is nonzero only when $\eta_1 = \eta_1' \pm 1$ and $\eta_i = \eta_i',\ i = 0, 2$. Here the "+" corresponds to $\eta_1 = 0$ and the "$-$" corresponds to $\eta_1 = 1$. This gives

$$\mathrm{Tr}\left(B_\eta^\dagger\sigma_1\Gamma_{\eta'} - \Gamma_\eta^\dagger\sigma_1 B_{\eta'}\right) = 4(-)^{\eta_1}$$

One thus obtains the following tranformation on the one-component spinor

$$\chi_\eta(y_0, -y_1, y_2) \rightarrow (-)^{\eta_1}\chi_{\tilde{\eta}}(y_0, -y_1, y_2), \tag{4.95}$$

where $\tilde{\eta} = (\eta_0, \eta_1 \pm 1, \eta_2)$. It is known that a two-component massive spinor violates parity in $(2+1)$ dimensions [66], but the mass term in the lattice action (4.75) is invariant with respect to this transformation due to the fact that it has four components.

4.3.1 Improved Lattice Action

Based on the discussion above, one sees that staggered fermions are cheap to simulate (one-component in spin space, see (4.49)) and contain a remnant of chiral symmetry. However, particularly in LQCD simulations, the violation of taste symmetry at finite lattice spacing is troubling. For example, even on a fine lattice (0.05 fm), the splitting of the masses of the pion taste-multiplet is $O(100\text{ MeV})$, which is close to the physical pion mass [67]. It was realized that taste violations occur due to the exchange of gluons with momentum components that were on the order of the cutoff, π/a [68]. Thus, suppresssing the coupling of the fermions to these modes should reduce taste violations [69].

Couplings to the high-momentum gauge fields are eliminated by a process of link "fattening". This entails replacing the link, $U_\mu(n)$, used in parallel transport, with an appropriately weighted sum of paths connecting the sites n and $n+\hat{\mu}$. The simplest of these paths is the three-link staple which is given by

$$U_\mu^{f3}(n) = a^2 \sum_{\nu\neq\mu} \Delta_\nu^l U_\mu(n), \tag{4.96}$$

where the fattening is performed by a Laplacian operator that acts on the link in the following way:

$$\Delta_\nu^l U_\mu(n) = \frac{1}{a^2}\left[U_\nu(n)U_\mu(n+\hat{\nu})U_\nu^\dagger(n+\hat{\mu}) + U_\nu^\dagger(n-\hat{\nu})U_\mu(n-\hat{\nu})U_\nu(n-\hat{\nu}+\hat{\mu})\right]. \tag{4.97}$$

By expanding the link variable in terms of the gauge potential A_μ, one can see that in momentum space the fattening results in

$$A_\mu(p) \to \sum_{\nu\neq\mu}\left(2A_\mu(p)\left[\cos(\hat{p}_\nu)-1\right] + 4\sin(\hat{p}_\mu/2)\sin(\hat{p}_\nu/2)A_\mu(p)\right). \tag{4.98}$$

One can see that by making the replacement $U_\mu(n) \to c_1 U_\mu(n) + c_3 U_\mu^{f3}(n)$, with an appropriate choice of the coefficients c_1 and c_3, the coupling to photons with one momentum component, $\hat{p}_\nu = \pi$ (one only needs to consider transverse components), can be eliminated. This program can be extended to include a five-link staple, a seven-link staple, and an additional five-link staple, known as the Lepage term, which corrects for the low-momentum, $O(a^2)$ discretization errors introduced by the staples [70]. These terms are depicted in Fig. 4.1. For complete $O(a^2)$ improvement, one must also improve the free staggered fermion dispersion relation. This is done with the introduction of the so-called Naik term [71], which is given by a third-nearest-neighbor coupling

$$\begin{aligned}\partial_\mu\chi(n) \quad \to \quad & \tilde{c}_1\partial_\mu^{(f)}\chi(n) + c_N\frac{1}{a}[U_\mu(n)U_\mu(n+\hat{\mu})U_\mu(n+2\hat{\mu})\chi(n+3\hat{\mu}) \\ & -U_\mu^\dagger(n-\hat{\mu})U_\mu^\dagger(n-2\hat{\mu})U_\mu^\dagger(n-3\hat{\mu})\chi(n-3\hat{\mu})],\end{aligned} \tag{4.99}$$

where $\partial_\mu^{(f)}\chi(n) \equiv \frac{1}{2a}\left(U_\mu^{(f)}(n)\chi(n+\hat{\mu}) - U_\mu^{(f)\dagger}(n-\hat{\mu})\chi(n-\hat{\mu})\right)$ is the nearest-neighbor term written in terms of the fat link $U_\mu^{(f)}(n)$, which is a a weighted sum of the above-mentioned staples. Finally, one has an action that is free of $O(a^2)$ discretization errors. The choice of the coefficients is determined by a system of equations which fixes the coupling to the zero-momentum photons to one, the coupling to the high-momentum photons to zero, and takes into account the introduction of the Lepage term as well as an appropriate choice of $\tilde{c}_1$ and c_N to get the desired improvement of the free fermion dispersion relation. Noting that the gauge group does not enter in the choice of the coefficients and that the gauge field in the graphene EFT lives in $(3+1)$-dimensions, the set of coefficients chosen for LQCD can be carried over to the graphene EFT.

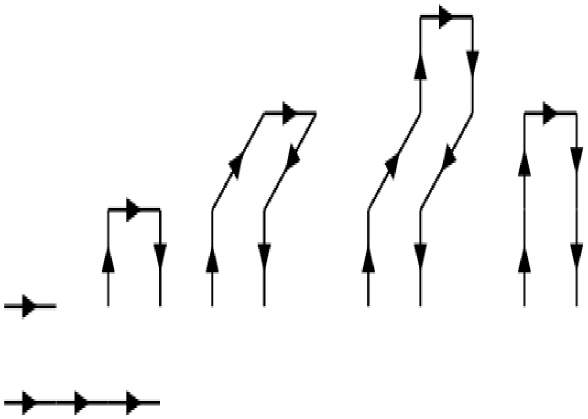

Figure 4.1. A pictorial representation of the links composing the asqtad improved staggered Dirac operator. The first row shows the "fat" links connecting site n with site $n+\hat{\mu}$ (from left): single link, three-link staple, five-link staple, seven-link staple, and Lepage term. The second row depicts the Naik term, which connects site n with site $n+3\hat{\mu}$.

Another way one can improve the staggered fermion action is to introduce the so-called tadpole improvement [72]. This program is based on the observation that in lattice perturbation theory, there are new vertices, not present in continuum perturbation theory, which are suppressed by powers of the lattice spacing. This can be seen by expanding the link variable

$$U_\mu(n) = 1 + iagA_\mu(n) - a^2g^2A_\mu(n)^2/2 + \dots \tag{4.100}$$

These new lattice vertices, however, lead to UV divergent diagrams whose divergences are cancelled by the lattice spacing dependence of the vertex. The result is that this class of diagrams are not as small as one would hope as they contain factors of only the coupling and not the lattice spacing. In the graphene EFT, one defines the tadpole factor, u_0, in the following way

$$u_0 = \left(\langle U^{(p)}\rangle\right)^{1/2}, \tag{4.101}$$

where $\langle U^{(p)}\rangle$ is the expectation value of the average of the space-time-oriented plaquette. Tadpole improvement, then, consists of dividing all links by the tadpole factor. Thus, each term in the $O(a^2)$-improved fermion faction receives a factor of $1/u_0^{L_t}$, where L_t is the length of the path in the temporal direction. This program has resulted in what is known as the improved asqtad action.

In continuum gauge field theory, it is necessary to fix the gauge in order to obtain the correct form for the gauge field propagator. This is done with the use of the Faddeev-Popov procedure [8]. On the lattice, however, there are finite degrees of freedom and thus gauge fixing is not necessary when sampling the path integral. However, when calculating charged propagators it is necessary to impose charge neutrality. This is done in the noncompact formulation by imposing the condition

$$\sum_{\vec{n}} \theta(n_0, \vec{n}) = 0, \tag{4.102}$$

which is the requirement that the average gauge potential on a time-slice be zero. The gauge condition (4.102) corresponds to a charged propagator moving in the background of a spatially uniform background charge of opposite sign. This gauge-fixing procedure will be necessary when one attempts to study the charged fermionic excitations of the system, which are sensitive to the spontaneous breaking of the $U(1)_\epsilon$ symmetry.

CHAPTER 5

MONTE CARLO METHODS

The numerical sampling of the Feynman path integral is a long standing and challenging problem in statistical physics and LQCD. Techniques and tools have been developed and refined to deal with this problem, and go under the name of Monte Carlo methods. In this chapter, the general principles and techniques are introduced, followed by the particulars of the algorithms used to obtain the results of this thesis.

5.1 Introduction to Monte Carlo

The Euclidean Feynman path integral has a strong connection with the partition function of a statistical system. This is clear from the expression for Z, as well as the calculation of observables given by the expression in (4.12). For the results in this thesis, in particular, one is interested in the evaluation of

$$\langle \mathcal{O} \rangle = \frac{\int \mathcal{D}\left[U_\mu\right] \mathcal{O} e^{-S_{eff}}}{\int \mathcal{D}\left[U_\mu\right] e^{-S_{eff}}}, \tag{5.1}$$

where $\mathcal{O}$ is a generic observable constructed from the fields appearing in the lattice action and the integration over the fermions has been performed, yielding

$$S_{eff} \equiv S_G - \mathrm{Tr}\, \log\left[\not{D} + m\right]. \tag{5.2}$$

Although one would like a way to evaluate these correlation functions, even the most modest volume would resist direct attempts at evaluation by today's most powerful supercomputers. The solution is importance sampling, whereby one samples the most important configurations determined by the weight, which is proportional to e^{-S_E}. By doing so in a manner that is faithful, one would hope that by generating a sequence of N_{conf} link configurations $\{U_\mu^{(i)}(n), i = 1, 2, \ldots, N_{conf}\}$, the observable could be estimated by a simple average

$$\langle \mathcal{O} \rangle \approx \frac{1}{N_{conf}} \sum_{i=1}^{N_{conf}} \mathcal{O}^{(i)}. \tag{5.3}$$

One needs a way to construct such a sequence of configurations following the probability distribution

$$P(U) = \frac{e^{-S[U]}\mathcal{D}[U]}{\int \mathcal{D}[U]e^{-S[U]}}. \tag{5.4}$$

The solution is a Markov process whereby one starts from a random configuration and constructs a stochastic sequence of configurations that converges to (5.4). Markov chains are characterized by a conditional transition probability

$$0 \leq W(U \to U') \leq 1, \tag{5.5}$$

$$\sum_{U'} W(U \to U') = 1, \tag{5.6}$$

where $W(U \to U')$ represents the probability of a transition from one gauge configuration $\{U_\mu(x)\}$, to another $\{U_\mu(x)'\}$. These probabilities have the Markov property in that they only depend on U and U' and not on their position in the sequence of generated configurations. One hopes that for well-chosen transition probabilities, the system reaches equilibrium. For this to happen, one needs the probability entering a state to be equal to the probability leaving that state

$$\sum_{U'} P(U')W(U' \to U) = \sum_{U'} P(U)W(U \to U'). \tag{5.7}$$

Typically, one demands that the conditional transition probabilities satisfy this relation term by term

$$P(U')P(U' \to U) = P(U)P(U \to U'). \tag{5.8}$$

This relation is known as detailed balance and is a sufficient condition for the Markov chain to converge to the desired equilibrium distribution. In practice, when equilibrating from a given initial gauge configuration, one determines if the distribution is close enough to the equilibrium distribution by monitoring certain observables and correlations in simulation time. In this thesis, the calculations monitor the Monte Carlo time histories of both the average value of the space-time-oriented plaquette, $\langle U_p \rangle$, as well as the chiral condensate, $\langle \bar{\psi}\psi \rangle$, in order to determine equilibrium as shown in Fig. 5.1 and Fig. 5.2. One must also demand that the Markov chain can access any configuration in a finite number of steps. This property is known as ergodicity and is an important consideration in the choice of algorithm for a lattice simulation

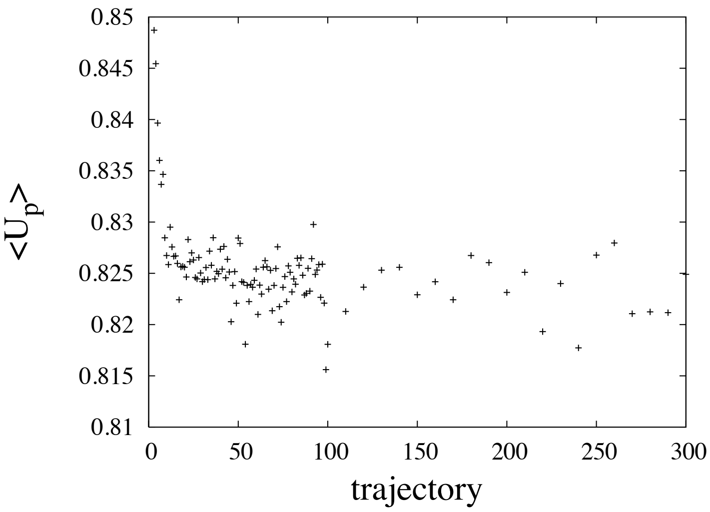

Figure 5.1. Time history of the space-time-oriented plaquette for lattice ensemble $8^2 \times 10 \times 120$, $\beta = 0.80$, $m = 0.05$, $\Phi_B = 0.125$. Starting from a "cold" lattice where all links are set to unity, one can see the value of the plaquette equilibrate at $O(200)$ trajectories. Note that the tadpole factor, u_0, has been determined self-consistently from the first 100 trajectories where the plaquette was measured after every trajectory.

It is convenient to express the transition probability $W(U \to U')$ as a product of the probability to propose a new configuration, $Q(U \to U')$, with the probability to accept that new configuration $A(U \to U')$

$$W(U \to U') = Q(U \to U')A(U \to U'). \tag{5.9}$$

Most algorithms demand that the function Q be symmetric, $Q(U \to U') = Q(U' \to U)$. This means that there is equal probability to propose U starting from U' as there is to propose U' starting from U. In terms of these quantities, detailed balance becomes

$$P(U')A(U' \to U) = P(U)A(U \to U'). \tag{5.10}$$

A popular and widely used algorithm makes the following choice for the acceptance probability [73]:

$$A(U \to U') = \min\left(1, e^{-\Delta S}\right), \quad \Delta S \equiv S[U'] - S[U]. \tag{5.11}$$

This is commonly known as a Metropolis step. One can easily verify that this satisfies detailed balance by direct substitution into (5.10). Although it is straightforward to implement the Metropolis approach for a gauge theory such as the one defined in (4.60) and

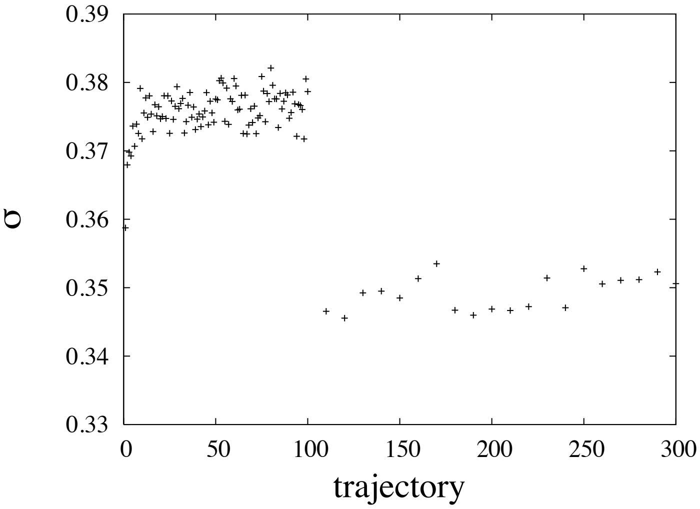

Figure 5.2. Time history of the chiral condensate, $\sigma \equiv \langle\bar{\psi}\psi\rangle$, for lattice ensemble $8^2 \times 10 \times 120$, $\beta = 0.80$, $m = 0.05$, $\Phi_B = 0.125$. One can also see the value of σ equilibrate at $O(200)$ trajectories. The condensate has been measured every trajectory during the first 100 trajectories and every 10 trajectories afterwards. The discontinuity in the Monte Carlo history that appears at a time of 100 is due to the introduction of the tadpole factor u_0 calculated from trajectories $60 - 100$.

(4.62), where a given link appears only in a small number of terms in the action, more sophisticated methods are needed to obtain high-quality results.

5.2 Hybrid Molecular Dynamics

Another solution in obtaining the desired Boltzmann distribution borrows ideas from classical mechanics. Namely, one introduces a fictitious momentum conjugate to the gauge field and integrates Hamilton's equations to obtain the desired distribution. This type of algorithm and its variants go under the name of molecular dynamics (MD) [74, 75]. One considers the Hamiltonian defined by

$$\mathcal{H}_{MD}(p, U) = \frac{1}{2}\sum_n p_n^2 + S_{eff}[U], \tag{5.12}$$

where S_{eff} is the action defined in (5.2) and p_n is a real momentum, living at site n, which is canonically conjugate to the $U(1)$ gauge link in the temporal direction, $U_0(n)$. The classical partition function corresponding to (5.12) takes the following form

$$Z_{MD} = \int \mathcal{D}[p]\mathcal{D}[U]e^{-\mathcal{H}_{MD}}, \tag{5.13}$$

where the integral over momenta is Gaussian, and thus adds a constant factor out in front of the original lattice partition function. With this in mind, (5.13) can be used to compute observables in the quantum theory. The trajectory that the gauge field and its momentum take in their evolution in "molecular dynamics time" is determined by the following equations of motion

$$\dot{\theta}(n) \equiv \frac{d\theta(n)}{d\tau} = p_n, \tag{5.14}$$

$$\dot{p}_n \equiv \frac{dp_n}{d\tau} = \frac{\partial S_{eff}}{\partial\theta(n)}, \tag{5.15}$$

where τ refers to MD time. One can see that the term on the right hand side of (5.15) resembles a "force", in analogy with classical mechanics. One can easily compute the derivative with respect to $\theta(n)$ of the gauge action in (4.60)

$$\frac{\partial S_G^{(NC)}}{\partial\theta(n)} = \beta\sum_i \Big(2\theta(n) - \theta(n+\hat{\imath}) - \theta(n-\hat{\imath})\Big)\,. \tag{5.16}$$

This is referred to as the "gauge force" for the noncompact $U(1)$ action. In order to obtain the “fermion force” coming from the determinant of the Dirac operator, one needs to use a fair amount of caution. This, along with the issue of how to properly integrate the equations of motion, will be the subject of the following section.

5.3 Φ-Algorithm for Graphene EFT

Formally, the path integral of the discretized graphene EFT can be written as

$$Z = \int \mathcal{D}[U]e^{-S_G}\det M(U), \tag{5.17}$$

where $M \equiv \not{D}_{st} + m$. The unimproved staggered Dirac operator can be written in position space as

$$(\not{D}_{st})_{x,y} = \frac{1}{2}\sum_\mu \eta_\mu(x)(U_\mu(x)\delta_{y,x+\hat{\mu}} - U_\mu^\dagger(x-\hat{\mu})\delta_{y,x-\hat{\mu}}). \tag{5.18}$$

Any discussion of how to perform calculations involving dynamical staggered fermions necessitates a discussion of the spectrum of the staggered Dirac operator. One takes note that all lattice Dirac operators have the property of "γ_5-hermiticity", which translates to

$$\not{D}^\dagger = \gamma_5\not{D}\gamma_5. \tag{5.19}$$

It can be shown that this property leads to all complex eigenvalues of the Dirac operator, λ_i, being paired

$$\not{D}\psi_i = \lambda_i\psi_i,\ \not{D}\left(\gamma_5\psi_i\right) = \lambda_i^*\left(\gamma_5\psi_i\right), \tag{5.20}$$

where both ψ_i and $\gamma_5\psi_i$ are eigenstates of the Dirac operator. It turns out that the staggered Dirac operator is antihermitian, which thus implies that all of its eigenvalues are purely imaginary. This property, coupled with γ_5-hermiticity leads to the following expression for the determinant in (5.17)

$$\det M(U) = m^{\nu} \prod_{\text{pairs}} \left(\lambda_i^2 + m^2\right), \tag{5.21}$$

where ν represents the number of zero modes and the product is over eigenvalue pairs. This expression demonstrates that the determinant is real and positive definite (for nonzero mass), thus allowing (5.2) to be interpreted as a probability distribution. The next step in dealing with the determinant is to note the following identity:

$$\det M(U) = \int \mathcal{D}[\Phi^\dagger, \Phi] e^{-\Phi^\dagger M^{-1}\Phi}, \tag{5.22}$$

where $\Phi^\dagger$, Φ are complex bosonic fields living at each lattice site and commonly referred to as "pseudofermion" fields. To reproduce the product of paired eigenvalues one first doubles the degrees of freedom by writing

$$Z = \int \mathcal{D}[U]\mathcal{D}[\Phi^\dagger, \Phi] e^{-\left(S_G + \Phi^\dagger (M^\dagger M)^{-1}\Phi\right)}, \tag{5.23}$$

where one uses the relation $\det(\not{D}^\dagger \not{D}) = [\det(\not{D})]^2$. Looking at the form of the staggered Dirac operator in (5.18), one takes note that it only couples even lattice sites to odd lattice sites and vice versa. This also holds true for the improved staggered Dirac operator in the asqtad action. This even-odd property can be exploited as $M^\dagger M$ decouples even and odd sites and thus one can obtain the correct expression for the determinant by restricting the pseudofermion fields to even or odd sites. One can readily generate a pseudofermion field with the correct distribution by first generating a random complex Gaussian field Ω, and acting on it with $M^\dagger$. The algorithm used to generate the results of this thesis uses a variant of the so-called Φ-algorithm [76]. In this approach, at the beginning of each MD trajectory, one generates a vector Φ and then proceeds to integrate the equations of motion for specified length, $\tau = N_s\epsilon$, where ϵ is the integration step size and N_s is the number of steps in the trajectory. The trajectory is typically taken to be unity and the step size is varied in order to achieve the desired acceptance ratio for the Metropolis step.

5.3.1 Fermion Force

One now needs to address the fermion force, which is computed using the term in the exponent of (5.23) involving the pseudofermion fields. One thus computes

$$\begin{aligned} F_n^{(F)} &= -\Phi^\dagger \frac{\partial}{\partial\theta(n)} \left(M^\dagger M\right)^{-1} \Phi, \\ &= \Phi^\dagger \left(M^\dagger M\right)^{-1} \frac{\partial\left(M^\dagger M\right)}{\partial\theta(n)} \left(M^\dagger M\right)^{-1} \Phi, \end{aligned} \tag{5.24}$$

where the computation of the fermion force involves the inversion of $M^\dagger M$, as opposed to M. This is a much easier task as $M^\dagger M$ is hermitian and positive definite. This allows one to employ iterative methods such as the conjugate gradient (CG) algorithm which is used in this thesis. Making the following definition:

$$P_{i,j} = X_i X_j^*, \; X \equiv \left(M^\dagger M\right)^{-1} \Phi, \tag{5.25}$$

where i, j label the lattice sites, one can write the force as

$$F_n^{(F)} = \mathrm{Tr}\left[U_0(n) M P \frac{\partial M^\dagger}{\partial U_0(n)} + U_0(n) P M^\dagger \frac{\partial M}{\partial U_0(n)} + \mathrm{c.c}\right], \tag{5.26}$$

where the trace operation is over spatial indices and one has traded derivatives with respect to the potentials for derivatives with respect to the $U(1)$-valued links $U_0(n)$ and their complex conjugates, $U_0^\dagger(n)$. This is convenient because the staggered Dirac operator is written in terms of the compact link variables as seen in (4.62). Computing the derivatives of the asqtad Dirac operator with respect to the links is a formidable task as $U_0(n)$ can appear in several places in both the fat- and long-link terms. To get an idea what one must do to compute the fermion force for improved staggered actions, one can start by examining the form it takes for the one-link unimproved staggered action. For this action the fermion force takes the form

$$F_n^{(F)} = -2U_0(n)\mathrm{Im}\left[\sum_\nu U_\nu(n+\hat{0}) P_{j+\hat{0}+\hat{\nu},j} - \sum_{\nu\neq\mu} U_\nu^\dagger(n+\hat{0}-\hat{\nu}) P_{j+\hat{0}-\hat{\nu},j}\right], \tag{5.27}$$

on even sites and

$$F_n^{(F)} = -2U_0(n)\mathrm{Im}\left[\sum_\nu U_\nu(n-\hat{\nu}) P_{j+\hat{0},j-\hat{\nu}} - \sum_{\nu\neq\mu} U_\nu^\dagger(n) P_{j+\hat{0},j+\hat{\nu}}\right], \tag{5.28}$$

on odd sites. In this expression, one has chosen Φ to reside only on even sites and the staggered phases, $\eta_\mu(n)$, have been absorbed into the links. Notice that the above expression contains links in the spatial directions. However, they do not have conjugate momenta associated with them as they are not dynamical. The terms for both even and odd sites represent propagation of the fermions coupled with parallel transport between source and sink to enforce gauge invariance. This can be seen by noting the identity

$$\langle P_{i,j}\rangle_{\Omega} = \left(M^{\dagger}M\right)^{-1}_{i,j}, \tag{5.29}$$

where the average is over the Gaussian distribution for the complex random vectors Ω. Improved actions will involve contributions to the fermion force from terms where $U_0(n)$ appears on the "sides" of a staple as well as from staples in the $\hat{0}$ direction. As one can imagine based on the discussion above, the fermion force constitutes a major part of any MD simulation involving dynamical fermions.

5.3.2 Integration Scheme

Integration of the first-order equations of motion is necessary to determine the trajectory in phase space, given a starting configuration $\{p_n^{(0)}, U_0^{(0)}(n)\}$. One of the main requirements one imposes on the chosen integration scheme is that it is invariant under a reversal of molecular dynamics time. This is a consequence of requiring that the transition function, $Q(U \to U')$, be symmetric in its arguments. The integration scheme used in this thesis is defined by the following equations

$$\begin{aligned} \theta^{(i-1/2)}(n) &= \theta^{(i-1)}(n) + \frac{\epsilon}{2}p_n^{(i-1)}, \\ p_n^{(i)} &= p_n^{(i-1)} + \epsilon F_n^{(i-1/2)}, \\ \theta^{(i)}(n) &= \theta^{(i-1/2)}(n) + \frac{\epsilon}{2}p_n^{(i-1)}, \end{aligned} \tag{5.30}$$

where superscript labels the MD time, $\tau_i = i\epsilon,\ i = 1, \ldots, N_s$, with ϵ the time step. Notice that (5.30) is written in terms of the potentials, which can then be exponentiated to determine the $U(1)$ links. This method is known as the leapfrog integration scheme and is known to have discretization errors $O(\epsilon^2)$.

In order to obtain accurate sampling of the path integral, one must either extrapolate observables to zero step size or correct for the discretization errors by introducing an accept/reject step at the end of each trajectory. The latter property, along with a refreshing of the momentum after each each trajectory, defines a class of algorithms known as hybrid Monte Carlo (HMC) [77, 78]. Returning to the decomposition of the conditional probabilities in (5.9), one identifies the MD trajectory with $Q(U \to U')$ and the acceptance probability, $A(U \to U')$, with that of the Metropolis algorithm.

CHAPTER 6

COMPUTATION OF OBSERVABLES

Once the gauge configurations have been produced using the methods discussed in the previous chapter, one then sets out computing observables of interest in the Euclidean field theory. The simplest such observable is the plaquette, U_P, which one must use to self-consistently determine the tadpole factor, u_0. Other observables of interest to this study consist of the fermionic condensates that develop when the graphene EFT is subject to an external magnetic field. Also, one can explore the excitations of the system, the Dirac quasiparticle as well as the pseudoscalar Goldstone mode, using standard techniques of lattice gauge theory spectroscopy. Finally, one must attempt to accurately estimate errors on the quantities computed.

6.1 Magnetic Field on a Torus

Although one would normally have translational invariance in the continuum graphene EFT, in the presence of a magnetic field, this is not so [79]. For a translationally invariant system, the operator $T_{\vec{R}} = e^{i\vec{R}\cdot\vec{p}}$, $\hbar = 1$, generates translations

$$T_{\vec{R}} f(\vec{r}) = f(\vec{r} + \vec{R}.) \tag{6.1}$$

This operator commutes with the Hamiltonian, which is invariant under translations

$$\begin{aligned} T_{\vec{R}}\mathcal{H}(\vec{r})\psi(\vec{r}) &= \mathcal{H}(\vec{r}+\vec{R})\psi(\vec{r}+\vec{R}), \\ &= \mathcal{H}(\vec{r})T_{\vec{R}}\psi(\vec{r}). \end{aligned} \tag{6.2}$$

The set of these translation operators forms a group which follows from the relations

$$T_{\vec{R}}T_{\vec{R}'} = T_{\vec{R}+\vec{R}'}, \tag{6.3}$$

$$T_{\vec{R}}T_{-\vec{R}} = \mathbf{1}. \tag{6.4}$$

However, one sees that with a vector potential of the form (3.2), one will no longer have translational invariance of the Hamiltonian as $\vec{A}(\vec{r}) \neq \vec{A}(\vec{r}+\vec{R})$. Since the magnetic field is uniform, the vector potential is linear in the coordinates and thus one can deduce that the vector potential changes in the following way under translation

$$\vec{A}(\vec{r}+\vec{R}) = \vec{A}(\vec{r}) + \vec{\nabla}\xi(\vec{r}). \tag{6.5}$$

One can confirm this relation by noting that $B\hat{z} = \vec{\nabla}_r \times \vec{A}(\vec{r}) = \vec{\nabla}_r \times \vec{A}(\vec{r}+\vec{R})$. For Landau gauge, one can verify that $\xi(\vec{r}) = ByR_x$, where R_x is the x-component of the translation vector $\vec{R}$. Using this, one can construct an operator that commutes with the Hamiltonian. It is known as the magnetic translation operator, and is a combination of a gauge transformation and the applicaiton of the usual translation operator defined above

$$\mathcal{T}_{\vec{R}} \equiv e^{ie\xi(\vec{r})} T_{\vec{R}}. \tag{6.6}$$

One can see that this operator commutes with the Hamiltonian in the presence of the vector potential (3.2) (or any other gauge-equivalent vector potential) by using the following relations

$$\begin{aligned} T_{\vec{R}}\mathcal{H}(\vec{p}+e\vec{A}(\vec{r})) &= \mathcal{H}(\vec{p}+e\vec{A}(\vec{r})+e\vec{\nabla}\xi(\vec{r}))T_{\vec{R}}, && (6.7)\\ \mathcal{H}(\vec{p}+e\vec{A}(\vec{r})+e\vec{\nabla}\xi(\vec{r})) &= e^{-ie\xi(\vec{r})}\mathcal{H}(\vec{p}+e\vec{A}(\vec{r}))e^{ie\xi(\vec{r})}. && (6.8) \end{aligned}$$

It is interesting to note that these operators do not commute

$$\begin{aligned} \mathcal{T}_{\vec{R}}\mathcal{T}_{\vec{R}'} &= e^{ieByR_x} T_{\vec{R}} e^{ieByR'_x} T_{\vec{R}'}, \\ &= e^{ieByR_x} e^{ieBR'_x(y+R_y)} T_{\vec{R}} T_{\vec{R}'}, \\ &= e^{ieBR'_xR_y} \mathcal{T}_{\vec{R}+\vec{R}'} && (6.9) \end{aligned}$$

This relation has interesting consequences for lattice calculations which are performed on a torus due to the periodic boundary conditions imposed on the $U(1)$ link variables. One imposes this periodicity with the magnetic translation operator

$$\begin{aligned} \mathcal{T}_{L_x\hat{x}}\psi(x,y) &= e^{ieBL_xy}\psi(x+L_x,y) = \psi(x,y), && (6.10)\\ \mathcal{T}_{L_y\hat{y}}\psi(x,y) &= e^{ieBL_xy}\psi(x,y+L_y) = \psi(x,y), && (6.11) \end{aligned}$$

where $\psi(x,y)$ is an eigenstate of the Hamiltonian in the presence of the magnetic field. From physical considerations, it is obvious that a wavefunction on the torus must satisfy the following relation:

$$\mathcal{T}_{L_x\hat{x}}\mathcal{T}_{L_y\hat{y}}\psi(x,y) = \mathcal{T}_{L_y\hat{y}}\mathcal{T}_{L_x\hat{x}}\psi(x,y). \tag{6.12}$$

Using this in conjuction with the relation in (6.9), one obtains

$$\mathcal{T}_{L_x\hat{x}}\mathcal{T}_{L_y\hat{y}} = e^{ieBL_xL_y}\mathcal{T}_{L_y\hat{y}}\mathcal{T}_{L_x\hat{x}}. \tag{6.13}$$

Thus, for toroidal boundary conditions, one is led to the quantization of the magnetic flux

$$eBL_xL_y = 2\pi N_B, \tag{6.14}$$

where N_B is an integer. This requirement is equivalent to imposing that the total flux through the xy-plane is an integral number of flux quanta. Furthermore, N_B enumerates the degeneracy of each Landau level on the torus [80]. In lattice calculations, one typically restricts N_B to the range [81]

$$0 \le N_B \le \frac{N_xN_y}{4}, \tag{6.15}$$

where N_x and N_y refer to the number of lattice sites in the x and y directions. The representation of (3.2) on the lattice in terms of the spatial links is given by

$$U_y(n) = e^{ia_s^2eBn_x}, \tag{6.16}$$

$$U_x(n) = \begin{cases} 1 & ,n_x \neq N_s-1 \\ e^{-ia_s^2eBN_xn_y} & ,n_x = N_s-1 \end{cases}. \tag{6.17}$$

One should note that these links are static, unlike the dynamical time-like links. Here static refers to the fact that they are not changed during the Monte Carlo updating process.

6.2 Condensates

As discussed in previous chapters, the characterization of the ground state of the graphene EFT in the presence of an external magnetic field involves the calculation of fermionic condensates. On the lattice, these condensates can be estimated on each gauge configuration using random stochastic vectors.

We first discuss the meaning of the chiral condensate in terms of the degrees of freedom on the hexagonal lattice. The appearance of a nonzero value for the chiral condensate, $\langle\bar{\psi}\psi\rangle$, signals the appearance of a Dirac mass in the low-energy theory. This term has the form

$$\tilde{\Delta}_\sigma\bar{\psi}P_\sigma\psi = \tilde{\Delta}\psi^\dagger\gamma_0P_\sigma\psi, \tag{6.18}$$

which is a triplet with respect to $SU(2)_\sigma$ which breaks down to $U(1)_\sigma$ with the generator $\tilde{\gamma}_{4,5} \otimes P_\sigma$. Notice that the mass above contains an extra spin label. In general, the order parameters of the graphene EFT can depend on the spin projection. For staggered fermions, this spin label corresponds to taste. In this thesis, all of the condensates measured are taste singlets and thus do not allow an investigation of the spin degree of freedom in the graphene EFT. Written in terms of Bloch components, the operator in (6.18) can be expressed as

$$\tilde{\Delta}_\sigma : \quad \psi^\dagger_{KA\sigma}\psi_{KA\sigma} - \psi^\dagger_{KB\sigma}\psi_{KB\sigma} + \psi^\dagger_{K'A\sigma}\psi_{K'A\sigma} - \psi^\dagger_{K'B\sigma}\psi_{K'B\sigma}. \tag{6.19}$$

One can interpret a nonzero value for this order parameter as an imbalance of charge between the A and B sublattices, which corresponds to a charge density wave (CDW).

To calculate the condensate $\langle\bar{\psi}\psi\rangle$ on the lattice, one first translates this expression to staggered fermion language. It is not difficult to see that in the spin-taste basis it corresponds to the operator $\bar{\Psi}(y)(\mathbf{1}\otimes\mathbf{1})\Psi(y)$, and in one-component form, using (4.63) and (4.64), one can verify that this becomes $\sum_\eta \bar{\chi}_\eta(y)\chi_\eta(y)$ in one-component form. Next one employs the identity

$$\begin{aligned} \langle\bar{\chi}\chi\rangle &= \frac{\partial \log Z}{\partial m} = \frac{1}{Z}\int \mathcal{D}U_\mu \,\mathrm{Tr}\left[(\not{D}_{st}+m)^{-1}\right] e^{-S_{eff}[U]}, & (6.20)\\ &= \langle \mathrm{Tr}\left[(\not{D}_{st}+m)^{-1}\right]\rangle. & (6.21) \end{aligned}$$

where Z is the lattice-staggered partition function and we have introduced the staggered Dirac operator

$$\begin{aligned} (\not{D}_{st})_{x,y} &= \sum_\mu (U^{(F)}_\mu(x)\delta_{y,x+\hat{\mu}} + U^{(L)}_\mu(x)\delta_{y,x+3\hat{\mu}} \\ &- U^{(F)\dagger}_\mu(x-\hat{\mu})\delta_{y,x-\hat{\mu}} - U^{(L)\dagger}_\mu(x-3\hat{\mu})\delta_{y,x-3\hat{\mu}}), \end{aligned} \tag{6.22}$$

where $U^{(F)}_\mu(x)$ refers to the fat links and $U^{(L)}_\mu(x)$ refers to the long links. In the above expression, the staggered phases $\eta_\mu(x)$ have been absorbed into the links. The trace in (6.22) involves calculating the fermion propagator from a given lattice site back to the same site and repeating this for every site on the lattice. Needless to say, for even very modest volumes, a direct estimation of the condensate on a lattice ensemble is impractical. The solution to this problem is to estimate the condensate stochastically. Namely, one introduces complex, Gaussian-distributed numbers χ_i, which satisfy

$$\langle \chi_i \chi_j^* \rangle_\chi = \delta_{ij}, \tag{6.23}$$

where i and j refer to lattice sites and the average is performed with the Gaussian distribution of the χ's. The trace now can be evaluated as follows

$$\mathrm{Tr}\left[(\not{D}_{st}+m)^{-1}\right] = \sum_{i,j}(\not{D}_{st}+m)^{-1}\delta_{ij} \approx \frac{1}{N_v}\sum_{k=1}^{N_v}\chi^{(k)\dagger}(\not{D}_{st}+m)^{-1}\chi^{(k)}, \tag{6.24}$$

where one has replaced the integration over the Gaussian distribution with an average over N_v random vectors drawn from the distribution. In this thesis, $O(100)$ stochastic vectors are used to give an accurate estimation of the chiral condensate. The behavior of the ensemble average of the condensate as a function of the number of stochastic vectors is shown in Fig. 6.1. The stochastic estimate on a given gauge configuration has a variance associated with it. The behavior of the standard deviation of the stochastic estimate of the chiral condensate on a single configuration is plotted versus the number of stochastic vectors in Fig. 6.2. The behavior of the variance as a function of the number of stochastic vectors can be described by the following expression

$$\sigma^2_{N_v} = \frac{\sigma_1^2}{N_v} + \sigma_g^2, \tag{6.25}$$

where σ_1^2 is the variance associated with a stochastic estimate that uses a single random vector and σ_g^2 is the variance associated with the gauge fluctuations.

Another condensate which characterizes graphene in the presence of an external magnetic field is a time-reversal odd condensate which in the low-energy energy theory corresponds to the Haldane mass term. This mass term has the following form:

$$\Delta_\sigma \bar{\Psi}\tilde{\gamma}_{4,5} P_\sigma \Psi = \Delta_\sigma \Psi^\dagger \gamma_0 \tilde{\gamma}_{4,5} P_\sigma \Psi, \tag{6.26}$$

which is a singlet with respect to $SU(2)_\sigma$ but is odd under time-reversal. In terms of Bloch components, it is given by

$$\Delta_\sigma: \quad \psi^\dagger_{KA\sigma}\psi_{KA\sigma} - \psi^\dagger_{K'A\sigma}\psi_{K'A\sigma} - \psi^\dagger_{KB\sigma}\psi_{KB\sigma} + \psi^\dagger_{K'B\sigma}\psi_{K'B\sigma}.$$

Thus, this order parameter can be seen to represent a charge imbalance between the two valleys, K and K'. To discuss the calculation of the Haldane condensate, one first considers the following staggered operator

$$\bar{\Psi}(y)\left(\tilde{\gamma}_{4,5} \otimes \mathbf{1}\right)\Psi(y) = \bar{u}(y)\left(\mathbf{1} \otimes \mathbf{1}\right)u(y) - \bar{d}(y)\left(\mathbf{1} \otimes \mathbf{1}\right)d(y), \tag{6.27}$$

where the four-dimensional Dirac spinor space is tensored with the two-dimensional taste space. Using the transformations (4.63) and (4.64), one can obtain the one-component form

$$\bar{u}(y)\left(\mathbf{1} \otimes \mathbf{1}\right)u(y) = \bar{u}^{\alpha a}(y)u^{\alpha a}(y) = \left(\frac{1}{4\sqrt{2}}\right)^2 \sum_{\eta,\eta'} \bar{\chi}_\eta(y)\chi_{\eta'}(y)\,\mathrm{Tr}\left[\Gamma^\dagger_\eta \Gamma_{\eta'}\right]. \tag{6.28}$$

The second term on the right side of (6.27) can be written in way similar to (6.28)

$$\bar{d}(y)\left(\mathbf{1} \otimes \mathbf{1}\right)d(y) = \left(\frac{1}{4\sqrt{2}}\right)^2 \sum_{\eta,\eta'} \bar{\chi}_\eta(y)\chi_{\eta'}(y)\,\mathrm{Tr}\left[B^\dagger_\eta B_{\eta'}\right]. \tag{6.29}$$

Taking the difference of (6.28) and (6.29) and employing the identity

$$\mathrm{Tr}\left[\Gamma^\dagger_\eta \Gamma_{\eta'} - B^\dagger_\eta B_{\eta'}\right] = \begin{cases} 4i, & \eta_\mu \neq \eta'_\mu, \forall\mu \\ 0, & \text{otherwise} \end{cases}, \tag{6.30}$$

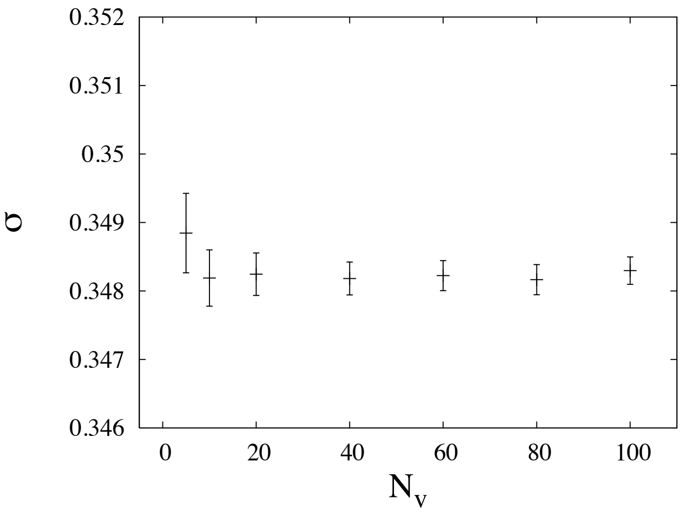

Figure 6.1. Value of the condensate, $\sigma \equiv \langle\bar{\psi}\bar{\psi}\rangle$, as a function of the number of stochastic vectors, N_v, for lattice ensemble $8^2 \times 10 \times 120, \beta = 0.80, m = 0.05, \Phi_B = 0.125$ with 189 gauge configurations.

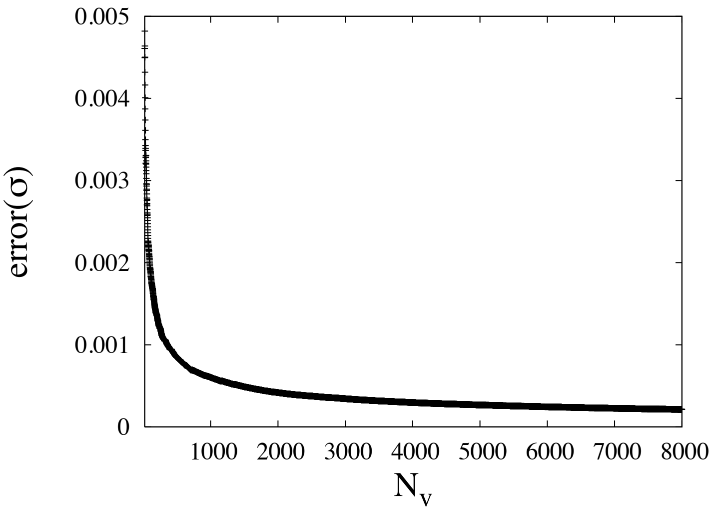

Figure 6.2. Error in the mean for the stochastic estimation of the chiral condensate on a single gauge configuration as a function of the number of stochastic vectors, N_v, for lattice ensemble $8^2 \times 10 \times 120, \beta = 0.80, m = 0.05, \Phi_B = 0.125$.

one can write the operator in (6.27) in the following form

$$\bar{\Psi}(y)\left(\tilde{\gamma}_{4,5}\otimes\mathbf{1}\right)\Psi(y)=\frac{i}{8}\sum_{\eta_\mu\neq\eta'_\mu}\bar{\chi}_\eta(y)\chi_{\eta'}(y). \tag{6.31}$$

One then takes the average of this operator over the entire lattice. A calculation of this term would involve a procedure similar to that used to calculate $\langle\bar{\chi}\chi\rangle$. A qualitative difference, however, can be seen by inspecting the expression on the right-hand side of (6.31), where one sees that this quantity involves the propagation of a fermion from each site within the cube to its opposite corner. To evaluate this quantity stochastically, one first generates an ensemble of Gaussian distributed complex victors satisfying (6.23) with support only on sites with a given $\eta=(\eta_t,\eta_x,\eta_y)$, where η_μ labels a particular site within the cube. The source is then shifted to the opposite corner of the cube using parallel transport:

$$\tilde{\Phi}^{(k)}=\frac{1}{6}\sum_P\hat{S}_{P_\mu}\hat{S}_{P_\nu}\hat{S}_{P_\lambda}\Phi^{(k)} \tag{6.32}$$

where the sum is over the six permutations of paths that take the vector to the corner opposite η. Here P_μ, P_ν, P_λ are permutations of $\pm t, \pm x, \pm y$ and the shift operators have been introduced

$$\left(\hat{S}_{\pm\mu}\Phi\right)_i \;=\; \begin{cases} U^\dagger_\mu(x-\hat{\mu})\Phi_{i-\hat{\mu}} & ,- \\ U_\mu(x)\Phi_{i+\hat{\mu}} & ,+ \end{cases}. \tag{6.33}$$

Using the source in (6.32), one can calculate the Haldane condensate as follows:

$$\sum_{y;\eta_\mu\neq\eta'_\mu}\bar{\chi}_\eta(y)\chi_{\eta'}(y)\approx\frac{1}{N_v}\sum_{k=1}^{N_v}\Phi^{(k)\dagger}M^{-1}\tilde{\Phi}^{(k)}. \tag{6.34}$$

where the sum over η goes over all eight sites of the cube. Stochastic estimation relies on cancellations of the noise to find the signal, which decays exponentially with the separation between source and sink. Therefore, for operators such as the Haldane condenstate, which are nonlocal, it can be difficult to obtain a good signal to noise ratio. In order to overcome this, the results in this thesis have been calculated using $N_v\approx 1000$ in (6.34). In Fig. 6.3 the error in the stochastic estimation is shown versus the number of stochastic vectors used. One needs a large amount of random vectors in order to obtain a signal. This is evident when looking at the time history for the real part of the Haldane condensate for an ensemble in Fig. 6.4.

6.3 Spectroscopy

The computation of the spectrum of a Euclidean field theory is one of the areas where lattice methods excel. For LQCD, an extensive amount of work has been done calculating

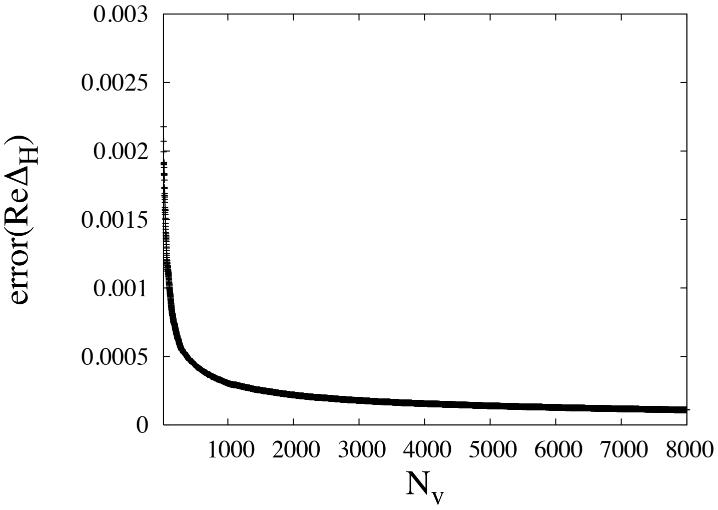

Figure 6.3. Error in the mean for the stochastic estimation of the real part of the Haldane condensate on a single gauge configuration as a function of the number of stochastic vectors, N_v, for lattice ensemble $8^2 \times 10 \times 120, \beta = 0.80, m = 0.05, \Phi_B = 0.125$.

the masses of the hadrons and their excited states. In this section, the construction of operators with the correct quantum numbers, such as spin and parity, is discussed. Subsequently, the numerical calculation of the propagators is touched upon, followed by a discussion of how one extracts a mass from the correlators.

6.3.1 Fermion Propagator

The spontaneous breaking of the $U(1)_\epsilon$ symmetry due to magnetic catalysis has consequences for the Dirac quasiparticles in graphene. Namely, one expects these excitations to be gapped in the broken phase. It is for this reason that one would like to study the fermion propagator defined as

$$G_F(x,y) \equiv \langle \chi(x)\bar{\chi}(y)\rangle = \frac{1}{Z}\int \mathcal{D}[U_\mu]\,(\not{D}_{st}+m)^{-1}_{x,y}\,e^{-S_{eff}}. \tag{6.35}$$

From the expression above, one sees that the calculation involves the inversion of the Dirac operator on each gauge configuration. In a lattice calculation, one does not direclty obtain the matrix $M^{-1} \equiv (\not{D}_{st}+m)^{-1}$, but uses the concept of a source to cast the problem into a linear system of equations of the form $Ax = b$. In this way, one is able to use iterative techniques which are much more efficient [82]. The equation to be solved is

$$M_{x,y}G_y = S_x, \tag{6.36}$$

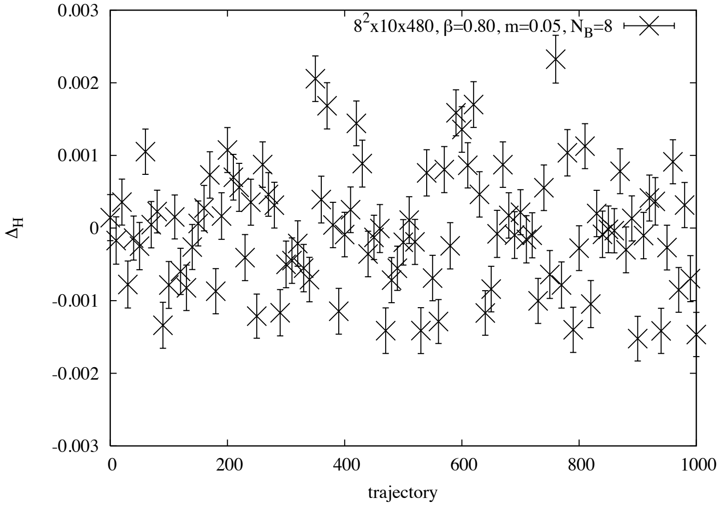

Figure 6.4. Monte Carlo time series for the real part of the Haldane condensate for lattice ensemble $8^2 \times 10 \times 480, \beta = 0.80, m = 0.05, \Phi_B = 0.125$ using 101 configurations.

where G is a row of the propagator and S is the source vector. For the purpose of this thesis, it is typically sufficient to use what is known as a point source

$$S_x^{(x_0)} \equiv \delta_{x_0 x}, \tag{6.37}$$

where x_0 is the location of the source. The solution of (6.36) gives the vector G which describes the propagation of a fermion from site x_0, where the source is located, to all other sites. Other types of sources exist which attempt to optimize the overlap of a given operator with the physical state described by the same quantum numbers [83].

One typically is interested in a propagator with a definite spatial momentum. On the lattice the spatial momenta are given by

$$\vec{p} \equiv \frac{2\pi}{L_s}(n_x, n_y), \;\; n_x, n_y \in \mathbb{Z}, \tag{6.38}$$

where L_s is the lattice extent in the spatial direction. These discrete momenta are dictated by the periodic boundary conditions for bosonic and fermionic quantities in the spatial direction. The quasiparticle propagator in the time-like direction with a definite momentum $\vec{p}$ is given by

$$G_F^{(t)}(\vec{p}, \tau) = \frac{1}{\sqrt{V_s}} \sum_{\vec{r}} e^{-i a_s \vec{r}\cdot\vec{p}} G_F(\vec{r}, \tau), \tag{6.39}$$

where V_s represents the spatial lattice volume and $\vec{r}$ represents the spatial coordinates of the lattice site. One can also do the same for a particular spatial direction:

$$G_F^{(x)}(x, p_y, \omega_l) = \frac{1}{\sqrt{N_s N_\tau}} \sum_{y,t} e^{-ia_s y p_y + ia_t t \omega_l} G_F(\vec{r}, \tau), \tag{6.40}$$

where $\omega_l = (2l+1)\pi/N_\tau$ is a fermionic Matsubara frequency. From the behavior of (6.39) and (6.40) as a function of the temporal and spatial separations, respectively, one can extract the energy levels of the fermion. The form of the free staggered fermion propagator gives a clue how to do so

$$G_F^{(t)}(\vec{p}, \tau) = \begin{cases} \cosh\left(E_t\left(\tau - N_\tau/2\right)\right)\left[\cosh\left(E_t N_\tau/2\right)\cosh\left(E_t\right)\right]^{-1}, \tau \text{ odd} \\ -2m\sinh\left(E_t\left(\tau - N_\tau/2\right)\right)\left[\cosh\left(E_t N_\tau/2\right)\sinh\left(2E_t\right)\right]^{-1}, \tau \text{ even} \end{cases} \tag{6.41}$$

$$G_F^{(x)}(x, p_y, \omega_l) = \begin{cases} \sinh\left(E_s\left(\tau - N_s/2\right)\right)\left[\sinh\left(E_s N_s/2\right)\cosh\left(E_s\right)\right]^{-1}, x \text{ odd} \\ -2m\sinh\left(E_s\left(x - N_s/2\right)\right)\left[\sinh\left(E_s N_s/2\right)\sinh\left(2E_s\right)\right]^{-1}, x \text{ even} \end{cases} \tag{6.42}$$

where

$$E_{t,s} = \sinh^{-1}(\omega_{t,s}) = \log\left(\omega_{t,s} + \sqrt{\omega_{t,s}^2 + 1}\right), \tag{6.43}$$

$$\omega_t^2 = \sum_{k=1,2} \sin^2(p_k) + m^2,\ \omega_s^2 = \sin^2(\omega_l) + \sin^2(p_y) + m^2. \tag{6.44}$$

One can use the form in expressions (6.41) and (6.42) to deduce a fit form for the Monte Carlo data. An example which illustrates the behavior of the temporal propagator is given in Fig. 6.5. In this thesis, correlators at zero spatial momentum are of interest and can be represented by

$$\begin{aligned} G_F^{(t)}(\tau, \vec{p} = \mathbf{0}) &= \frac{A_t}{2}\left(1 + (-)^\tau\right)\left(e^{-m_F\tau} + e^{-m_F(N_\tau - \tau)}\right) \\ &+ \frac{A_t}{2}\left(1 - (-)^\tau\right)\left(e^{-m_F\tau} - e^{-m_F(N_\tau - \tau)}\right), \end{aligned} \tag{6.45}$$

for the temporal propagator and

$$\begin{aligned} G_F^{(x)}(x, p_y = 0, \omega_0) &= \frac{A_{e,s}}{2}\left(1 + (-)^x\right)\left(e^{-m_F^{(s)}x} + e^{-m_F^{(s)}(N_s - x)}\right) \\ &+ \frac{A_{o,s}}{2}\left(1 - (-)^x\right)\left(e^{-m_F^{(s)}x} - e^{-m_F^{(s)}(N_s - x)}\right), \end{aligned} \tag{6.46}$$

for the spatial propagator, where $\omega_0 = \pi/N_\tau$ represents the lowest fermionic Matsubara frequency. In the above expressions the masses m_F and $\tilde{m}_F$ have been introduced which represent the mass of the fermion in Coulomb gauge (assuming the gauge fixing procedure introduced earlier) and the screening mass, respectively. The screening mass proves useful in determining the effects of a finite spatial volume on the calculations performed in the graphene EFT on the lattice.

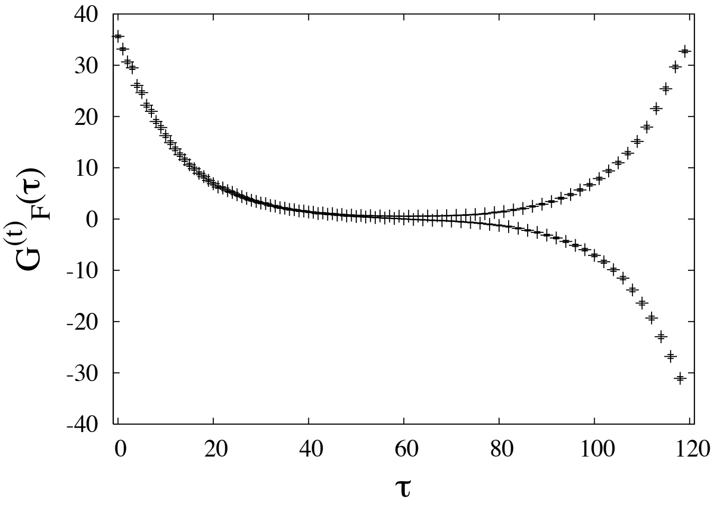

Figure 6.5. Zero-momentum Dirac quasiparticle propagator in the temporal direction for lattice ensemble $8^2 \times 10 \times 120, \beta = 0.80, m = 0.05, \Phi_B = 0.125$ with 800 gauge configurations. One can see the propagator's periodic behavior for odd τ and antiperiodic behavior for even τ.

6.3.2 Pseudoscalar Goldstone Mode

As was mentioned in previous sections, the appearance of a nonzero chiral condensate, $\langle\bar{\psi}\psi\rangle \neq 0$, signals the spontaneous breaking of the staggered $U(1)_\epsilon$ symmetry and thus, the appearance of a pseudoscalar Goldstone mode. This state is similar to the almost massless pion that appears in QCD due to the spontaneous breaking of chiral symmetry. Using this analogy, one can think of the Goldstone mode in the graphene EFT as a pseudoscalar fermion-antifermion bound state. The construction of meson operators in LQCD, which represent bound states of quarks and antiquarks, involes determining the fermion bilinear with the appropriate quantum numbers. For staggered fermions in particular, this is a much more difficult task than for, say, Wilson fermions, due to the fact that spin-taste basis fields involve a linear combination of the one-component fields at the corners of the cube. Furthermore, for the graphene EFT, the fact that the fermions live in $(2 + 1)$ dimensions makes the task even more difficult.

One can start with a general bilinear in the spin-taste basis

$$\mathcal{O}_{S,T} = \bar{\Psi}(y)\,(\Gamma_S \otimes \Gamma_T^*)\,\Psi(y), \tag{6.47}$$

where Γ_S and Γ_T are gamma matrices acting on the Dirac and taste indices respectively. In $(3 + 1)$ dimensions, choosing $\Gamma_S = \Gamma_T$ gives local operators in the one-component basis.

For the Goldstone mode in $(2+1)$ dimensions, it turns out that the relevant operator is given by

$$\bar{\Psi}(y)\left(\tilde{\gamma}_4 \otimes \mathbf{1}\right)\Psi(y) = \bar{u}(y)d(y) + \bar{d}(y)u(y) = \frac{1}{8}\sum_{\eta}\epsilon(\eta)\bar{\chi}_\eta(y)\chi_\eta(y), \tag{6.48}$$

where $\epsilon(x) \equiv (-)^{x_0+x_1+x_2}$, and the following identity was used

$$\mathrm{Tr}\left(\Gamma_\eta^\dagger B_{\eta'} + B_\eta^\dagger \Gamma_{\eta'}\right) = 4\epsilon(\eta)\delta_{\eta,\eta'}. \tag{6.49}$$

In Table 6.1, the commonly used staggered fermions in $(2+1)$ dimensions are listed along with their associated phase and alternating partner state, which will be discussed later. The zero-momentum temporal correlator for the bilinear in (6.48) is given by

$$\begin{aligned}
C_{PS}(\vec{p}=0;\tau) &= \sum_{\vec{y}}\langle \mathcal{O}_{PS}(\vec{y},\tau)\mathcal{O}_{PS}^\dagger(\vec{y},\tau)\rangle, \\
&= -\sum_{\vec{y}}\sum_{\eta,\eta'}(-)^{\eta-\eta'}G_F(\eta',2y+\eta)G_F(2y+\eta,\eta'), && (6.50)\\
&= -\sum_{\vec{y}}\sum_{\eta,\eta'}(-)^{\eta-\eta'}G_F^\dagger(2y+\eta,\eta')G_F(2y+\eta,\eta'), && (6.51)
\end{aligned}$$

where in the last step, path-reversal symmetry of the propagator has been applied, $G_F(x,x') = (-)^{x-x'}G_F^\dagger(x',x)$. Notice that the operator in (6.48) involves mulitiple time slices. Thus, the temporal separation of the correlator in (6.51) is ambiguous. In order to involve only a single timeslice, one introduces a new operator which is a linear combination of the original operator and an additional operator with a different spin and taste content. For the case of the pseudoscalar, consider the following operator:

$$\begin{aligned}
\bar{\Psi}(y)\left(\gamma_\mu\gamma_\nu \otimes \sigma_\mu^*\sigma_\nu^*\right)\Psi(y) &= \bar{u}(y)\left(\sigma_\mu\sigma_\nu \otimes \sigma_\mu^*\sigma_\nu^*\right)u(y) + \bar{d}(y)\left(\sigma_\mu\sigma_\nu \otimes \sigma_\mu^*\sigma_\nu^*\right)d(y), \\
&= \left(\frac{1}{4\sqrt{2}}\right)^2\sum_{\eta,\eta'}\bar{\chi}_\eta(y)\chi_{\eta'}(y)\,\mathrm{Tr}\left[\Gamma_\eta^\dagger\sigma_\mu\sigma_\nu\Gamma_{\eta'}\sigma_\nu\sigma_\mu\right] \\
&+ \left(\frac{1}{4\sqrt{2}}\right)^2\sum_{\eta,\eta'}\bar{\chi}_\eta(y)\chi_{\eta'}(y)\,\mathrm{Tr}\left[B_\eta^\dagger\sigma_\mu\sigma_\nu B_{\eta'}\sigma_\nu\sigma_\mu\right], \\
&= \frac{1}{8}\sum_\eta\epsilon(\eta)(-)^{\eta_0}\bar{\chi}_\eta(y)\chi_\eta(y), && (6.52)
\end{aligned}$$

where in the last line the following identity was used

$$\mathrm{Tr}\left[\Gamma_\eta^\dagger\sigma_\mu\sigma_\nu\Gamma_{\eta'}\sigma_\nu\sigma_\mu\right] + \mathrm{Tr}\left[B_\eta^\dagger\sigma_\mu\sigma_\nu B_{\eta'}\sigma_\nu\sigma_\mu\right] = 4\epsilon(\eta)(-)^{\eta_0}\delta_{\eta,\eta'},\ \ \mu,\nu \neq 0. \tag{6.53}$$

Adding (6.52) to (6.48), gives a new operator which only lives on sites of the cube with $\eta_0 = 0$, but excited two separate states. This is one of the prices that one must pay for using

Table 6.1. Listing of common staggered bilinear operators in $(2+1)$ dimensions. They are written in terms of their spin-taste representation as well as their one-component representation which is encoded in the phase factor. Single time-slice correlators imply an additional alternating state which is listed in the third column for each channel. Adapted from [1].

Staggered Fermion Bilinears in $(2+1)$ Dimensions

	Direct	Phase	Alternating
pseudoscalar	$\tilde{\gamma}_4 \otimes \mathbf{1}$	$(-)^{x_0+x_1+x_2}$	$\gamma_\mu\gamma_\nu \otimes \sigma^*_\mu\sigma^*_\nu$
scalar	$\mathbf{1} \otimes \mathbf{1}$	1	$\tilde{\gamma}_4\gamma_\mu\gamma_\nu \otimes \sigma^*_\mu\sigma^*_\nu$
local vector	$\gamma_\mu\gamma_0 \otimes \sigma^*_3\sigma^*_\mu$	$(-)^{x_0+x_1} + (-)^{x_0+x_2}$	$\tilde{\gamma}_4\gamma_\mu\gamma_0 \otimes \sigma^*_3\sigma^*_\nu$
conserved vector	$\gamma_\mu \otimes \mathbf{1}$		$\tilde{\gamma}_4\gamma_\mu \otimes \sigma^*_3$

staggered fermions. In $(3+1)$ dimensions, the additional, alternating state is the parity partner of the original operator defined on the entire hypercube. An analogous procedure can be followed for other channels, with the results displayed in Table 6.1. Constructing basic interpolating operators for lattice fermions that keep the Dirac spinor structure intact, such as Wilson fermions, is straightforward and closely resembles the procedure that one would perform in the continuum.

As in the case of the Dirac quasiparticle, one must perform a fit of the correlator to a functional form in order to obtain energies for the pseudoscalar particle in both the temporal and spatial directions. For this thesis, one is interested in zero-momentum correlators, which for the temporal direction are fit to the following form

$$\begin{aligned} C^{(t)}_{PS}(\vec{p}=0,\tau) &= \sum_{\vec{x}} C^{(t)}_{PS}(\vec{x},\tau), \\ &= A\left(e^{-m_\pi\tau} + e^{-m_\pi(N_\tau-\tau)}\right) \\ &+ (-)^\tau \tilde{A}\left(e^{-m'_\pi\tau} + e^{-m'_\pi(N_\tau-\tau)}\right), \end{aligned} \tag{6.54}$$

where m_π and m'_π refer to the masses of the pseudoscalar state and its partner, respectively. An example of a pseudoscalar correlator is shown in Fig. 6.6. An analogous expression exists for the correlator in the spatial direction

$$\begin{aligned} C^{(x)}_{PS}(x,p_y=0,\omega_0=0) &= \sum_{y,\tau} C^{(t)}_{PS}(x,y,\tau), \\ &= A\left(e^{-m^{(s)}_\pi\tau} + e^{-m^{s}_\pi(N_\tau-\tau)}\right) \\ &+ (-)^\tau \tilde{A}\left(e^{-m^{(s)\prime}_\pi\tau} + e^{-m^{(s)\prime}_\pi(N_\tau-\tau)}\right), \end{aligned} \tag{6.55}$$

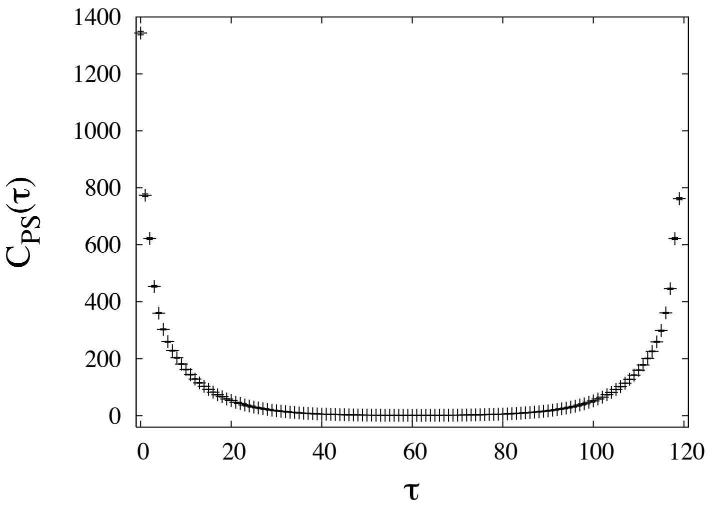

Figure 6.6. Zero-momentum pseudoscalar correlator in the temporal direction for lattice ensemble $8^2 \times 10 \times 120, \beta = 0.80, m = 0.05, \Phi_B = 0.125$ with 800 gauge configurations.

with the caveat that due to the fact that $\mathcal{O}_{PS}$ is a bosonic operator, one can project to zero Matusbara frequency, $\omega_0 = 0$ and m_π^s, $m_\pi^{s'}$ are the pseudoscalar screening masses. In the expression (6.54), one can include additional sets of terms representing excited states. Excited states are notoriously difficult to obtain and require methods that are beyond the scope of this thesis [83].

6.4 Analysis of Correlators

After obtaining the correlator by performing the appropriate inversions and momentum projections, one then must extract an energy from its behavior as a function of time (space) separation. In the previous section, the appropriate fit forms were discussed for the Dirac quasiparticles as well as the NG mode. Before performing a fit, one must find an appropriate fit range which is determined by the demands of the problem. For this thesis, one is only interested in the ground state in a given channel, and thus one needs to determine the range where this term dominates and all excited states are strongly suppressed. A good indicator for identifying this region is the effective mass

$$m_{eff}(\tau) = \frac{1}{4}\left[\log\left(\frac{C(\tau)}{C(\tau+1)}\right) + \log\left(\frac{C(\tau-1)}{C(\tau)}\right) + \log\left(\frac{C(\tau-2)}{C(\tau-1)}\right)\right], \tag{6.56}$$

where $C(\tau)$ is a two-point correlator in the temporal direction and the three terms are included due to the oscillations in (6.51). When the excited states have effectively died out, the effective mass plateaus, and is a guide to choosing the fit range for the Monte Carlo data. An example for the pseudoscalar is shown in Fig. 6.7. To determine the ground state mass and its associated uncertainty from correlator data, one needs to perform a nonlinear least-squares analysis that takes into account correlations between points at different time separations. This is done by introducing the correlation matrix, which is defined by

$$\mathcal{C}_{i,j} = \frac{1}{N(N-1)} \sum_{k=1}^{N} \left[C^{(k)}(\tau_i) - \bar{C}(\tau_i) \right] \left[C^{(k)}(\tau_j) - \bar{C}(\tau_j) \right], \tag{6.57}$$

$$\bar{C}(\tau_i) \equiv \frac{1}{N} \sum_{k=1}^{N} C^{(k)}(\tau_i), \tag{6.58}$$

where N is the number of configurations and $\tau_i = ia_t,\ i = 0, 1, \ldots, N_\tau - 1$. The diagonal elements of the correlation matrix give the variance of the correlator values, while the off-diagonal elements give information regarding correlations between measurements at different time separation. One can employ the correlation matrix in constructing a modified chi-squared functional that is to be minimized in order to obtain the desired fit parameters

$$\chi^2 \equiv \sum_{i,j} \left[\bar{C}(\tau_i) - f(i, \{m\}) \right] \left[\mathcal{C}^{-1} \right]_{i,j} \left[\bar{C}(\tau_j) - f(j, \{m\}) \right], \tag{6.59}$$

where $f(i, \{m\})$ is the fit function evaluated at time τ_i, with $\{m\}$ representing the fit parameters. The error on the mass can be determined in the same way as for uncorrelated nonlinear least-squares fits. For a large number of degrees of freedom d, one expects a good fit to yield $\chi^2 = d \pm \sqrt{2d}$. There still arises the question of how one chooses the fit range $[\tau_{min}, \tau_{mas}]$. In practice, one can examine the effective mass to get an initial estimate of the fit range and then refine the fit window until one obtains the best chi-squared value.

6.5 Estimation of Errors

In a Monte Carlo calculation, one has to be aware of autocorrelations in order to accurately estimate the statistical uncertainties associated with the observables that are computed. In the course of performing a Monte Carlo calculation, there exist correlations between neighboring configurations in the Markov chain, or more specifically, between neighboring MD trajectories. What one hopes to estimate, for any observable computed using MC methods, is the variance in the mean. However, the aforementioned correlations between configurations in simulation time make this process much more subtle. The naive variance of the mean for an observable $\mathcal{O}$ is given by

$$\sigma^{(0)2}_{mean} = \frac{1}{N} \left(\langle \mathcal{O}^2 \rangle - \langle \mathcal{O} \rangle^2 \right). \tag{6.60}$$

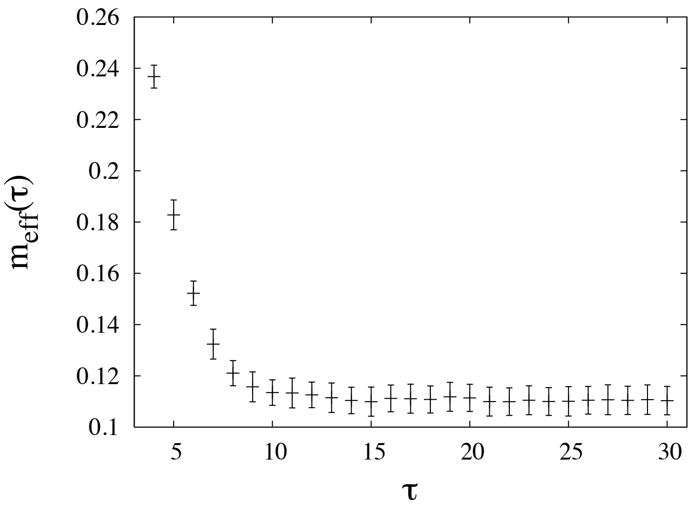

Figure 6.7. Effective mass of the pseudoscalar correlator in the temporal direction for lattice ensemble $8^2 \times 10 \times 120, \beta = 0.80, m = 0.05, \Phi_B = 0.125$ with 800 gauge configurations. At several time slices away from the source, one can notice the formation of a plateau indicating the dominance of the ground state.

This estimate, often biased by autocorrelations, can be corrected. One first introduces the autocorrelation function

$$C(\tau) = \langle \tilde{\mathcal{O}}^{(i)} \tilde{\mathcal{O}}^{(j)} \rangle, \tag{6.61}$$

$$\tilde{\mathcal{O}}^{(i)} \equiv \left(\mathcal{O}^{(i)} - \langle \mathcal{O} \rangle \right) / \sigma^{(0)}, \tag{6.62}$$

where $\tau \equiv (i-j)\delta t$ is the separation of the two measurements in MC time which is typically given in units of MD trajectories and the average is performed over the the entire ensemble. Imagine, now, that one knew the value of the slowest decay mode of (6.61), which one refers to as the autocorrelation time, τ_{AC}. Now, if one constructed well-separated blocks of M measurements, such that $M > \tau_{AC}$, one could compute the true variance using these blocked values. Namely, one could use the following expression to determine the true variance

$$\sigma^2_{mean} = \langle \left(\frac{1}{M} \sum_i \tilde{\mathcal{O}}^{(i)} \right)^2 \rangle = \sigma^{(0)2}_{mean} \left[1 + 2 \sum_{i>0} C(i\delta t) \right]. \tag{6.63}$$

The correction factor in (6.63) accounts for the autocorrelations and can be estimated directly. An alternative method involves constructing blocks of successive measurements and obtaining the variance as a function of block size n_b

$$\sigma^2_{mean}(n_b) = \frac{n_b^2}{N^2} \sum_i \left(\langle \mathcal{O} \rangle_i - \langle \mathcal{O} \rangle \right)^2 , \tag{6.64}$$

where $\langle \mathcal{O} \rangle_i$ is the average in the ith block. One finally attemps to extrapolate to infinite block size using a linear form for $\sigma(n_b)$ as a function of $1/n_b$. Other, more sophisticated methods are available which attempt to obtain accurate estimates of the correction factor on the right hand side of (6.63). These methods have found success in LQCD simulations where slow modes appear due to the autocorrelation of the topological charge [84, 85].

CHAPTER 7

RESULTS

In this chapter, the results of the lattice simulation of the graphene EFT in the presence of an external magnetic field will be discussed. First, the semimetal phase, characterized by a vanishing of the chiral condensate in the limit $m \to 0$, will be identified in the absence of the magnetic field. Then, introducing a magnetic field, the phenonemon of magnetic catalysis will be studied. As shown in previous studies [21, 22], magnetic catalysis is a property of the ground state of the field theory and thus should be present at $T = 0$. Taking the zero-temperature limit, which on the lattice consists of taking $N_\tau \to \infty$, one is able to isolate the ground state and then investigate the spontaneous symmetry breaking as the explicit symmetry breaking parameter, m, is removed.

7.1 Chiral Condensate

In this section, the calculation of the chiral condensate will be discussed. This quantity signals the spontaneous breaking of the remnant $U(1)_\epsilon$ symmetry which characterizes the phenomenon of magnetic catalysis in the lattice version of the graphene EFT.

7.1.1 Identifying the Semimetal Phase

At large values of the inverse coupling β, the graphene EFT describes a semimetal with gapless fermionic excitations and a vanishing value of the condensate, $\langle \bar{\psi}\psi \rangle$, in the chiral limit, $m \to 0$. As one increases the coupling, the theory has been shown to undergo a phase-transition to an insulating phase characterized by gapped fermionic excitations and a nonvanishing value of the chiral condensate, $\langle \bar{\psi}\psi \rangle \neq 0$. Various aspects of the transition have been studied using lattice methods [19, 86, 87, 88]. The transition is believed to be second-order according to the results of [19].

To identify the semimetal phase, one needs to look at the behavior of $\sigma \equiv \langle \bar{\psi}\psi \rangle$ as a function of the bare fermion mass m, at fixed coupling. The fermion mass, introduced as an infrared regulator needed in order to perform inversions to compute the fermon propagator, explicitly breaks the $U(1)_\epsilon$ symmetry present in the massless staggered fermion action. In the symmetric (semimetal) phase, one expects that for sufficiently small values of the fermion mass, σ will vanish linearly in m. This can be seen in Fig. 7.1, where σ is plotted as a function of m in the semimetal region at zero magnetic field (black points). As the inverse coupling decreases, one eventually encounters the critical coupling β_{cr}, which separates the semimetal from the insulating phase.

The situation changes significanly after an external magnetic field is introduced. Namely, the critical coupling β_{cr}, which determines the boundary between the two phases, shifts to larger values. This was shown in the lattice study performed in [89]. In this study, the authors, using unimproved staggered fermions, obtained a phase diagram in the (B, β)-plane. One expects that this phase boundary has a temperature dependence. In the limit $T \to 0$, the authors of [21, 22, 23] predict that an infinitesimal interaction between fermions and antifermions will lead to pairing, and thus magnetic catalysis. Another early analysis of a graphene-like theory showed that at extremely weak coupling, a nonzero condensate was obtained in the chiral limit [90].

After identifying the semimetal region, one can then introduce the external magnetic field and perform a similar calculation at fixed β. In Fig. 7.1 one can see that after the external magnetic field is introduced, σ increases and exhibits a nonlinear behavior as a function of m (blue points). However, just as is the case at zero magnetic field, σ vanishes as the explicit symmetry breaking parameter m is removed. One must, therefore, reconcile these results with the predictions from the infinite-volume continuum EFT.

7.1.2 Finite-Volume Effects

Typically, behavior of the type exhibited in Fig. 7.1 is associated with the restoration of symmetry due to the finite spatial extent of the box. One recalls that spontaneous symmetry breaking only exists in the infinite volume limit and thus one is obligated to perform an infinite-volume extrapolation in order to obtain information on the catalysis. In Fig. 7.2, one can see the behavior of σ versus m for a number of spatial extents, N_s, at magnetic flux $\Phi_B = 0.125$. For a large range of spatial extents N_s, the condensate shows little variation. This can be explained by noting that the magnetic length, $l_B \equiv \sqrt{\hbar c/eB}$, which characterizes the quasiparticle's cyclotron orbit, satisfies $1 < l_B < L_s$, in units of a_s.

An independent check for finite volume effects can be performed by calculating the screening masses of the fermion quasiparticle and the pseudoscalar. Expected to be the lightest excitations of the theory, the Compton wavelengths associated with their screening masses could be compared to N_s in order to characterize the effect of a finite spatial volume.

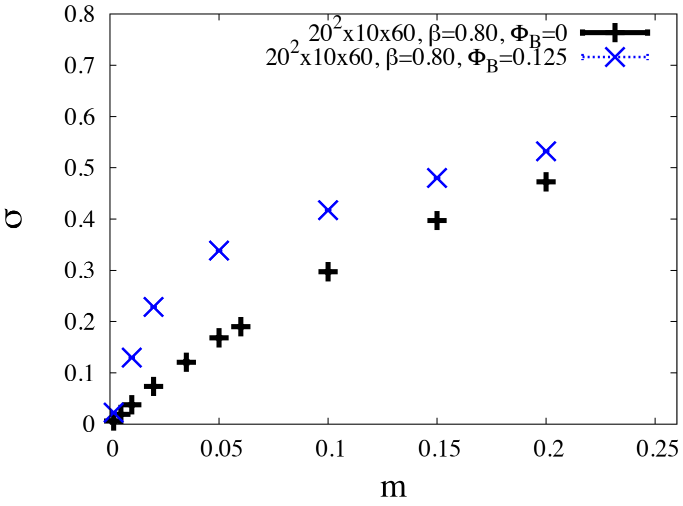

Figure 7.1. The chiral condensate $\sigma \equiv \langle\bar{\psi}\psi\rangle$ as a function of the bare fermion mass at zero field (black points) and at magnetic flux $\Phi_B = 0.125$ (blue points), where flux is measured in units of a_s^2. We report the volumes in the form $N_s^2 \times N_z \times N_\tau$. One can note that σ vanishes with m at zero field as well as at nonzero external field. The vanishing of the condensate in the presence of the magnetic field is argued to be a thermal effect. The error bars on each point are not visible on this scale.

The screening masses are obtained by computing the spatial correlators defined in (6.46) and (6.55). The result of this calculation is that the screening masses satisfy $M^{(s)}L_s > 1$ where $L_s = N_s a_s$ and $M^{(s)}$ represents a screening mass. In particular, for the pseudoscalar, $m_\pi^{(s)}L_s \approx 18 - 20$, for the ensembles with volume $20^2 \times 10 \times 60$ and flux $\Phi_B = 0.125$ while for the fermion propagator, $m_F^{(s)}L_s \approx 11 - 14$, for the same ensembles. Typically, in LQCD, leading finite-volume corrections are of the form $e^{-M_s L_s}$. Thus, these results give further confirmation that finite-volume corrections are under control.

7.1.3 Finite-Temperature Effects

Thermal effects are also known to affect lattice simulations due to the finite extent of the box. The temperature of the system is inversely proportional to the extent of the box in Euclidean time, $T = 1/N_\tau a_t$. In order to isolate the ground state of the system, one must make sure that N_τ is sufficiently large. The effects of temperature on the chiral condensiate σ are exhibited in Fig. 7.3. One can see that at large values of the ratio T/m, the chiral symmetry is restored. As T/M approaches small values, the condensate obtains a finite value in the zero-temperature limit.

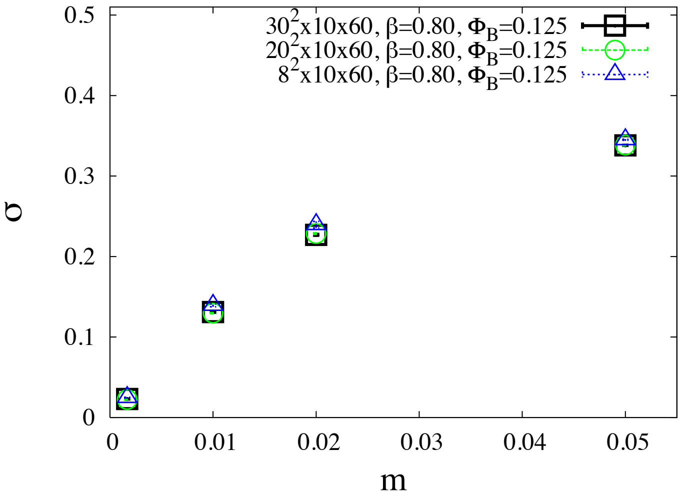

Figure 7.2. The chiral condensate σ as a function of fermion mass with varying spatial volume N_s^2 for magnetic flux $\Phi_B = 0.125$. The lattice volumes are listed in the form $N_s^2 \times N_z \times N_\tau$ where the fermions live in the xy-plane and the gauge field is present throughout the entire volume.

The predictions of magnetic catalysis in the continuum, for example in [21], are statements about the ground state of the theory. One has seen that in $(2+1)$ dimensions, even in the free theory, a finite value for the condensate is obtained. This derivation, in fact, already assumes that one has isolated the ground state of the theory, or equivalently, one has already performed the zero-temperature limit before taking the bare fermion mass to zero. This fact suggests that in order to obtain information on magnetic catalysis for the data reported above, one must first perform the $T \to 0$ limit before taking the chiral limit, $m \to 0$.

For a given bare mass, one can see from the data pictured in Fig. 7.3 that as small temperatures are approached, the value of σ reaches a plateau. Due to the fact that one does not have an analytic formula to guide the zero-temperature extrapolation, a polynomial extrapolation was used. For the points residing on the plateau, for example the first two points at bare mass $m = 0.05$, a fit to a constant was used. Adding a third point at higher T, a fit to a polynomial, $\sigma(T) = c_0 + c_1 T + c_2 T^2$ was performed. These two approaches were used in order to estimate a systematic error associated with this extrapolation due to the lack of an analytic formula for a guide. The systematic error is taken to be the difference in the central values obtained for the two extrapolations described above. One assumes that

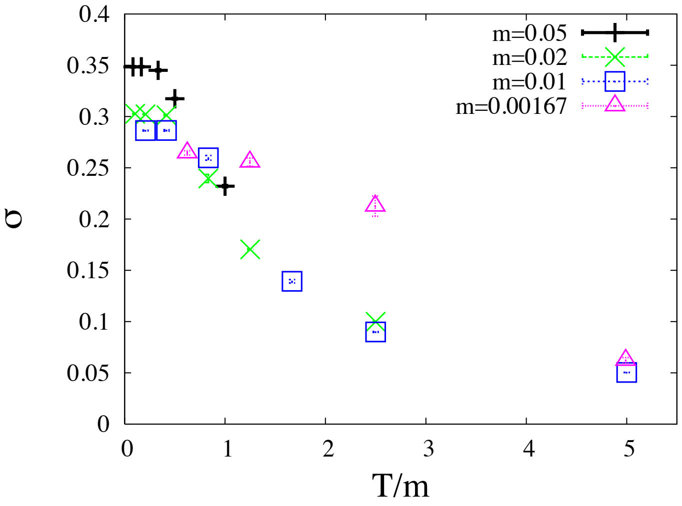

Figure 7.3. The chiral condensate σ plotted as a function of the ratio T/m for the ensembles with $\Phi_B = 0.125$ and $N_s = 8, N_z = 10$. One can see that at small values of T/m, the condensate increases and tends towards a nonzero value.

this error adds in quadrature with the statistical error, thus giving a total error which is used in later results. The results for the extrapolations performed at magnetic flux $\Phi_B = 0.125$ for bare mass $m = 0.05$ are shown in Fig. 7.4

Once the zero-temperature extrapolations have been performed, one can then take the chiral limit. In Fig. 7.5, the chiral condensate at $T = 0$ is plotted as a function of the bare mass at $\Phi_B = 0.125$. One can see that a linear extrapolation in the mass gives a nonzero value for the condensate. After performing the same extrapolations for three fluxes, one is able to obtain the behavior of the zero-temperature, chirally extrapolated condensate as a function of the magnetic flux, Φ_B. The results are shown in Fig. 7.6. The relationship between the condensate and Φ_B is fit to the form $\sigma_{T=m=0} = c_1\Phi_B + c_2\left(\Phi_B\right)^2$. This is motivated by the fact that at zero magnetic flux, the condensate should vanish in the chiral limit. The errors on the points in the plot are those calculated in the chiral extrapolation.

7.2 Haldane Condensate

The situation for the time-reversal-odd Haldane condensate is less clear than that of the chiral condensate. This has much to do with staggered fermions and the issue of the taste degree of freedom. In the simulations with staggered fermoins, only taste-singlet operators have been used. This has consequences for the original hexagonal lattice degrees

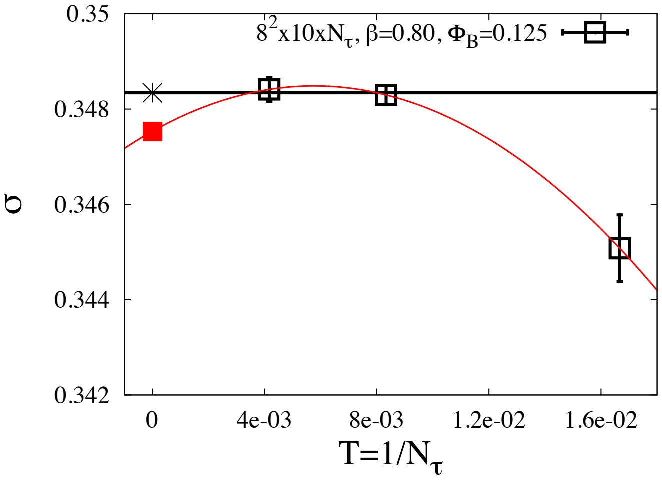

Figure 7.4. The chiral condensate σ plotted as a function of the temperature T for the ensemble with $\Phi_B = 0.125$, $N_s = 8, N_z = 10$, $m = 0.05$. The constant function (black curve) gives an intercept of 0.3483(2) with $\chi^2 \approx 0.13$. The quadratic (red curve) gives an intercept of 0.3475(8). The difference between these values gives an estimate of the systematic error associated with the extrapolation.

of freedom, as these simulations cannot distinguish spin components. Furthermore, taste-nonsinglet operators have zero expectation value as the vacuum has zero taste quantum numbers. This situation is unfortunate, and makes a comparison with the continuum results difficult. In the continuum, the Zeeman term in (3.30) explicitly breaks the $U(4)$ symmetry to $U(2)_\uparrow \times U(2)_\downarrow$. Noting that in the ground state solution described by (3.34), the Haldane masses for the two spin projections are opposite in sign, one can see that the Zeeman spin splitting is enhanced. In the absence of the Zeeman term, the solution described by (3.34) signals the spontaneous breaking of the $U(4)$ symmetry and implies a nonzero value for the condensate $\langle \bar{\psi} \, (\tilde{\gamma}_{4,5} \otimes \sigma_3) \, \psi \rangle$. However, the staggered lattice action only contains a remnant $U(1) \times U(1)_\epsilon$ symmetry and does not distinguish spin projection. Thus, unlike the case of the chiral condensate, the appearance of a nonzero value for the time-reversal-odd condensate, $\langle \bar{\psi} \, (\tilde{\gamma}_{4,5} \otimes \mathbf{1}) \, \psi \rangle$, does not lead to spontaneous symmetry breaking.

The time-reversal-odd condensate was measured on the lattice ensembles with the largest magnetic flux, $\Phi_B = 0.125$ for $a_\tau T = [0.002, 0.016]$. These temperatures are sufficiently small that if the ground state did support a Haldane condensate, these temperatures would be sufficiently small and the magnetic flux sufficiently large to observe this. The results,

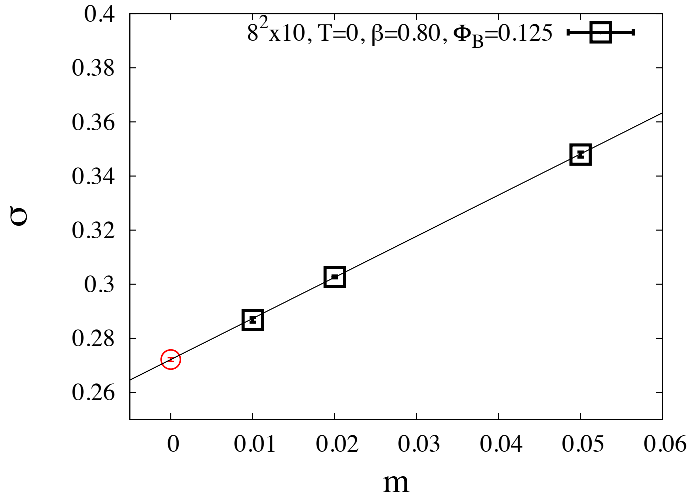

Figure 7.5. The zero-temperature extrapolated chiral condensate σ plotted as a function of the bare mass m for magnetic flux $\Phi_B = 0.125$ and lattice size $N_s = 8, N_z = 10$. The linear chiral extrapolation gives an intercept of 0.2721(7) with $\chi^2/d \approx 0.6$.

however, do no support a nonzero Haldane condensate. In Fig. 7.7, the real part of the Haldane mass is plotted versus the temperature for $N_\tau = 480$, $\Phi_B = 0.125$. In this calculation, each point was computed with 1000 stochastic sources on 100 gauge configurations. The results seem to be consistent with zero. The results for larger temperature at the same value of the flux also are consistent with zero as one would expect.

When interpreting these relations for the Haldane condensate, one must keep in mind that taste-nonsinglet operators have zero expectation values. In particular, this means that $\langle\bar{\psi}\,(\tilde{\gamma}_{4,5}\otimes\sigma_3)\,\psi\rangle$ is exactly zero due to taste symmetry. To address spontaneous symmetry breaking due to the appearance of a nonzero value for $\langle\bar{\psi}\,(\tilde{\gamma}_{4,5}\otimes\sigma_3)\,\psi\rangle$, one would need to include a term in the action that breaks this symmetry explicitly and in the usual way, take in the infinite volume and zero-temperature limits followed by removing the symmetry breaking term. This is what was done for the Dirac mass.

7.3 Spectrum

In this section, the spectrum of the graphene EFT will be discussed. In the absence of an external magnetic field, one expects to be firmly in the semimetal phase at the fixed coupling, $\beta = 0.80$. This should be reflected in the dynamical mass of the Dirac quasiparticle. Namely, one expects a nonperturbative calculation of the temporal fermion propagator, represented

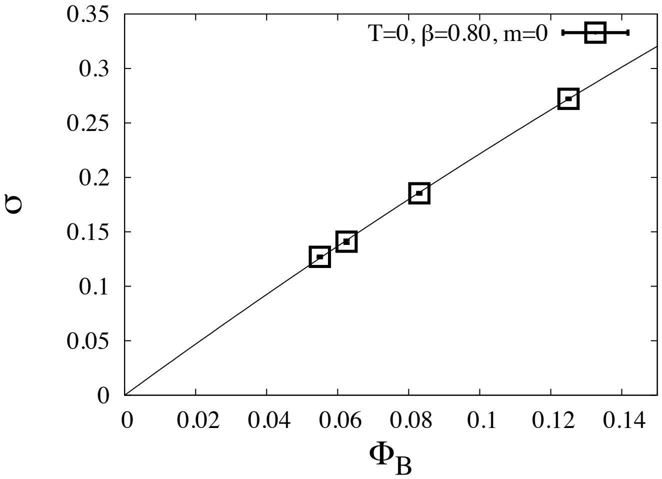

Figure 7.6. The zero-temperature, chirally extrapolated chiral condensate σ, plotted as a function of the magnetic flux $\Phi_B = eB/2\pi$. The points at $\Phi_B = 0.0625$ and $\Phi_B = 0.125$ have a spatial size of $N_s = 8$, while those at $\Phi_B = 0.056$ and $\Phi_B = 0.083$ have a spatial size of $N_s = 12$. The errors on the points were obtained from the chiral extrapolations at $T = 0$. The data have been fit to a quadratic which passes through the origin. The fit has parameters $c_1 = 2.38(2)$ and $c_2 = -1.6(2)$ with a $\chi^2/d \approx 3.6/2$.

in (6.39), to yield a mass, m_F, that vanishes in the chiral limit. The situation is expected to change drastically in the presence of an external magnetic field. Namely, one expects a nonzero value for the dynamical mass in the chiral limit. Furthermore, the pseudoscalar mode, studied via the correlator in (6.51), is predicted to be a Goldstone mode due to the spontaneous symmetry breaking that occurs.

7.3.1 Dirac Quasiparticle

As discussed in the previous chapter, the spectrum can give additional information characterizing the spontaneous breaking of the $U(1)_\epsilon$ chiral symmetry. As a consequence of the acquisition of a nonzero value for the chiral condensate, one expects the fermions to acquire a dynamical mass which is nonzero as the bare mass vanishes. Obtaining an accurate extrapolation in the bare mass can be difficult, as illustrated in Fig. 7.8. One can see that a simple linear extrapolation in the bare mass for the nonperturbative points seems to suggest a nonzero value for the dynamical mass in the chiral limit. In order to further investigate this, a calculation of the fermion pole at $O(e^2)$ in lattice perturbation theory was performed. This calculation used a one-link unimproved staggered action which included a

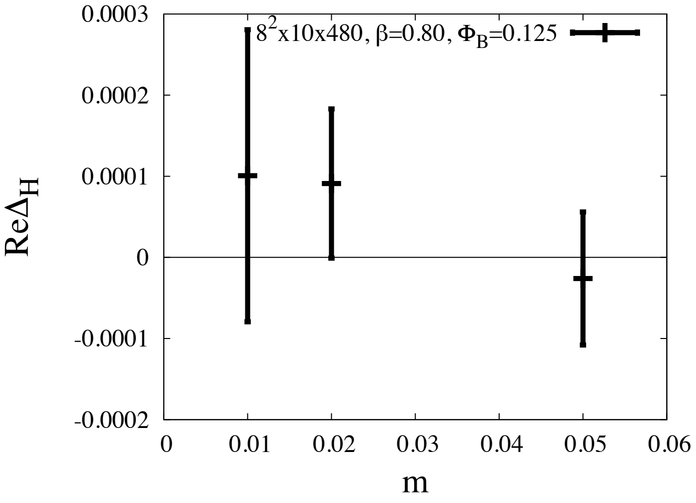

Figure 7.7. The real part of the Haldane condensate as a function of the fermion bare mass m for $8^2 \times 10 \times 480, \beta = 0.80, \Phi_B = 0.125$.

perturbative value of the tadpole factor to the same order in the coupling. Further details of this calculation can be found in Appendix A. The perturbative result for the pole of the fermion propagator shows that as one reaches very small bare masses, the curve develops large curvature and eventually vanishes at the origin. This can be better seen in Fig. 7.9, where the perturbative result is shown in a region near the origin. Using this result as a heuristic explanation of the results obtained at zero magnetic field, one might expect the same to happen in the chiral limit for a nonperturbative calculation.

For the case of nonzero magnetic field, the results for the dynamical fermion mass are encouraging, as seen in Fig. 7.10. One notices that at a given bare mass, the dynamical mass increases with the magnetic flux, which is also illustrated in Fig. 7.11 at a fixed bare mass. Furthermore, the plot suggests that all four ensembles extrapolate to nonzero values in the chiral limit. However, in light of the behavior observed in the zero-field case, one might want to be cautious in predicting the behavior at bare masses smaller than those plotted.

7.3.2 Pseudoscalar

The pseudoscalar mode in the graphene EFT is predicted to be the Goldstone mode resulting from the spontaneous chiral symmetry breaking. As discussed previously, this mode is analogous to the pion in QCD which is also a Goldstone boson in the limit of

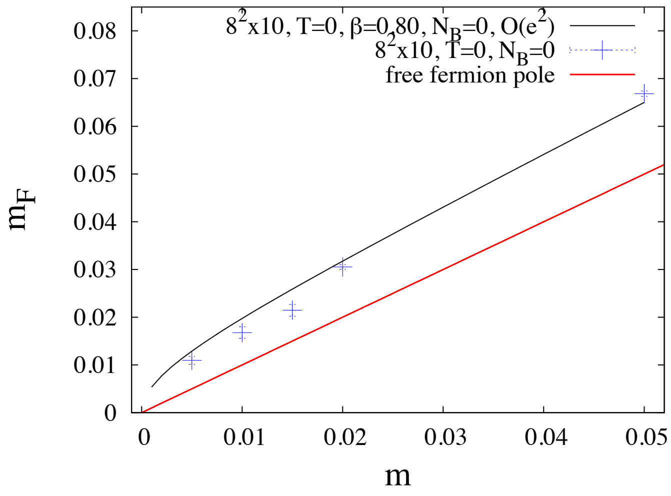

Figure 7.8. The dynamical fermion mass as a function of the bare fermion mass at zero magnetic flux. Both the nonperturbative determination and the $O(e^2)$ perturbative determination have been included. The solid line represents the location of the free fermion pole, $\log(m + \sqrt{m^2 + 1})$. One can see that perturbative result heuristically explains the nonperturbative result.

vanishing quark mass. To determine the pseudoscalar mass, a fit of the temporal two-point function was performed using the form listed in (6.54). The results are seen in Fig. 7.12, where the mass of the pseudoscalar is plotted as a function of the bare mass. One should first point out that these results, in conjunction with those in Fig. 7.10, determine that the pseudoscalar mode is indeed a bound state. The fermion-antifermion scattering state has energy $2m_F$ (at zero spatial momentum), which is higher than m_π for all simulated bare masses. One can also see from the results of Fig. 7.12 that the pseudoscalar mass shows little variation in flux. This in contrast with QCD, where electrically charged pions couple to the external magnetic field and their mass recieves a contribution due to this interaction [91].

One can see that the mass of the pseudoscalar seems to vanish linearly with the bare mass. However, in analogy with chiral symmetry breaking in QCD, one expects a Gell-Mann-Oakes-Renner relation between the pion mass and the fermion mass, $m_\pi^2 \sim m$ [92]. A possible reconciliation of these two comes from the fact that spatial box size is not large enough to properly characterize the relation between the pseudoscalar mass and the fermion mass. Namely, one typically wants the spatial box size to be larger than a certain

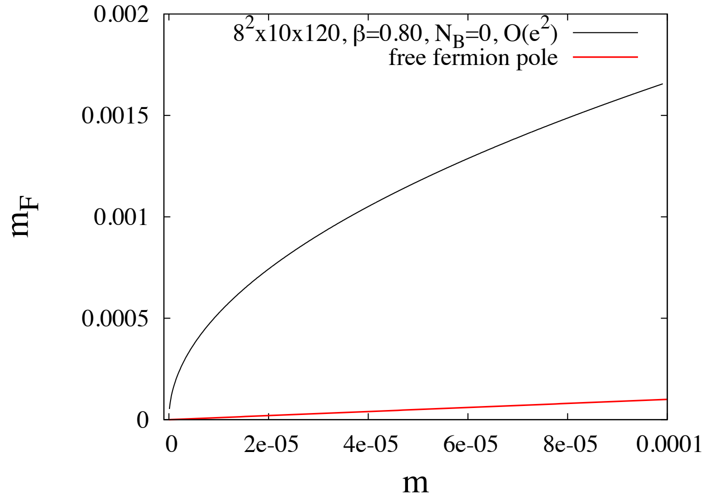

Figure 7.9. The pole of the fermion propagator at $O(e^2)$ along with the free fermion pole as one approaches the chiral limit, $m \to 0$. One can see that the pole at $O(e^2)$ vanishes in this limit, as expected. However, the curvature that causes this behavior can be observed only as one moves to extremely small fermion bare masses.

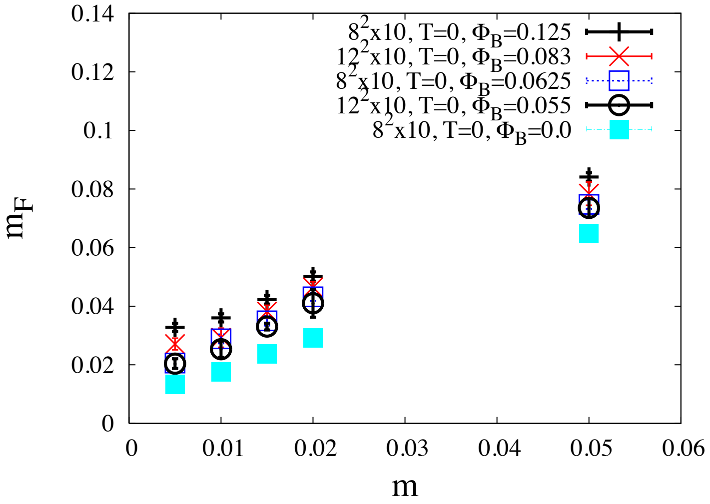

Figure 7.10. The dynamical fermion mass as a function of the bare mass for all four magnetic fluxes as well as at zero magnetic flux.

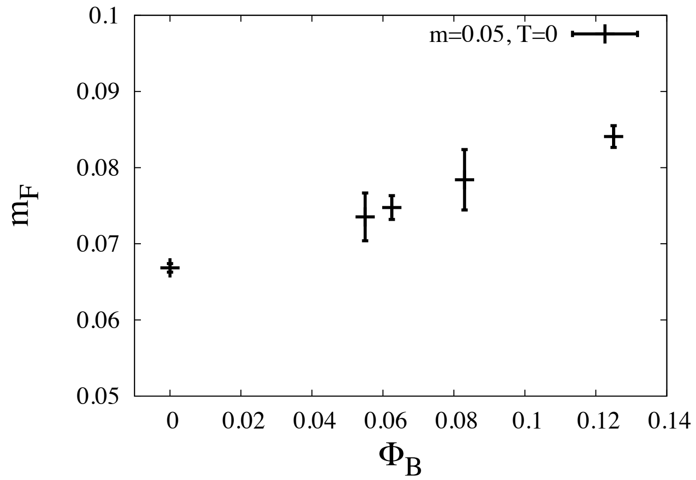

Figure 7.11. The dynamical fermion mass as a function of the magnetic flux at a fixed bare mass of $m = 0.005$. The data is taken from the Fig. 7.10.

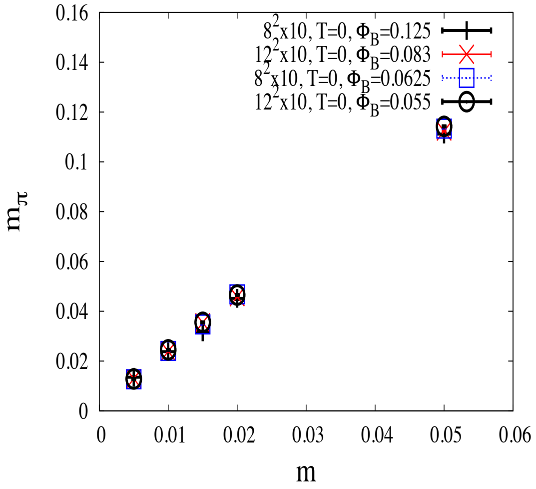

Figure 7.12. The mass of the pseudoscalar bound state as a function of the bare fermion mass for all four magnetic fluxes.

multiple of the pion's Compton wavelength measured in lattice units, which in this case is $\lambda_\pi \equiv 1/(m_\pi a_t) = [9, 74]$. Noting that the spatial box sizes used in this study are $N_s = 8, 12$, one can imagine that finite volume corrections are hampering the verification of the Gell-Mann-Oakes-Renner relation which is an infinite-volume result.

CHAPTER 8

CONCLUSION AND OUTLOOK

In this chapter, conclusions are drawn regarding the lattice study of the graphene EFT. Finally, future works are discussed as well as an outlook for the field in general.

8.1 Conclusion

Through a thorough, full nonperturbative study of the graphene EFT, the existence of spotaneous symmetry breaking due to an external magnetic field has been shown. This represents an important step in the study of magnetic catalysis in condensed matter systems. The ground state of the system has been characterized by performing a zero-temperature extrapolation of the observables, in particular the chiral condensate. Furthermore, the difficulties in studying the Haldane mass with staggered fermions has been commented on. This study has shown evidence for a dynamically generated Dirac mass for the quasiparticle as well as the nonzero value for the chirally extrapolated, $T = 0$ chiral condensate. As a result, one obtains strong evidence that indeed, magnetic catalysis is occuring in the graphene EFT. The study of the pseudoscalar mass was able to determine that it is indeed a fermion-antifermion bound state. Furthermore, the vanishing of its mass in the chiral limit showed that it is indeed the Goldstone boson that results from the spontaneous breaking of the lattice $U(1)_\epsilon$ symmetry.

8.2 Outlook

The use of lattice methods in studying the graphene EFT in the presence of a magnetic field has proven to be quite successful. For a fixed temperature, the authors of [89] have mapped out a phase diagram of the theory in the (β, B)-plane. The results showed that the magnetic field shifts the critical coupling, β_{cr}, to larger values. One possible extension of this work which could lend support to the results of this thesis would be to map out the temperature dependence of this phase line. One would expect that at as the temperature decreases, the line would move closer to the β-axis. Thus, for a given coupling, the external magnetic field needed to put the system into the insulating phase would decrease.

Another continuation of this work on the graphene EFT would be a more precise study of the order of the zero-field transition from a semimetal to an insulator. Although the zero magnetic field phase transition from a semimetal to an insulator has been previously studied [19], a more thorough analysis is needed to determine precise values of critical exponents as well as the critical dielectric constant, ϵ_{cr}. Previous studies found large finite volume effects in the insulator phase, which necessitates a careful scaling analysis in order to determine the parameters characterizing the phase transition.

Finally, a further direction to investigate would be the exploration of the effects of adding more species of Dirac fermions to the graphene-like theory studied in this thesis. One would like to see if there exists a critical number of fermion species above which the theory is always in the semimetal phase. Early work in this direction studied a model similar to the graphene EFT in the limit of strong coupling and large N_f [93]. In this limit, the theory is tractable and a renormalization group analysis was employed. Other studies have provided estimates for the critical number of flavors [94, 47]. These studies have used a Schwinger-Dyson approach in the instantaneous approximation and concluded that the critical number of species is $N_{cr} \approx 2.55$. Using staggered fermions in $(2+1)$ dimensions, one can easily simulate an even number of flavors. Odd integers can be simulated by employing rooted staggered fermions which although controversial in the context of LQCD, would be necessary here in order to determine the critical number of fermion species.

APPENDIX

PERTURBATIVE CALCULATION OF FERMION POLE

In this appendix, the calculation of the fermion pole in lattice perturbation theory will be discussed. First, a quick introduction to the conventions and Feynman rules for the graphene EFT on the lattice are given. This is followed by the calculation of the fermion self-energy to $O(e^2)$. Using this result, one can extract the pole of the fermion propagator to the same order in the coupling.

A.1 Conventions and Feynman Rules

To derive the Feynman rules, which are illustrated in Fig. A.1, one first starts with the lattice action for the graphene EFT

$$S = S_G^{(NC)} + S_F, \tag{A.1}$$

where $S_G^{(NC)}$ is the noncompact gauge action given by (4.60) and here S_F is taken to be the naive fermion action with tadpole improvement

$$\begin{aligned} S_F &= a_s^2 a_t \sum_n \Bigg[\bar{\psi}_n \gamma_0 \left(\frac{1}{2u_0 a_t}\right) \left(e^{iea_t A_0(n)} \psi_{n+\hat{0}} - e^{-iea_t A_0(n)} \psi_{n-\hat{0}}\right) \\ &+ v_F \sum_i \bar{\psi}(n) \gamma_i \left(\frac{1}{2a_s}\right) \left(\psi_{n+\hat{\imath}} - \psi_{n-\hat{\imath}}\right) + m \bar{\psi}_n \psi_n \Bigg], \end{aligned} \tag{A.2}$$

where $u_0 = \langle U_P \rangle^{1/2}$ is the tadpole factor calculated from the average of the space-time-oriented plaquette, U_P. Notice that in the above expression for the fermion action, the link variable has been expressed in terms of the continuum gauge potential, $A_0(n)$. Expanding the link variables up to terms quadtratic in the coupling, the fermion action becomes

$$S_F = S_F^{(0)} + S_F^{(1)} + S_F^{(2)} + O(a_t^2), \tag{A.3}$$

where

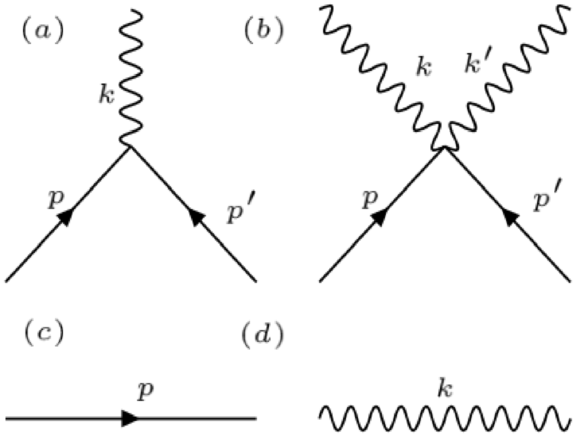

Figure A.1. In (a), the familiar photon-fermion vertex is depicted. In (b), the two-photon-fermion vertex is shown. This is a lattice artifact that vanishes in the naive continuum limit $a \to 0$. In (c) and (d), the fermion and photon lines are shown which are associated with the appropriate propagator.

$$\begin{aligned} S_F^{(0)} &= a_s^2 a_t \sum_n \left[\bar{\psi}_n \gamma_0 \left(\frac{1}{2u_0 a_t} \right) (\psi_{n+\hat{0}} - \psi_{n-\hat{0}}) \right. \\ &+ \left. v_F \sum_i \bar{\psi}(n) \gamma_i \left(\frac{1}{2a_s} \right) (\psi_{n+\hat{i}} - \psi_{n-\hat{i}}) + m\bar{\psi}_n \psi_n \right] \end{aligned} \tag{A.4}$$

is the free fermion action and

$$S_F^{(1)} = a_s^2 a_t \left(\frac{ie}{2u_0} \right) \sum_n \left[\bar{\psi}_n \gamma_0 A_0(n) \psi_{n+\hat{0}} + \bar{\psi}_{n+\hat{0}} \gamma_0 A_0(n) psi_n \right], \tag{A.5}$$

$$S_F^{(2)} = -a_s^2 a_t \left(\frac{a_t e^2}{4u_0} \right) \sum_n \left[\bar{\psi}_n \gamma_0 A_0^2(n) \psi_{n+\hat{0}} - \bar{\psi}_{n+\hat{0}} \gamma_0 A_0^2(n) \psi_n \right]. \tag{A.6}$$

The terms in (A.5) and (A.6) give rise to the fermion-gauge-field interactions. In the naive continuum limit, $a \to 0$, the former reduces to the continuum interaction term given by (2.10). The coupling of two photons to the fermions is described by (A.6) and has no continuum analog. This term is present as a result of the lattice regularization and vanishes as $a \to 0$ [95].

To derive the Feynman rules, one first goes to momentum space where the fields have the following Fourier decompositions

$$\begin{aligned} \hat{A}_0(n) &= \int_{BZ} \frac{d^4k}{(2\pi)^4} \hat{A}_0(k) e^{ik\cdot(n+\hat{0}/2)}, & \text{(A.7)} \\ \hat{\psi}_n &= \int_{BZ} \frac{d^3k}{(2\pi)^3} \hat{\psi}(k) e^{ik\cdot n}, & \text{(A.8)} \\ \hat{\bar{\psi}}_n &= \int_{BZ} \frac{d^3k}{(2\pi)^3} \hat{\bar{\psi}}(k) e^{-ik\cdot n}, & \text{(A.9)} \end{aligned}$$

where dimensionless lattice fields have been introduced and the integral is over the Brillouin zone in dimensionless lattice momenta. One also notices that in (A.7), the gauge potential has been defined at the midpoints of the links connecting neighboring sites. Fourier transforming the terms in (A.5) and (A.6), one obtains the following vertices

$$\Gamma_0^{(1)}(p',p,k) = -\frac{ie}{u_0}(2\pi)^3\delta(p-p'+k)\gamma_0\cos((p+p')/2), \tag{A.10}$$

$$\Gamma_0^{(2)}(p,p',k,k') = \frac{ia_t e^2}{u_0}(2\pi)^3\delta(p-p'+k+k')\gamma_0\sin((p+p')/2), \tag{A.11}$$

where $\delta(p)$ is the periodic delta-function, p and p' are the incoming and outgoing fermion momenta, respectively, and k and k' are the incoming photon momenta. For each fermion or photon line, one associates the corresponding propagator. The fermion and photon propagators can be obtained from (4.60) and (A.4). The fermion propagator is given by

$$G_0(p) = \frac{-i\gamma_0\tilde{p}_0 - iv_F s\sum_i \gamma_i\tilde{p}_i + m}{m^2 + \tilde{p}_0^2 + v_F\sum_i \tilde{p}_i^2}, \tag{A.12}$$

where $\tilde{p}_\mu \equiv \sin(p_\mu)$. At zero spatial momentum, the pole of the free fermion propagator is located at $\log(m+\sqrt{m^2+1})$. The photon propagator is given by

$$D(p) = \int_{-\pi}^{\pi}\frac{dp_z}{2\pi}\tilde{D}(p), \tag{A.13}$$

$$\tilde{D}(p) \equiv \frac{1}{\bar{p}_z^2 + \sum_i \bar{p}_i^2}, \tag{A.14}$$

where $\bar{p}_\mu \equiv \sin(p_\mu/2)$.

A.2 Fermion Self-Energy

As discussed earlier, the mass of the fermion is associated with the pole of its propagator. Using the Feynman rules discussed in the previous section, one would like to perturbatively determine the effects of interactions on the fermion mass. To begin, one first notes that the full fermion propagator can be written

$$G(p) = \frac{1}{i\gamma_0\tilde{p}_0 + iv_F\sum_i \gamma_i\tilde{p}_i + m_0 - \Sigma(p)}, \tag{A.15}$$

where $\Sigma(p)$ is the self-energy determined from the one-particle irreducible diagrams with two external fermion lines [8]. At $O(e^2)$, the self-energy is given by the graphs depicted in Fig. A.2. Using the Feynman rules, one writes

$$\Sigma^{(2)}(p) = \Sigma_a^{(2)}(p) + \Sigma_b^{(2)}(p), \tag{A.16}$$

where the contributions from the two graphs are given by

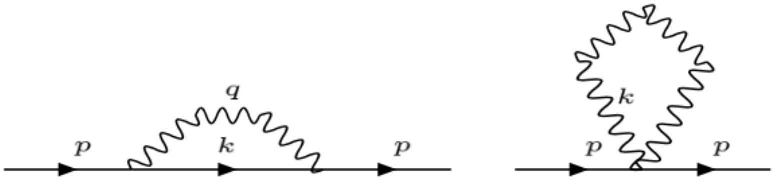

Figure A.2. The fermion self-energy at $O(e^2)$ in lattice perturbation theory. (left) The "sunset" graph familiar from continuum perturbation theory. (right) The "tadpole" graph that appears on the lattice due to the two-photon-fermion vertex.

$$\begin{aligned}\Sigma_a^{(2)}(p_0,\vec{p}) &= \frac{(ie)^2}{u_0 N_s^2}\sum_{q_i}\int\frac{dq_0}{2\pi}\gamma_0\frac{-i\sum_\mu\gamma_\mu\tilde{k}_\mu+m_0}{\sum_\mu\tilde{k}_\mu^2+m_0^2}\gamma_0\cos^2(p_0+q_0/2)D(q), &\text{(A.17)}\\ \Sigma_b^{(2)}(p_0,\vec{p}) &= i\gamma_0\sin(p_0)\frac{e^2}{u_0N_s^2}\sum_{q_i'}D(q'), &\text{(A.18)}\end{aligned}$$

where $\tilde{k}_\mu \equiv \sin(p_\mu+q_\mu)$. In the expressions (A.17) and (A.18), the integrals over the spatial lattice momenta have been replaced by sums. This is due to the fact that the lattice calculations of Chapter 7 are done at finite volume, which restricts the momenta to discrete values. For the sum in (A.17), this restricts the momentum to be

$$q_i = \frac{2\pi n_i}{N_s},\; n_\mu = -N_s/4, -N_s/4+1,\ldots,-1,0,1,\ldots,N_s/4-1. \tag{A.19}$$

This particular set of values for the momentum reflects the fact that in order to include the effect of staggered fermions, one shrinks the size of the Brillouin zone by a factor of two. This is due to the fact that the spin-taste basis for staggered fermions is defined on a lattice of spacing $2a$. The sum in (A.18) involves a photon loop and thus

$$q_\mu' = \frac{2\pi n_\mu'}{N_\mu},\; n_\mu' = -N_\mu/2, -N_\mu/2+1,\ldots,-1,0,1,\ldots,N_\mu/2-1, \tag{A.20}$$

where the zero-momentum mode, $q_\mu = 0, \forall\mu$, is excluded in the sum due to the gauge-fixing condition (4.102). The integral over the zeroth component of the loop momentum has been kept as one assumes a zero-temperature formalism.

To determine the shift in the mass due to interactions, one sets $\vec{p}=0$ and looks for the pole of the propagator. The most general form for the self-energy based on lattice symmetries takes the form

$$\Sigma(p_0,\vec{p}) = i\sum_\mu\gamma_\mu\sin(p_\mu)F_\mu(p_0,\vec{p}) + m_oH(p_0,\vec{p}), \tag{A.21}$$

where F_μ and H are functions determined perturbatively in the coupling. In this thesis, one is interested in the dynamical mass of the fermion. The dynamical mass is the pole of the zero-momentum propagator, which at $O(e^2)$ is determined by

$$\begin{aligned}\left(1 - e^2 F_0^{(2)}(p_0,\vec{0})\right)^2 \sin^2(p_0) + m_0^2\left(1 - e^2 H^{(2)}(p_0,\vec{0})\right)^2 &= 0, \qquad \text{(A.22)}\\ \left(1 - 2e^2 F_0^{(2)}(p_0,\vec{0})\right)\sin^2(p_0) + m_0^2\left(1 - 2e^2 H^{(2)}(p_0,\vec{0})\right) + O(e^4) &= 0, \qquad \text{(A.23)}\end{aligned}$$

where $F_\mu^{(2)}$ and $H^{(2)}$ are the self-energy terms at $O(e^2)$. The above condition was determined after rationalizing the fermion propagator in (A.15). To find the pole in the interacting theory, one writes $p_0 \to i\tilde{\omega}$, and (A.23) becomes

$$\sinh^2(\tilde{\omega}) = m_0^2\left(1 - 2e^2 H^{(2)}(i\omega_0,\vec{0}) + 2e^2 F_0^{(2)}(i\omega_0,\vec{0})\right) \qquad \text{(A.24)}$$

where the replacement $p_0 \to i\omega_0$ has been made in the functions $F_0^{(2)}$ and $H^{(2)}$ as one is only working at $O(e^2)$. The pole, $\tilde{\omega}$, can thus be written as

$$\begin{aligned}\tilde{\omega} &= \log\left(\tilde{\Omega} + \sqrt{\tilde{\Omega}^2+1}\right), \qquad \text{(A.25)}\\ \tilde{\Omega} &= m_0\sqrt{1 - 2e^2 H^{(2)}(i\omega_0,\vec{0}) + 2e^2 F_0^{(2)}(i\omega_0,\vec{0})}. \qquad \text{(A.26)}\end{aligned}$$

To determine these functions, one considers (A.17) and (A.18) at zero spatial momentum. One finds that

$$\begin{aligned}F_0^{(2)}(p_0,\vec{0}) &= \frac{1}{u_0 N_s^2}\sum_{\vec{q}}\int \frac{dq_0}{2\pi}\frac{\cos(q_0)+\sin(q_0)\cot(p_0)}{\sin^2(p_0+q_0)+\sum_i \sin^2(q_i)+m_0^2}\cos^2(p_0+q_0/2)D(q)\\ &+ \frac{1}{u_0 N_s^2}\sum_{q_i'} D(q'), \qquad \text{(A.27)}\end{aligned}$$

$$\begin{aligned}H^{(2)}(p_0,\vec{0}) &= -\frac{1}{u_0 N_s^2}\sum_{\vec{q}}\int \frac{dq_0}{2\pi}\frac{1}{\sin^2(p_0+q_0)+\sum_i \sin^2(q_i)+m_0^2}\\ &\times \cos^2(p_0+q_0/2)D(q). \qquad \text{(A.28)}\end{aligned}$$

To proceed, one makes the substitution $p_0 \to i\omega_0$ in the functions $F_0^{(2)}$ and $H^{(2)}$ and evaluates the integration over q_0 in the above expressions using the method of residues. One first considers the general expression

$$I = \int \frac{dq_0}{2\pi}\frac{f(q_0,i\omega_0)}{\sin^2(q_0+i\omega_0)+\sum_i \sin^2(q_i)+m_0^2}, \qquad \text{(A.29)}$$

where $f(q_0, i\omega_0)$ is a regular function of q_0. One can employ the mapping $z = e^{iq_0 - \omega_0}$ which maps the integral over q_0 into a closed contour in the complex z plane. This contour is a circle of radius $e^{-\omega_0}$. The expression in (A.29) thus becomes

$$I = -4 \oint \frac{dz}{2\pi i} \frac{z f(z)}{z^4 - 2bz^2 + 1}, \tag{A.30}$$

$$b \equiv 1 + 2 \left(\sum_i \sin^2(q_i) + m_0^2 \right). \tag{A.31}$$

The integrand has poles at $\pm z_+$ and $\pm z_-$ where

$$(z_\pm)^2 = b \pm \sqrt{b^2 - 1}, \;\; z_\pm = e^{\pm\omega}, \tag{A.32}$$

$$\cosh(2\omega) = b, \;\; \sinh(\omega) = \sqrt{\sum_i \sin^2(q_i) + m_0^2}. \tag{A.33}$$

The roots $\pm z_-$ lie within the contour, thus one can evaluate I via residues, obtaining

$$\begin{aligned} I &= -4 \oint \frac{dz}{2\pi i} \frac{z f(z)}{(z - z_+)(z - z_-)(z + z_+)(z + z_-)}, \\ &= \frac{f(z_-) + f(-z_-)}{\sinh(2\omega)}. \end{aligned} \tag{A.34}$$

From the expression for $H^{(2)}(i\omega_0, 0)$, one makes the identification $f(q_0) = \cos^2(i\omega_0 + q_0/2)$. Changing variables to z results in

$$f(z) = \frac{1}{4} \left(z^{1/2} e^{-\omega_0/2} + \frac{1}{z^{1/2}} e^{\omega_0/2} \right)^2. \tag{A.35}$$

One can use the result in (A.34) to obtain

$$H^{(2)}(i\omega_0, 0) = -\frac{1}{u_0 N_s^2} \sum_{\vec{q}} \frac{D(q)}{\sinh(2\omega)}. \tag{A.36}$$

From the expression for $F_0^{(2)}(i\omega_0, 0)$, one makes the identification $f(q_0) = [\cos(q_0) - i \sin(q_0) \coth(\omega_0)] \cos^2(i\omega_0 + q_0/2)$. Changing variables to z results in

$$\begin{aligned} f(z) &= \frac{1}{8} \left[\left(z e^{\omega_0} + \frac{1}{z} e^{-\omega_0} \right) - \left(z e^{\omega_0} - \frac{1}{z} e^{-\omega_0} \right) \coth(\omega_0) \right] \\ &\times \left(z^{1/2} e^{-\omega_0/2} + \frac{1}{z^{1/2}} e^{\omega_0/2} \right)^2. \end{aligned} \tag{A.37}$$

One can use the result in (A.34) to obtain

$$\begin{aligned} F_0^{(2)}(i\omega_0, 0) &= \frac{1}{u_0 N_s^2} \sum_{\vec{q}} D(q) \frac{\cosh(\omega + \omega_0)}{\sinh(2\omega)} \left(\cosh(\omega - \omega_0) + \sinh(\omega - \omega_0) \coth(\omega_0) \right) \\ &+ \frac{1}{u_0 N_s^2} \sum_{q_i'} D(q'). \end{aligned} \tag{A.38}$$

Finally, the expressions in (A.36) and (A.38) have been used to numerically evaluate the mass shift depicted in Fig. 7.8 and Fig. 7.9.

The tadpole factor used in this calculation was also calculated perturbatively. From its definition one can write

$$\begin{aligned} u_0 &\equiv \mathbb{R}\mathrm{e}\langle U_P\rangle^{1/2} \approx 1 - \frac{1}{2V}e^2a^2\sum_n \langle A_0(n)A_0(n)\rangle \\ &+ \frac{1}{6V}e^2a^2\sum_i\sum_n \mathbb{R}\mathrm{e}\langle A_0(n)A_0(n+\hat{i})\rangle, \qquad (A.39) \\ U_P(n) &\equiv \frac{1}{3}\sum_i U_0(n)U_0^\dagger(n+\hat{i}) = \frac{1}{3}\sum_j e^{ie(A_0(n)-A_0(n+\hat{i}))} \qquad (A.40) \end{aligned}$$

where V is the volume and the space-time plaquette has been expanded in terms of the gauge potential. The second and third terms on the right-hand side of (A.39) can be represented at lowest order by the following expression

$$\frac{1}{V}\sum_n \langle A_0(n)A_0(n)\rangle = \frac{1}{N_s^2}\sum_{q'} D(q') + O(e^2), \qquad (A.41)$$

$$\frac{1}{3V}\sum_i\sum_n \mathbb{R}\mathrm{e}\langle A_0(n)A_0(n+\hat{i})\rangle = \frac{1}{3N_s^2}\sum_i\sum_{q'} D(q')\cos(q'_i) + O(e^2) \qquad (A.42)$$

One finds that the value of tadpole factor calculated in lattice perturbation theory is close to the nonperturbative value used in obtaining the results of Fig. 7.10. This reflects the fact that the tadpole factor has a weak dependence on the bare fermion mass.

REFERENCES

[1] L. Hands, S. J. Del Debbio and J. C. Mehegan, Nucl. Phys. B **502**, 269 (1997).

[2] P. R. Wallace, Phys. Rev. **71**, 622 (1947).

[3] J. W. McClure, Phys. Rev. **108**, 612 (1957).

[4] J. W. Slonczewski and P. R. Weiss, Phys. Rev. **109**, 272 (1958).

[5] K. S. Novoselov et al., Science **306**, 666 (2004).

[6] N. W. Ashcroft and N. D. Mermin, *Solid State Physics* (Saunders College, New York, N.Y., 1976).

[7] E. McCann and V. I. Fal'ko, Phys. Rev. Lett. **96**, 086805 (2006).

[8] M. Peskin and D. Schroeder, *Introduction to Quantum Field Theory* (Addison-Wesley, 1995).

[9] J. L. Manes, Phys. Rev. B **75**, 155424 (2007).

[10] F. D. M. Haldane, Phys. Rev. Lett. **61**, 2015 (1988).

[11] V. P. Gusynin, S. G. Sharapov, and J. P. Carbotte, Int. J. Mod. Phys. B **21**, 4611 (2008).

[12] E. Fermi, Il Nuovo Cimento **11**, 1 (1934).

[13] S. Weinberg, Physica A **96**, 327 (1979).

[14] J. Gasser and H. Leutwyler, Annals Phys. **158**, 142 (1984).

[15] J. Bardeen, L. N. Cooper, and J. R. Schrieffer, Phys. Rev. **106**, 162 (1957).

[16] K. G. Wilson, Phys. Rev. B **4**, 3174 (1971).

[17] T. Ortín, *Gravity and Strings* (Cambridge, New York, N.Y., 2004).

[18] S. Weinberg, *The Quantum Theory of Fields, Vol. 1* (Cambridge, New York, N.Y., 1995).

[19] J. E. Drut and T. A. Lähde, Phys. Rev. B **79**, 165425 (2009).

[20] J. Giedt, A. Skinner, and S. Nayak, Phys. Rev. B **83**, 045420 (2011).

[21] V. Gusynin, V. Miransky, and I. Shovkovy, Phys. Rev. Lett. **73**, 3499 (1994).

[22] V. Gusynin, V. Miransky, and I. Shovkovy, Phys. Lett. B **349**, 477 (1995).

[23] V. Gusynin, V. Miransky, and I. Shovkovy, Phys. Rev. D **52**, 4718 (1995).

[24] V. Gusynin, V. Miransky, and I. Shovkovy, Nucl. Phys. B **462**, 249 (1996).

[25] Y. Nambu and G. Jona-Lasinio, Phys. Rev. **122**, 345 (1961).

[26] Y. Nambu and G. Jona-Lasinio, Phys. Rev. **124**, 246 (1961).

[27] I. A. Shovkovy, Lect. Notes Phys. **871**, 13 (2013).

[28] A. Akhiezer and V. Berestetsky, *Quantum Electrodynamics* (Interscience, New York, 1965).

[29] J. S. Schwinger, Phys. Rev. **82**, 664 (1951).

[30] W. Dittrich and H. Gies, Phys. Lett. B **392**, 182 (1997).

[31] W. Dittrich and M. Reuter, *Effective Lagrangians in Quantum Electrodynamics* (Springer, Berlin, 1985).

[32] N. D. Mermin and H. Wagner, Phys. Rev. Lett. **17**, 1133 (1966).

[33] S. Coleman, Nucl. Phys. B **145**, 110 (1978).

[34] Y. Nambu, Phys. Rev. **117**, 648 (1960).

[35] J. Goldstone, Nuovo Cimento **19**, 154 (1961).

[36] J. Goldstone, A. Salam, and S. Weinberg, Phys. Rev. **127**, 965 (1962).

[37] S. P. Klevansky, Rev. Mod. Phys. **64**, 649 (1992).

[38] J. Hubbard, Phys. Rev. Lett. **3**, 77 (1959).

[39] R. L. Stratonovich, Soviet Physics Doklady **2**, 416 (1957).

[40] D. Gross and A. Neveu, Phys. Rev. D **10**, 3235 (1974).

[41] E. Witten, Nucl. Phys. B **145**, 110 (1978).

[42] B. Simon, Annals Phys. **97**, 279 (1976).

[43] H. L. Stormer, P. Kim, Y. Zhang, and Y. W. Tan, Nature **438**, 201 (2005).

[44] D. Jiang, M. Katsnelson, K. Novoselov, and A. Geim, Nature **438**, 197 (2005).

[45] V. P. Gusynin and S. Sharapov, Phys. Rev. Lett. **95**, 146801 (2005).

[46] J. P. Small et al., Phys. Rev. Lett. **96**, 136806 (2006).

[47] E. Gorbar, V. Gusynin, V. Miransky, and I. Shovkovy, Phys. Rev. B **66**, 045108 (2002).

[48] E. Gorbar, V. Gusynin, V. Miransky, and I. Shovkovy, Phys. Rev. B **78**, 085437 (2008).

[49] E. Gorbar, V. Gusynin, V. Miransky, and I. Shovkovy, Phys. Scripta T **146**, 014018 (2012).

[50] V. A. Miransky and I. A. Shovkovy, Phys. Rep. **576**, 1 (2015).

[51] I. L. Aleiner, D. E. Kharzeev, and A. M. Tsvelik, Phys. Rev. B **76**, 195415 (2007).

[52] M. Kharitonov, Phys. Rev. B **85**, 155439 (2012).

[53] D. V. Khveshchenko, Phys. Rev. Lett. **87**, 206401 (2001).

[54] R. P. Feynman, Rev. Mod. Phys. **20**, 367 (1948).

[55] F. A. Berezin, *The Method of Second Quantization* (Academic Press, 1966).

[56] K. G. Wilson, *New Phenomena in Subnuclear Physics (Erice, 1975)* (Plenum, 1975).

[57] H. B. Nielsen and M. Ninomiya, Nucl. Phys. **185**, 20 (1981).

[58] P. H. Ginsparg and K. G. Wilson, Phys. Rev. D **25**, 2649 (1982).

[59] M. Atiyah and I. M. Singer, Ann. Math. **93**, 139 (1971).

[60] P. Hasenfratz, V. Laliena, and F. Niedermayer, Phys. Lett. B **427**, 125 (1998).

[61] J. B. Kogut and L. Susskind, Phys. Rev. D **9**, 3501 (1974).

[62] J. B. Kogut and C. G. Strouthos, Phys. Rev. D **71**, 094012 (2005).

[63] T. DeGrand and C. DeTar, *Lattice Methods for Quantum Chromodynamics* (World Scientific, 2006).

[64] C. Burden and A. N. Burkitt, Eur. Phys. Lett. **3**, 545 (1987).

[65] H. Kluberg-Stern, A. Morel, O. Napoly, and B. Peterson, Nucl. Phys. B **220**, 447 (1983).

[66] R. Jackiw and S. Templeton, Phys. Rev. D **23**, 2291 (1981).

[67] A. Bazavov et al., Rev. Mod. Phys. **82**, 1349 (2010).

[68] J.-F. Lagaë and D. K. Sinclair, Nucl. Phys. Proc. Suppl. **63**, 892 (1998).

[69] K. Orginos, R. Sugar, and D. Toussaint, Phys. Rev. D **60**, 054503 (1999).

[70] P. Lepage, Nucl. Phys. B **60**, 12 (1998).

[71] S. Naik, Nucl. Phys. B **316**, 238 (1989).

[72] G. P. Lepage and P. B. Mackenzie, Phys. Rev. D **48**, 2250 (1993).

[73] M. N. Rosenbluth, A. H. Teller, N. Metropolis, A. W. Rosenbluth, and E. Teller, J. Chem. Phys. **21**, 1087 (1953).

[74] D. J. E. Callaway and A. Rahman, Phys. Rev. Lett. **49**, 613 (1982).

[75] D. J. E. Callaway and A. Rahman, Phys. Rev. D **28**, 1503 (1983).

[76] D. Toussaint, R. L. Renken, S. A. Gottlieb, W. Liu, and R. L. Sugar, Phys. Rev. D **35**, 2531 (1987).

[77] S. Duane and J. B. Kogut, Phys. Rev. Lett. **55**, 2774 (1985).

[78] S. Duane and J. B. Kogut, Nucl. Phys. B **275**, 398 (1986).

[79] J. Zak, Phys. Rev. **134**, 1603 (1964).

[80] M. H. Al-Hashimi and U. J. Wiese, Annals Phys. **324**, 343 (2009).

[81] G. S. Bali et al., JHEP **2**, 44 (2012).

[82] G. H. Golub and C. F. Van Loan, *Matrix Computations* (Johns Hopkins University Press, 1996).

[83] C. Gattringer and C. B. Lang, *Quantum Chromodynamics on the Lattice* (Springer, 2010).

[84] U. Wolff, Comput. Phys. Commun. **156**, 143 (2004).

[85] R. Sommer, S. Schaefer, and F. Virotta, Nucl. Phys. B **845**, 93 (2011).

[86] J. E. Drut and T. A. Lähde, Phys. Rev. Lett. **102**, 026802 (2009).

[87] W. Armour, S. Hands, and C. Strouthos, Phys. Rev. B **81**, 125105 (2010).

[88] W. Armour, S. Hands, and C. Strouthos, Phys. Rev. B **84**, 075123 (2011).

[89] D. L. Boyda, V. V. Braguta, S. N. Valgushev, M. I. Polikarpov, and M. V. Ulybyshev, Phys. Rev. B **89**, 245404 (2014).

[90] P. Cea, L. Cosmai, P. Guidice, and A. Papa, Phys. Rev. D **85**, 094505 (2012).

[91] I. A. Shushpanov and A. V. Smilga, Phys. Lett. B **402**, 351 (1997).

[92] M. Gell-Mann, R. J. Oakes, and B. Renner, Phys. Rev. **175**, 2195 (1968).

[93] D. T. Son, Phys. Rev. B **75**, 235423 (2007).

[94] H. Leal and D. V. Khveshchenko, Nucl. Phys. B **687**, 323 (2004).

[95] H. J. Rothe, *Lattice Gauge Theories: An Introduction* (World Scientific, 2005).